

INFORMATION TO USERS

This manuscript has been reproduced from the microfilm master. UMI films the text directly from the original or copy submitted. Thus, some thesis and dissertation copies are in typewriter face, while others may be from any type of computer printer.

The quality of this reproduction is dependent upon the quality of the copy submitted. Broken or indistinct print, colored or poor quality illustrations and photographs, print bleedthrough, substandard margins, and improper alignment can adversely affect reproduction.

In the unlikely event that the author did not send UMI a complete manuscript and there are missing pages, these will be noted. Also, if unauthorized copyright material had to be removed, a note will indicate the deletion.

Oversize materials (e.g., maps, drawings, charts) are reproduced by sectioning the original, beginning at the upper left-hand corner and continuing from left to right in equal sections with small overlaps.

Photographs included in the original manuscript have been reproduced xerographically in this copy. Higher quality 6" x 9" black and white photographic prints are available for any photographs or illustrations appearing in this copy for an additional charge. Contact UMI directly to order.

ProQuest Information and Learning
300 North Zeeb Road, Ann Arbor, MI 48106-1346 USA
800-521-0600

UMI[®]

**Manifold based voltage stability boundary tracing, margin control optimization
and time domain simulation**

by

Yuan Zhou

**A dissertation submitted to the graduate faculty
in partial fulfillment of the requirements for the degree of
DOCTOR OF PHILOSOPHY**

Major: Electrical Engineering (Electric Power)

Program of Study Committee:

Venkataramana Ajarapu, Major Professor

Vijay Vittal

James D. McCalley

Degang J. Chen

Scott Hansen

Iowa State University

Ames, Iowa

2001

Copyright © Yuan Zhou, 2001. All rights reserved.

UMI Number: 3034242

Copyright 2001 by
Zhou, Yuan

All rights reserved.

UMI[®]

UMI Microform 3034242

Copyright 2002 by ProQuest Information and Learning Company.
All rights reserved. This microform edition is protected against
unauthorized copying under Title 17, United States Code.

ProQuest Information and Learning Company
300 North Zeeb Road
P.O. Box 1346
Ann Arbor, MI 48106-1346

**Graduate College
Iowa State University**

**This is to certify that the doctoral dissertation of
Yuan Zhou
has met the dissertation requirements of Iowa State University**

Signature was redacted for privacy.

Major Professor

Signature was redacted for privacy.

For the Major Program

TABLE OF CONTENTS

LIST OF FIGURES	ix
CHAPTER 1. INTRODUCTION	1
1.1 Industry Concerns about Voltage Stability	1
1.1.1 Load Margin	1
1.1.2 Optimal Margin Control	2
1.1.3 Timing of Corrective Control	2
1.2 Power System Voltage Stability	2
1.2.1 Load Dynamics	2
1.2.2 Major Issues in Voltage Stability Study	3
1.3 Modeling for Voltage Stability Study	4
1.4 Voltage Stability Analysis	5
1.4.1 Power Flow Based Analysis	5
1.4.2 Small-Disturbance Analysis	6
1.4.3 Quasi-Steady-State Analysis (QSS)	7
1.4.4 Large Disturbance Analysis	8
1.5 Control Strategy	9
1.5.1 Sensitivity Based Margin Control Optimization	9
1.5.2 Nonlinear optimization of Margin Control	10
CHAPTER 2. LITERATURE REVIEW AND SCOPE OF THE WORK	11
2.1 Literature Review	11
2.1.1 Bifurcation Viewpoint	11

2.1.2	Optimization Viewpoint	14
2.1.3	Time Domain Viewpoint	15
2.2	Scope of Work	17
2.3	Organization of This Dissertation	20
CHAPTER 3. POWER SYSTEM MODELING		21
3.1	Formulation of Power System DAE model	21
3.1.1	Synchronous Generator	21
3.1.2	Excitation Control System	22
3.1.3	Prime Mover and Speed Governor	23
3.1.4	Nonlinear Load Model	24
3.1.5	LTC Model	25
3.1.6	HVDC Model	25
3.1.7	Network Power Equations	29
3.1.8	Modeling of Limit Constraints	30
3.1.9	Power System DAE model	34
3.2	Bifurcation Modeling of Power System Dynamics	35
3.2.1	Saddle Node Bifurcation	36
3.2.2	Hopf Bifurcation	36
3.2.3	Comparison with Time Domain Simulation	38
3.3	Manifold Models in Power Systems	38
3.3.1	Manifold	38
3.3.2	Natural Parameterization	39
3.3.3	Local Parameterization	39

3.3.4	Manifold Model in Power Systems	41
CHAPTER 4. POWER SYSTEM EQUILIBRIUM TRACING WITH DETECTION OF BOTH SADDLE NODE AND HOPF BIFURCATIONS		42
4.1	Natural Parameterization of Load Parameter Space for Power System Equilibrium Tracing	42
4.2	Equilibrium Manifold of Power System and Transverse Difficulty	43
4.3	Initialization of Power System Equilibrium Tracing	44
4.4	Continuation Method with Local Parameterization	45
4.5	Linearization of Power System DAE	46
4.6	Detection of Saddle Node and Hopf Bifurcation with System Total Jacobian Matrix	48
4.6.1	Detection of Saddle Node Bifurcation	50
4.6.2	Detection of Hopf Bifurcation without Eigenvalue Calculation	51
4.7	Numerical Example	56
4.7.1	Equilibrium Tracing with Detection of SNB and Hopf	56
4.7.2	Computational Requirements Compared with Eigenvalue Calculation	57
4.8	Summary	57
CHAPTER 5. UNIFIED MARGIN BOUNDARY TRACING		59
5.1	Introduction	59
5.2	Natural Parameterization for Margin Boundary Tracing	59
5.3	Formulation of Unified Margin Boundary Tracing	61
5.3.1	Margin Boundary Manifold of Power System	61

5.3.2	Bifurcation Characterization	61
5.3.3	Augmentation for Local Parameterization	64
5.3.4	Differentiation of Cut Functions	65
5.3.5	Unified Margin Boundary Tracing	67
5.4	Saddle Node Bifurcation Related Margin Boundary Tracing	70
5.4.1	Emergency Load Shedding	70
5.4.2	Reactive Power Support	71
5.4.3	Secondary Voltage Control	72
5.4.4	Control Combination	72
5.4.5	Multiple Contingencies	73
5.5	Saddle Node and Hopf bifurcation Related Stability Boundary Tracing	74
5.5.1	Boundary Tracing with Respect to Generation Control Parameters	74
5.5.2	Boundary Tracing with Respect to Network Parameter Change	76
5.6	Advantages of Unified Margin Boundary Tracing	78
5.7	Summary	78
CHAPTER 6. OPTIMAL MARGIN BOUNDARY TRACING WITH CONTINUATION		
	OPTIMAL POWER FLOW	79
6.1	Introduction	79
6.2	Problem Formulation	80

6.3	Formulation of Optimal Margin Boundary Tracing	83
6.3.1	Optimal Margin Boundary Manifold of Power System	83
6.3.2	Characterization of Optimal Margin Boundary	83
6.3.3	Optimal Margin Boundary Tracing with Continuation Optimal Power Flow	84
6.4	Optimal Margin Boundary Tracing Procedure	86
6.5	Numerical Results	87
6.5.1	Case 1: Load Shedding	88
6.5.2	Case 2: Control of Shunt Capacitance	89
6.6	Summary	90
CHAPTER 7. LOCAL PARAMETERIZATION BASED UNIFIED TIME DOMAIN		
	SIMULATION	91
7.1	Introduction	91
7.2	DAE Modeling for Time Domain Simulations	92
7.2.1	Multi-time-scale DAE Modeling	92
7.2.2	Quasi-Steady State DAE Modeling	93
7.2.3	Unified DAE Modeling of Power System Dynamics	94
7.3	Formulation of Conventional Time Domain Simulation of Unified DAE	94
7.3.1	Conventional Time Domain Simulation of Unified DAE	94
7.3.2	Conventional Time Domain Simulation of Multi-Time-Scale DAE	95
7.3.3	Conventional Time Domain Simulation of QSS DAE	96
7.4	Local Parameterization Based Time Domain Simulation of Unified DAE	97

7.4.1	Initial Point of Piecewise Manifold	97
7.4.2	Trajectory Predictor	97
7.4.3	Trajectory Corrector	98
7.4.4	Continuation Parameter Selection	99
7.5	Local Parameterization Based Time Domain Simulation for Special Cases	99
7.5.1	Multi-Time-Scale DAE	99
7.5.2	QSS DAE	101
7.6	Manifold Based Time Domain Simulation Procedure	103
7.7	Numerical Simulation Results	105
7.7.1	Results for Multi-Time Scale Time Domain Simulation	105
7.7.2	Results for QSS Simulation	110
7.7.3	Comparison with Margin Boundary Tracing	111
7.8	Summary	111
CHAPTER 8. CONCLUSIONS AND SUGGESTIONS FOR FUTURE WORK		113
8.1	Conclusions	113
8.2	Suggestions for Future Work	114
REFERENCES		115
APPENDIX		122
ACKNOWLEDGEMENTS		127

LIST OF FIGURES

Figure 2-1: Illustration of margin boundary tracing framework	13
Figure 2-2: Optimal margin boundary tracing	15
Figure 3-1: The IEEE type DC-1 excitation system	24
Figure 3-2: The simplified speed governor and prime mover	24
Figure 3-3: Capability curves (saliency and saturation neglected)	32
Figure 4-1: Flowchart for detection of Saddle node and Hopf bifurcations	55
Figure 4-2: Hopf detection in PV curve tracing under base control	57
Figure 5-1: Flowchart of margin boundary tracing	69
Figure 5-2: System load margin vs load shedding at bus 39	71
Figure 5-3: System load margin vs shunt capacitance at bus 8	71
Figure 5-4: System load margin vs Vref adjustment at all generator	72
Figure 5-5: System load margin vs control combination steps: <div style="margin-left: 40px; padding-left: 20px;">Vref39(0.001pu),C8(0.1pu),Q6(0.1pu)</div>	73
Figure 5-6: System load margin vs multiple contingencies: line 8-9 and line 7-8 outage	74
Figure 5-7: Unified margin boundary tracing versus Ka adjustment	75
Figure 5-8: Unified margin boundary tracing versus Vref adjustment	76
Figure 5-9: Unified margin boundary tracing versus load shedding	77
Figure 5-10: Unified margin boundary tracing versus line outage	78
Figure 6-1: Flowchart of optimal margin boundary tracing	87
Figure 6-2: Marge boundary optimization comparison between OMBT and Linear <div style="margin-left: 40px; padding-left: 20px;">Programming</div>	89

Figure 6-3: Margin boundary optimization comparison among OMBT, Linear Programming and, randomly chosen strategy (adding capacitance only at bus 20)	90
Figure 7-1: Locally parameterized time trajectory tracing	97
Figure 7-2: Flowchart of manifold based time domain simulation	104
Figure 7-3: Small disturbance time domain simulation	106
Figure 7-4: Hopf bifurcation caused oscillation observed	106
Figure 7-5: Line 8-9 is off at 80 sec	107
Figure 7-6: Load shedding at 20 seconds after contingency	108
Figure 7-7: Capacitance is on 20 seconds after contingency	109
Figure 7-8: Line 8-9 is off at base condition with no load variation	110
Figure 7-9: Quasi-Steady State simulation	111
Figure A-1: New England 39 bus system diagram	122

CHAPTER 1 INTRODUCTION

1.1 Industry Concerns about Voltage Stability

1.1.1 Load Margin

In an open access environment, less regulated power flow patterns and increased utilization of transmission facilities could more frequently violate system security conditions. Deterioration in system operating conditions makes the power system more vulnerable to disturbances.

Deregulation brings new challenges for operating the power system. Independent System Operator (ISO) needs to monitor the system load margin in real time and close the power transaction deals based on the available system stability margin as well as other considerations in order to meet the quickly varying energy demand. How to efficiently extend the system margin by readjusting the system control configuration becomes an important part of the overall economic operation of the power system.

In many cases, power is transferred via a highly stressed network. Voltage collapse and system oscillations, such as the Tokyo voltage collapse and Union Electric system oscillations [18] under heavy loading conditions, appeared in many reports.

Meanwhile a stressed system is vulnerable to be overloaded by a contingency, which causes the system voltage stability margin to shrink and could endanger a system even if it has survived the transient dynamics. Therefore, the voltage stability margin needs to be monitored.

1.1.2 Optimal Margin Control

How to efficiently extend the system margin by readjusting the system control configuration is also the major aspect of power system operational security. With FACTS devices widely applied in modern power systems, the capability and range of control are increased. Selection of cost efficient control then becomes an important part for economic operation of power systems.

Voltage stability constrained margin monitoring and optimization will provide indispensable control information for a modern power system Energy Management System (EMS).

1.1.3 Timing of Corrective Control

Load dynamics plays an important role for corrective control against voltage collapse. References [17,18] brought the timing issue into the concern of corrective control against voltage collapse. The amount of corrective control needed to save the system from voltage collapse depends on the timing of the control. The amount of required control increases dramatically if the time of the control is beyond the critical time [18,20].

1.2 Power System Voltage Stability

1.2.1 Load Dynamics

Generator angle stability was proposed and studied earlier than voltage stability. In general, rotor angle stability centers on the dynamics of generators and their regulators, whereas voltage stability centers on load dynamics. However in transient time scale, sometimes it is difficult to separate these two instabilities.

Due to the complexity of load characteristics, load dynamics may involve quite different time scales. For daily load variance, load dynamics is relatively slow compared to

rotor angle dynamics so that it could be modeled as a steady state variable. In this case, bifurcation theory could be applied with a steady state load variable as bifurcation parameter. Note that bifurcation theory could only be introduced with steady state variable as bifurcation parameter to characterize the dynamics of other dynamic variables. That is, the prerequisite of the bifurcation model is that the derivative of the bifurcation parameter equals zero.

For some of the loads, load restoration dynamics tend to restore their consumed power in the time frame of a second [5]. The load dynamics may relate to induction motors, HVDC. Since the time scale of this kind of load dynamics is close to rotor angle dynamics, load could no longer be taken as a steady state variable. Therefore bifurcation theory based voltage stability analysis may fail in this case. Multiple time scale based time domain simulation then becomes the basic tool to study transient load induced voltage stability. Since the critical corrective control time depends on load restoration dynamics, multiple time scale time domain simulation is also indispensable to design corrective control.

1.2.2 Major Issues in Voltage Stability Study

Considerable research has been devoted to many aspects of the voltage stability problem. The study can be classified as off-line or on-line according to the time scale of interest. Off-line voltage stability studies serve for operation planning. A longer time interval is required so that the computationally intensive analysis can be obtained. On the other hand, on-line voltage stability studies are needed for operation monitoring, alert, and instant decision support. On-line studies need to be computationally efficient to satisfy the demanding time requirement. Both of on-line and off-line studies share the following common key issues.

- **Analysis tools** are used to understand the mechanisms of the voltage instability and make planning or operation decisions based on reliable simulations. Power flow based analysis, small-disturbance analysis, quasi-steady-state analysis, and time domain simulation are the major tools that can be selected to perform voltage stability analysis of the system.
- **Indices** could be used on-line or off-line to help operators determine to what extent the system state is secure or dangerous. The criteria of those indices could be specified for the system security assessment. Linear indices, such as load margin, are more preferable than nonlinear ones.
- **Control strategy** is needed to mitigate voltage collapse, extend the stability margin, and economically dispatch while maintaining the margin requirement for security. In case the system is experiencing voltage instability, remedial control actions should be taken to effectively bring the system to a stable post-disturbance operation point.

The following sections briefly present the background of the thesis work regarding to the key issues mentioned above.

1.3 Modeling for Voltage Stability Study

Nonlinear load characteristics may drive the system to voltage collapse. Voltage regulating mechanisms on the generator side may lead the system to oscillatory instability. The interaction between rotor dynamics and induction motor dynamics may lead to oscillatory instability via Hopf bifurcation or voltage collapse via Saddle node bifurcation. Tap changer dynamics also have an effect on voltage stability as part of the mechanism of load restoration.

Key devices that may have significant impact on system voltage stability were recognized[1]. They include:

- Load increase or restoration characteristics,
- Tap changers,
- Generator field current (over excitation) and armature current limiters,
- AVR (primary and secondary voltage regulation including line drop compensation),
and
- HVDC control characteristics.

Properly modeling of above components is imperative for accurate voltage stability analysis.

1.4 Voltage Stability Analysis

Different voltage stability analysis tools are needed corresponding to the type of concerned disturbance, output information, and computational time requirement.

1.4.1 Power Flow Based Analysis

Basically power flow is the approximation of power system steady state under several assumptions, such as

- Bus types: PV bus, PQ bus, slack bus,
- Active and reactive power generation limits, and
- Constant power load.

Originally, power flow was used as a computationally effective way to determine power system network status under normal operation condition. Power flow based voltage stability analysis was first proposed. The voltage collapse point was determined by observing

power flow divergence corresponding to a singular Jacobian matrix. However, if the system's condition was close to a critical loading, conventional power flow calculations based on the Newton-Raphson method encountered numerical problems. Therefore, additional special techniques were designed and implemented based on traditional power flow programs. The continuation method [9,21,22] and direct method [2] have been developed to overcome these numerical problems.

Even though the numerical difficulty could be avoided by the continuation power flow[9], the power flow based analysis has the following disadvantages, due to the inaccuracy of modeling.

- Power flow based analysis is dependent on an approximated model ignoring the dynamic aspect of the generation and load components.
- Bus type assumptions are unrealistic.
- Limit constraints are not accurate enough for study system stability behavior.
- Power flow based analysis does not provide enough information for nonlinear dynamic phenomena other than maximum loadability.

These observations indicate that the criteria based on power flow based voltage stability analysis may not be accurate or may even be too optimistic. Thus, including proper dynamic models of the key devices may provide more accurate voltage stability analysis.

1.4.2 Small Disturbance Analysis

Based on the full-pledged component dynamic model, the aim of small disturbance voltage stability analysis is to determine whether a suggested operating point of a power system will remain stable with respect to a small disturbance when the system load level is increased.

To achieve this goal, the original nonlinear dynamical equations are linearized about a specified operating point, and the system matrix is calculated. Eigenvalue analysis could be conducted to provide stability related information. The eigenvalues of the system matrix determine the dynamic behavior of the system response to small disturbances. The corresponding right and left eigenvectors define the shape of the corresponding modes of response. This analysis provides helpful information on both the proximity to and the mechanism of voltage instability. However, eigen-calculation is computationally intensive. Recently, local bifurcation theory [9,11,12,15,22,26] has been applied in small disturbance analysis for the determination of the stability margin.

1.4.3 Quasi-Steady-State Analysis (QSS)

Quasi-Steady-State analysis is a simplification of multi-time-scale time domain dynamic analysis. The fast-slow time scale decomposition [5,18] is conducted to apply the singular perturbation analysis. Slow dynamics, such as load restoration characteristics and LTC, are distinguished from fast dynamics. The stiff problem associated with multi-time-scale time domain simulation is avoided.

However, there is inherent limitation on QSS. QSS is valid only under the following assumptions.

- A stable fast dynamical equilibrium exists after the disturbance.
- For large disturbances, pre-disturbance state of the system must also belong to the attraction region of the post-disturbance equilibrium of fast dynamics.
- Oscillatory instability of fast dynamics could not be observed.
- The interaction of load dynamics and other fast dynamics could not be observed.

1.4.4 Large Disturbance Analysis

Although classical voltage instability evolves over several minutes, the possibility of transient voltage instability also exists because of the characteristics of fast-response system components. When a large disturbance occurs in the system, the phenomena are usually analyzed by transient stability programs which include fast dynamic models, such as induction motors.

Voltage instability often occurs due to system dynamics of the order of tens of seconds to minutes. Dynamics include increase of load, recovery of load after disturbances, and power coordination following a loss of generation. Several approaches that are based on long-term time simulation have been developed. The time simulation is valuable in determining and demonstrating the time sequence of control and protection actions with any size of disturbance. In addition, time domain simulations are capable of studying the overall system stability and are not limited to voltage stability.

The most general method for transient and long-term analysis involves unified solution of fast (transient) and slow (longer-term) dynamics. Simultaneously solving long-term equations with short-term equations makes the problem stiff. A stiff problem is one in which the underlying physical process contains components operating on widely separated time scales, or the dynamics of some part of the process are very fast compared to the long-term time interval. Stiffness is measured by the ratio of the largest to the smallest eigenvalue.

A fixed small time step size is needed for capturing short-term dynamics. While this mitigates numerical difficulty, it still has its disadvantages. It generally requires extensive output analysis to uncover the causes that contribute to voltage instability. Although

numerical integration techniques have become more efficient, the conventional time domain dynamic simulations for long periods of time remain very computationally intensive.

Some programs use various time steps to simulate the system behavior in different time frames. A well known step size control strategy is by control of the Local Truncation Error (LTE)[5]. This control scheme is applied in EUROSTAG software[49]. However, it is costly to achieve the higher order derivative information of all the dynamic variables which are needed to estimate the LTE, especially for the power system DAE model.

1.5 Control Strategy

In power system planning and operation studies, the detection and prediction of voltage collapse is only part of the work facing the engineers. To avoid voltage collapse, it is necessary to investigate the contributing factors that lead to voltage instability. Effective controls need to be designed to prevent the system from collapse. Information about what controls are effective and where to apply them is useful. Based on the optimization technique, the control strategy could be divided into the following two categories.

1.5.1 Sensitivity Based Margin Control Optimization

Sometimes sensitivity is defined for evaluating general system performance, such as parametric sensitivity. It indirectly relates to stability since system degradation eventually will lead to collapse if no preventive measure is applied. More often, the sensitivity is defined with respect to certain stability indices, which are intended for determining the degree of stability. The stability index can be based on a given state, requiring only information from the current operating point, or based on large deviation, which also requires the knowledge of the critical point. The latter accounts for nonlinearities caused by larger

disturbance or load increase. A link between a given state index and a large deviation-based index is needed if it is desired that the sensitivity can be used quantitatively to predict the effectiveness of the particular controls applied. Using this kind of quantitative sensitivity measure, one will then be able to further apply the methodology to estimate transfer margin as limited by voltage collapse, without actually re-computing the PV curves[25,11,26]. Further, if system dynamics is of concern, the sensitivity of a stability index should be defined with respect to the DAE model of the system[11].

Optimization in conjunction with margin sensitivity could be formulated to seek the most effective and efficient control strategy. In most cases, linear programming or quadratic programming is employed [51,53]. The limitation of the approach is due to the difficulty of taking into account the component limit constraints and higher order nonlinearities.

1.5.2 Nonlinear Optimization of Margin Control

Margin boundary in multi-control parameter space is highly nonlinear. Nonlinear optimization of margin control, which is subject to limit constraints, is in demand to seek the optimal control in a wide control range. However, there is still a challenge from the numerical difficulty associated with solving optimization problems in heavy load condition. As part of this thesis work, Continuation Optimal Power Flow (COPF) is proposed to overcome the numerical difficulty.

CHAPTER 2 LITERATURE REVIEW AND SCOPE OF THE WORK

2.1 Literature Review

We reviewed the literature related to our work based on the following aspects:

- Bifurcation viewpoint
- Optimization viewpoint
- Time domain viewpoint

2.1.1 *Bifurcation Viewpoint*

Voltage collapse and oscillatory instability due to small load variations are inherently nonlinear phenomena that could be modeled by bifurcation theory from the perspective of parametric nonlinear dynamic systems. Substantial research has been conducted to help understand and analyze the mechanism of those types of instability based on bifurcation theory.

Voltage collapse is related to Saddle node bifurcation (SNB), during which system equilibrium disappears as system parameters, mostly system load, change slowly [1-3,5,6]. In recent decades, several blackouts have been recognized to be related to Saddle node bifurcation [3].

Oscillatory stability is another aspect of power system operational security. Oscillatory stability is related to Hopf bifurcation [38]. The improper tuning of generation control parameters may lead to Hopf bifurcation [24,32,35]. Nonlinear load may also lead to Hopf bifurcation [12]. References [6,33,34] presented analysis related to a 1992 disturbance on the midwestern segment of the US interconnected power system and the resulting oscillations caused by line tripping. It confirmed that the event was indeed related to a Hopf

bifurcation. Continuation based approaches have been proposed to identify these critical points [9,10,14,15,16,21,22].

Load margin is a reasonable measure of proximity to the bifurcation related instability. It is defined as the amount of additional load on a specified pattern of load increase that would cause power system instability. From this total load margin increase, the margin at individual load buses can be easily calculated from the load distribution factors. Since real power of load increase is often under concern in power system operation, the load margin is presented in MW corresponding to a specified loading scenario.

The load margin can be obtained in a variety of ways. The trivial way to obtain a new margin is to retrace the PV curve for the given contingency and scenario. Obviously this method is time consuming and less informative. References [11,23,25,26,46,47] focused on Saddle node bifurcation related to voltage stability margin estimation based on linear or quadratic margin sensitivities. Retracing of the entire PV curve for each parameter change was avoided. Dobson et al in [24] studied the sensitivities of Hopf bifurcation for various power system parameters. Margin sensitivity based methods are very useful for a quick calculation of the margin for a given change in any parameter. But the prominent sources of inaccuracy inherently associated with margin sensitivity methods make a significant impact on the reliability of the margin estimation. Parameter change, sometimes due to a contingency, may not be within a small range and hence higher non-linearity could not be neglected [21].

Oscillatory stability needs to identify critical eigenvalues. The methodologies for the calculation of critical eigenvalues for power system dynamic stability analysis have been summarized and compared in [56]. Preconditioning and iteration are the significant

components of those algorithms. Several preconditioning techniques have been presented, such as Shift-Invert Transformation, Cayley Transformation and Chebyshev Transformation. The major solution methods have been also presented, such as Power Iterations, Rayleigh Quotient Iterations, Newton, Subspace iteration and Arnoldi method. Those methods are all iteration based and involves a great volume of computation.

Venkatasubramanian et al in [33,34] presented iterative algorithms that calculated the Hopf bifurcation related segment of the feasibility boundary for a realistically large power system model. The method applied bilinear transformation of system Jacobian matrix and power method to calculate the dominant eigenvalue. A large volume of calculation associated with eigen-analysis and complicated transformation still existed.

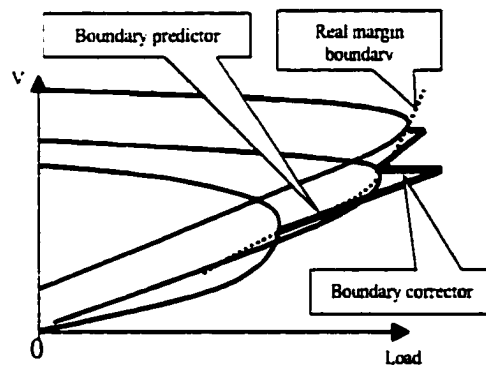


Figure 2-1: Illustration of margin boundary tracing framework

In chapter 5, this thesis presents a framework based on a differential manifold approach [36.40] that combines the identification and tracing of both Saddle node and Hopf bifurcation margin boundaries without calculating any eigenvalues. For a given base case, we first identify either saddle node or Hopf bifurcation. Then for any given control change

scenario, we can further trace the change in Saddle node or Hopf bifurcation margins. Fig. 2-1 shows the conceptual diagram of margin boundary tracing.

2.1.2 Optimization Viewpoint

As was mentioned in the previous section, prominent sources of inaccuracy inherently associated with margin sensitivity methods make a significant impact on the reliability of the margin estimation and control. In essence,

- Single point local sensitivity information has its limitations in seeking a global optimal control solution. Linear (or high order, practically limited to no more than quadratic) sensitivity information is obtained by a Taylor series expansion at the system margin point (critical point). Note that the parameter change, sometimes due to contingency, may not be within a small range and therefore the higher nonlinearity could not be neglected.
- The effect of system limits may lead to a discontinuous change in margin.

Due to the heavy nonlinear behavior shown by the stressed power system, nonlinear analysis and nonlinear global (practically, within a certain physical arrange) optimal control solutions are, in essence, required by the nature of non-linearity demonstrated by the systems near the voltage stability boundary.

There is an inherent relationship between the maximum loadability and Saddle node bifurcation in a load parameterized power system [5]. There has been a great amount of effort made to optimization based voltage stability analysis. Under certain conditions, the singularity problem could be avoided. But the difficulty of identifying an active constraint set and the possibility of divergence still exists, especially when parameter variance is not within a small range.

The Galiana group published a series of papers [27-31] on the optimal power flow based on the homotopy type continuation method. It could trace the optimal solution along a certain system scenario, based on optimization formulated with power flow equations. However, the algorithm may diverge when the sequential specified load level is close to the largest feasible load margin. The largest feasible load margin is the largest load margin a system could achieve within the control limits and security constraints.

Optimal margin boundary tracing, proposed in this thesis, avoids this divergence. Fig.2-2 shows a conceptual diagram of the optimal margin boundary tracing proposed in this paper, where u_1 and u_2 are control parameters; m_0, \dots, m_3 indicate the voltage stability margins.

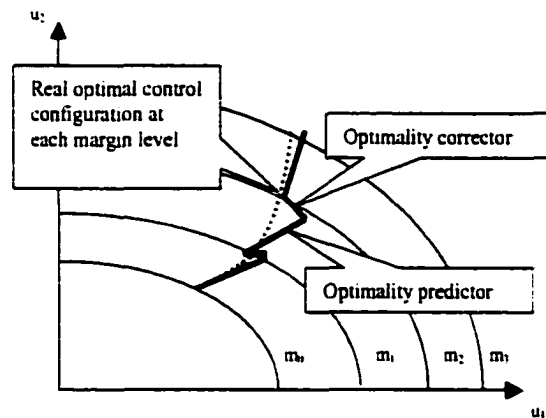


Figure 2-2: Optimal margin boundary tracing

2.1.3 Time Domain Viewpoint

The interest in voltage collapse evolution and the timing of corrective control brings in the third aspect of voltage stability analysis, time domain simulation. Time domain

simulation is among the major supporting tools for power system analysis. A variety of algorithms have been proposed for power system transient stability analysis.

A time domain solution of a large set of coupled algebraic and ordinary differential equations is an important tool for many applications in power system analysis. Time domain simulation techniques are widely used for power system analysis because of their versatility and accuracy. The set of equations is usually formulated as a set of differential algebraic equations (DAE) [5.6].

The time horizon for voltage instability dynamics varies from seconds to minutes [3]. The timing of corrective control is vital for the restoration of system stability [16.17]. Thus, transient stability and long term stability analysis have to be combined in a single program to simulate the interaction of load dynamics with generator side fast dynamics.

In recent years, a large amount of effort has been spent in this direction [41–45]. The stiff problem is solved by the use of variable step size and variable order integration algorithms. But time domain simulation algorithms with adaptable step size still encounter a divergence of solutions close to the voltage collapse point. Time scale decomposition is applied to mitigate the stiff problem. As a simplification, the quasi-steady-state DAE model was investigated in [17.18.19.20]. However, the divergence of solutions of short-term equilibrium at the neighborhood of voltage collapse still cannot be avoided.

So a more competent time domain simulation algorithm is demanded for more reliable and accurate dynamic voltage stability assessment and validation of corrective control against voltage instability.

In chapter 7, we propose a numerically well-conditioned local parameterization based time domain simulation to solve both power system multi-time scale and the quasi-steady-state DAE.

2.2 Scope of the Work

The manifold based methodologies presented in this thesis facilitate the analysis contributing to fast margin monitoring, margin control and timing of the control.

The salient features of the approach are given below:

- **Fast detection of Hopf bifurcation**

With only solving tangent vector of the test matrix: a linear transformation of system total Jacobian matrix, the Hopf bifurcation is easily detected by observing the sign change of a scalar index in the tangent vector without eigenvalue calculation. Time consuming calculation associated with eigenvalue is avoided.

- **Fast determination of voltage and oscillatory stability margin**

Continuation method is the most reliable method applied in determination of load margin for large-scale power systems. It is used in a single parameter tracing on one dimension manifold with the introduction of only one parameter (usually the loading parameter under a specified loading scenario). However, it is really time consuming to get a new voltage stability margin for every change of control configuration by retracing the entire PV curve from the base case (or operating point for online load margin monitoring). It may not be suitable for on-line voltage stability assessment.

Based on manifold and bifurcation theory, a unified formulation for a variety of bifurcation related voltage stability margin boundary tracing in multi-parameter space is originally proposed. The bifurcation related margin boundary could be traced along

any control scenario in multi-control parameter space combined with any given loading scenario. This is achieved by moving from one boundary point to the next without re-tracing the entire PV curve. This paves the way for online voltage stability assessment.

The unified boundary predictor-corrector-identifier tracing framework is originally employed to trace both voltage collapse and oscillatory stability margin boundaries, which are limited by Saddle node and Hopf bifurcations, respectively.

- **Optimal Margin Boundary Tracing with Continuation Optimal Power Flow**

Continuation optimal power flow traces optimal control to maintain specified load level. Whenever the specified load level is beyond the current margin boundary, the optimal control for extended margin boundary is calculated. Then it becomes optimization on voltage stability margin boundary manifold and actually optimal margin boundary tracing is conducted. It could automatically generate a cost based optimal control solution corresponding to a specific margin level.

- **Local Parameterization Based Unified Time Domain Simulation**

The timing of control makes a great difference in term of the amount of control. The type and amount of control the system needs to survive is quite dependent on control time and load recovery characteristics. During this process both short-term dynamics and long-term dynamics could affect the system. A unified local parameterization based time domain simulation algorithm is proposed. It could be applied in multi-time scale DAE to capture both fast and slow dynamics. It also could be applied in QSS DAE to capture both long-term dynamics and the exact short-term voltage collapse points.

Based on local parameterization, the numerical problem associated with power system DAE under heavy load condition could also be avoided.

This local parameterization based time domain simulation could adapt time step size right according to the variant rate of derivative of dynamic variable and network variable. It employs a larger integration time step size for slow dynamics and smaller step size for fast dynamics.

Analysis from any of the above perspectives finally results in the solution of a set of corresponding nonlinear equations. Numerical difficulty is always the critical problem when solving those highly nonlinear equations. Based on the differential manifold concept, a variety of natural and local parameterizations are proposed and applied in this thesis.

Note that the natural parameter introduced into the equation system does not have to be a bifurcation parameter.

- In the perspective of bifurcation, the load level scalar is introduced as bifurcation parameter, and thereby local parameterization is applied to trace either the equilibrium manifold or margin boundary manifold.
- In the perspective of optimization, the load level is a direct bifurcation parameter associated with a set of equations originated from the DAE system. However, it is the natural parameter introduced to the equations coming from the optimality condition. Therefore, local parameterization could still be applied to trace the optimal margin boundary.
- In the perspective of time domain, the integration time step size is not a bifurcation parameter at all. But it is the natural parameter associated with the solving of a set of nonlinear equations that come from the constraints of the

integration, a piecewise manifold. Therefore local parameterization could still be applied to solve for this natural parameter: integration time step size on each of the piecewise manifold. Thereby numerical problems associated with the DAE are avoided.

2.3 Organization of This Dissertation

Chapter 3 addresses the modeling of power systems for equilibrium tracing, margin boundary tracing, margin control optimization and time domain simulation.

Chapter 4 and chapter 5 address voltage stability from the perspective of bifurcation.

Chapter 4 presents power system equilibrium tracing with detection of both Saddle node and Hopf bifurcations. Note that Hopf bifurcation is detected with computationally efficient methods without eigenvalue calculation.

Chapter 5 presents the unified margin boundary tracing framework and its application to Saddle node and Hopf bifurcations.

Chapter 6 addresses voltage stability from the viewpoint of optimization. Margin control optimization with continuation optimal power flow is presented.

Chapter 7 addresses voltage stability from the perspective of time domain. Local parameterization based time domain simulation is presented. Unified algorithm is presented that could be applied in both multi-time scale and quasi-steady-state (QSS) time domain simulation to avoid numerical difficulty.

All numerical results are demonstrated with the New England 39 bus system.

Chapter 8 concludes the thesis.

CHAPTER 3 POWER SYSTEM MODELING

3.1 Formulation of the Power System DAE model

A power system is assumed to have n buses and m generators. Each generator is assumed to be equipped with the same type of excitation control system and speed governor. The formulation of power system modeling is presented in this chapter. The most commonly used power system notations are adopted here.

3.1.1 Synchronous Generator

Without loss of generality, the rotor angle of the m_{th} generator is chosen as the system angle reference. This choice of reference is different from the conventional slack bus selection. No assumptions are necessary for choosing such a reference. When stator transients are ignored, the two-axis model [4.48] describing the synchronous machine dynamics can be given as:

$$\dot{\delta}_i = (\omega_i - \omega_m)\omega_0 \quad i = 1, \dots, m-1 \quad (3.1)$$

$$\omega_i = M_i^{-1} [P_m - D_i(\omega_i - \omega_m) - (E'_{qi} - X'_{di} I_{di}) I_{qi} - (E'_{di} + X'_{qi} I_{qi}) I_{di}] \quad i = 1, \dots, m \quad (3.2)$$

$$E'_{qi} = T_{d0i}^{-1} [E_{fdi} - E'_{qi} - (X_{di} - X'_{di}) I_{di}] \quad i = 1, \dots, m \quad (3.3)$$

$$E'_{di} = T_{q0i}^{-1} [-E'_{di} + (X_{qi} - X'_{qi}) I_{qi}] \quad i = 1, \dots, m \quad (3.4)$$

where ω_m is the system frequency, ω_i is the machine frequency, namely, generator angular speed and ω_0 is the system rated frequency (377.0 rad /sec). I_{di} and I_{qi} are direct axis

and quadrature axis currents respectively; E'_d and E'_q are transient direct axis and quadrature axis EMF respectively; T_{d0} and T_{q0} are direct axis and quadrature axis open circuit time constants respectively; X'_d and X'_q are direct axis and quadrature axis transient reactances and R_s is armature resistance of the machine; M is inertia constant and D is the damping constant of the machine. All the quantities are per unit except ω .

Interface voltage equations to the network are given as follows:

$$E'_{qi} = V_i \cos(\delta_i - \theta_i) + R_{si} I_{qi} + X'_{di} I_{di} \quad (3.5)$$

$$E'_{di} = V_i \sin(\delta_i - \theta_i) + R_{si} I_{di} - X'_{qi} I_{qi} \quad (3.6)$$

where V_i and θ_i are bus voltage and angle respectively.

The machine currents I_{di} and I_{qi} can be eliminated by solving the generator interface equations to the network. Hence,

$$I_{di} = [R_{si} E'_{di} + E'_{qi} X'_{qi} - R_{si} V_i \sin(\delta_i - \theta_i) - X'_{qi} V_i \cos(\delta_i - \theta_i)] A_i^{-1} \quad (3.7)$$

$$I_{qi} = [R_{si} E'_{qi} - E'_{di} X'_{di} - R_{si} V_i \cos(\delta_i - \theta_i) - X'_{di} V_i \sin(\delta_i - \theta_i)] A_i^{-1} \quad (3.8)$$

$$A_i = R_{si}^2 + X'_{di} X'_{qi} \quad (3.9)$$

Note that (3.1) does not include the differential equation for δ_m , and that all the angles here and henceforth are relative angles with respect to the m th generator's rotor angle.

3.1.2 Excitation Control System

The simplified IEEE type DC-1 excitation system [4] as shown in Fig.3-1 is used here. The corresponding mathematical model is

$$E_{fdi} = T_{ei}^{-1} [V_{ri} - [S_{ei}(E_{fdi})] E_{fdi}] \quad i = 1, \dots, m \quad (3.10)$$

$$V_n = T_{av}^{-1}[-V_n + K_{av}(V_{refi} - V_n - R_n)] \quad i = 1, \dots, m \quad (3.11)$$

If

$$V_{n,\min} \leq V_n \leq V_{n,\max}, \quad V_{psu} = 0 \quad (\text{at steady state})$$

$$R_{fi} = T_{fi}^{-1}[-R_{fi} - [K_{ei} + S_{ei}(E_{fdi})]K_{fi}E_{fdi}/T_{ei} + K_{fi}V_n/T_{ei}] \quad i = 1, \dots, m \quad (3.12)$$

where V_{refi} is the reference voltage of the automatic voltage regulator (AVR); V_n and R_{fi} are the outputs of the AVR and exciter soft feedback; E_{fdi} is the voltage applied to generator field winding; T_{av} , T_{ei} and T_{fi} are AVR, exciter and feedback time constants; K_{av} , K_{ei} and K_{fi} are the gains of AVR, exciter and feedback; $V_{n,\min}$ and $V_{n,\max}$ are the lower and upper limits of V_n .

3.1.3 Prime Mover and Speed Governor

Fig. 3-2 shows the block diagram for a simplified prime mover and speed governor. Two differential equations are involved to describe the dynamics when no μ_i limit is hit.

$$P_{mi} = T_{hi}^{-1}(\mu_i - P_{mi}) \quad i = 1, \dots, m \quad (3.13)$$

$$\mu_i = T_{gi}^{-1}[P_{gi} - (\omega_i - \omega_{ref})/R_i - \mu_i] \quad \text{if } \mu_{i,\min} \leq \mu_i \leq \mu_{i,\max} \quad i = 1, \dots, m \quad (3.14)$$

where $P_{gi} = P_{gi}^0(1 + K_{gi}\mu)$ is the designated real power generation; P_{gi}^0 is its setting at base case; K_{gi} is the generator load pick-up factor that could be determined by AGC, EDC or other system operating practices; P_{mi} is the mechanical power of prime mover and

μ_i is the steam valve or water gate opening; R_i is the governor regulation constant, representing its inherent speed-droop characteristic; ω_{ref} ($=1.0$) is the governor reference speed; T_{chl} and T_{gt} are the time constants related to the prime mover and speed governor respectively; $\mu_{i,min}$ and $\mu_{i,max}$ are the lower and upper limits of μ , where a parameter μ is introduced to designate the system load level. At the base case, μ equals zero.

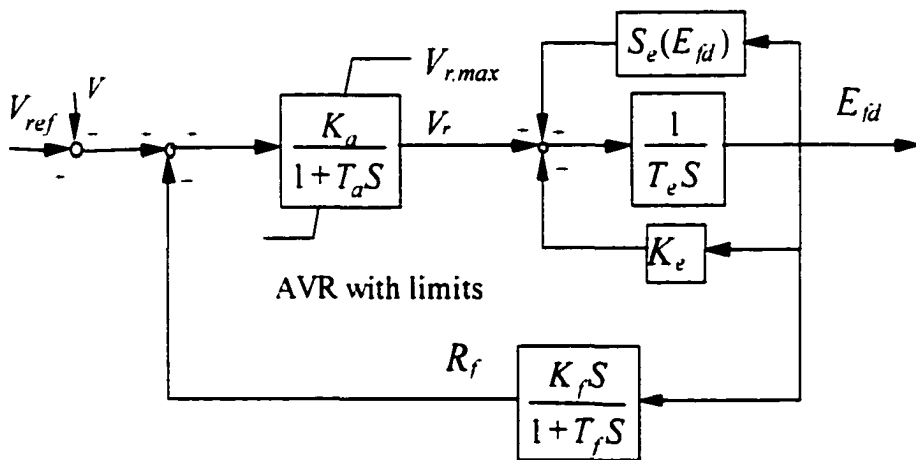


Figure 3-1: The IEEE type DC-1 excitation system

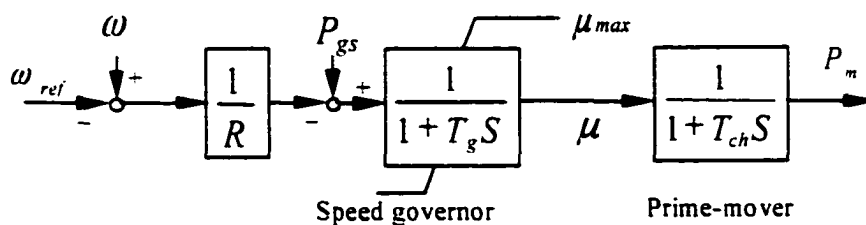


Figure 3-2: The simplified speed governor and prime mover

3.1.4 Nonlinear Load Model

The voltage and frequency dependent load is modeled as follows for all the load buses.

$$\begin{cases} P_{li} = P_{li0} (V_i / V_{i0})^{\alpha_i} [1 + K_{lpi} (\omega_m - \omega_r)] \\ Q_{li} = Q_{li0} (V_i / V_{i0})^{\beta_i} [1 + K_{lqi} (\omega_m - \omega_r)] \end{cases} \quad i = 1, \dots, m \quad (3.15)$$

where P_{li0} and Q_{li0} are the active and reactive powers consumed by the load at the nominal voltage V_i and frequency ω_r ($=1.0$). The frequency dependent term is included to prevent the equilibrium computation from divergence in case all the generators reach their maximum real power limits due to load increase or generator outages. Here K_{lpi} and K_{lqi} are the load changing factors with respect to system frequency.

3.1.5 LTC Model

Continuous on Load Tap Changer (LTC) model is taken.

Assume there is an LTC between bus i and j .

$$V_i = r V_j \quad (3.16)$$

$$T_i \dot{r} = V_j^{ref} - V_i \quad (3.17)$$

where r is the ratio position of an LTC; i is the number of LTC; V_j^{ref} is the reference voltage at the LTC regulated bus j ; T_i is the time constant.

3.1.6 HVDC Model

A simplified version of the AC/DC power flow [50] is incorporated in algebraic equations of the DAE modeling of power systems. This simple version, nevertheless, has all of the capabilities of established power flow methods. For this simplified version of the AC/DC power flow, the usual assumptions of continuous converter transformer tap, scheduled voltage control with a certain minimum control angle and fixed voltage margins at

those terminals with a scheduled current or power control, as in established methods, are made.

3.1.6.1 Basic equations

The converter model is based on the relationship between the ripple-free average DC quantities and the fundamental frequency AC quantities.

Based on the per unit system, the following equations can be written for every converter terminal. For the k_{th} converter, its DC voltage equation in terms of its tap a_k , AC voltage V_k , control angle θ_k , commutation resistance R_{ck} , and the DC current I_{dk} is

$$V_{dk} = a_k V_k \cos \theta_k - R_{ck} I_{dk} \quad (3.18)$$

Its DC power equation is

$$P_{dk} = V_{dk} I_{dk} \quad (3.19)$$

Neglecting the losses in the k_{th} converter and its transformer and equating the expressions for powers on the AC side and DC side, the equation obtained for its power factor angle ($\psi_k - \xi_k$) is

$$V_{dk} = a_k V_k \cos(\psi_k - \xi_k) \quad (3.20)$$

For the simple circuit representation of the converter transformer, the equation for the reactive power flowing from the AC bus into the k_{th} converter terminal is

$$Q_k = P_{dk} \tan(\psi_k - \xi_k) \quad (3.21)$$

3.1.6.2 Converter controls equations

A practical operating scheme for a multi-terminal DC system using local terminal controls is to have the DC system voltage determined at one terminal – the voltage

controlling terminal. The other terminals are provided with scheduled power or current settings.

To keep the reactive power consumption of the converters and the losses in the snubber circuits low, the control and reliable commutation, a minimum control angle should be maintained. Typical values of the minimum ignition angle α^{\min} range from 5° to 7° . Those of the minimum extinction angle range from 15° to 20° .

In most power flow methods, the voltage controlling terminal that is operating at the scheduled voltage V_j^{sch} is also assumed to be operating with a certain minimum control angle θ^{\min} . Thus if the m terminal is the voltage controlling terminal, its DC voltage and control angle are

$$V_{dm} = V_j^{sch} \text{ and } \theta_m = \theta_m^{\min}$$

For the terminal with a scheduled current or power control, it is common practice to coordinate the tap control with the phase control so that the terminal will operate at some DC voltage below its own minimum ignition or extinction angle characteristic. This is done in order to avoid frequent mode shifts from occurring with normal AC voltage fluctuations. Typically, a 3% voltage margin is provided; with the average α^{\min} or θ^{\min} given above, typical values of the control angles α and γ are 15° and 20° , respectively, for those DC terminals with a scheduled current or power control. This typical voltage margin of 3%, in practice, can be considered in the power flow computation by modifying the DC voltage equations for such terminals with a coefficient of $K=0.97$.

Thus, if the k_{th} terminal has a scheduled current control, its DC current is equal to the scheduled current I_{dk}^{sch} , that is

$$I_{dk} = I_{dk}^{sch}$$

and its DC voltage equation is

$$V_{dk} = K_k [a_k V_k \cos \theta_k^{mn} - R_{ck} I_{dk}] \quad (3.22)$$

Similarly, if the k_{th} terminal has a scheduled power control, its DC power is equal to the scheduled power P_{dk}^{sch} , that is

$$P_{dk} = P_{dk}^{sch}$$

and its DC voltage equation is also given by (3.22).

3.1.6.3 DC network equations

The equations for the DC network can be formulated to suit the procedure that is used to solve them. Since multi-terminal DC networks in the near future are unlikely to have greater than 30 buses, the present choice is the R_{bus} Gauss-Seidel method.

Although the algorithm is applicable to a general bipolar network, there is no loss in generality by considering a symmetrically m-terminal bipolar system that can be economically represented as an equivalent m-terminal monopolar system.

If the buses are numbered so that the m_{th} terminal is the voltage controlling terminal, and its network terminal is also the reference bus for the R_{bus} , the voltage equations for the DC network of the equivalent m-terminal monopolar system can be written as

$$V_{dk} = \sum_{i=1}^{m-1} r_{ki} I_{di} + V_{dm}, \quad k = 1, \dots, (m-1) \quad (3.23)$$

where r_{ki} 's are elements of the DC network's R_{bus} with the terminal of the m_{th} terminal as its reference.

Note that V_{dm} is the DC voltage at the terminal of the voltage controlling terminal: V_{dm} is equal to the scheduled voltage V_d^{sch} of that terminal.

3.1.7 Network Power Equations

Corresponding to the above models, the network equations can be written as:

$$\begin{cases} 0 = P_{gr} - (1 + K_{lp_i, \mu})P_i - P_n \\ 0 = Q_{gr} - (1 + K_{lq_i, \mu})Q_i - Q_n \end{cases} \quad i = 1, \dots, n \quad (3.24)$$

Where

$$\begin{cases} P_n = \sum_{k=1}^n V_i V_k Y_{ik} \cos(\theta_i - \theta_k - \varphi_{ik}) \\ Q_n = \sum_{k=1}^n V_i V_k Y_{ik} \sin(\theta_i - \theta_k - \varphi_{ik}) \end{cases} \quad i = 1, \dots, n \quad (3.25)$$

and

$$\begin{cases} P_{gr} = I_{di} V_i \sin(\delta_i - \theta_i) + I_{qi} V_i \cos(\delta_i - \theta_i) \\ Q_{gr} = I_{di} V_i \cos(\delta_i - \theta_i) - I_{qi} V_i \sin(\delta_i - \theta_i) \end{cases} \quad i = 1, \dots, m \quad (3.26)$$

P_{gr} and Q_{gr} are the generator output powers, which are primarily determined by the inherent characteristics of the speed governor and the AVR regulations. They will change if real power generation rescheduling and secondary voltage control are applied. P_n and Q_n are the powers injected into the network at bus i . K_{lp_i} and K_{lq_i} are the load changing factors specified for bus i . It should be noted that (3.24) is generic in the sense that it is used for all of the buses.

3.1.8 Modeling of Limit Constraints

It is very important to adequately address the system limits when studying voltage stability. Voltage collapse often occurs as a consequence of some devices hitting their limits in a heavily stressed power system. For a synchronous generator, its real power output limit, the armature current limit and the field current limit are especially important and should be appropriately considered. In this work, we take full advantage of the DAE formulation to accurately implement all of these three limits. Implementation of these limits is given in [10].

3.1.8.1 Generator real power limits

The active power output of a generator is limited by equivalently enforcing the governor output limit $\mu_{i,\min}$ or $\mu_{i,\max}$ in (3.13-3.14). Once the governor output reaches its limit, the generator will no longer be allowed to pick up any additional load, and will stop participating in the system frequency regulation. In the meantime, μ will stop being a state variable and become a control input and stay at its limits.

3.1.8.2 Generator reactive capability limits

In voltage stability analysis, it is important to consider the reactive capability limits of generators. Generators are rated in terms of the maximum MVA output, at a specified voltage and power factor, that they can carry continuously without overheating. The continuous reactive power output is limited by the armature current and field current limits. Static voltage stability analysis using power-flow program usually assumes a fixed reactive power limit in simulations. However, the reactive power limit varies depending on the system operating conditions.

The generator capability curve is shown in Fig.3-3[6]. It is a plot of P versus Q , together with the limits corresponding to maximum turbine output and underexcitation limiter operation. Lines of constant armature current I_a appear as lines of constant

$$S = V_t I_a \quad (3.27)$$

which are concentric circles around the origin. Lines of constant field current corresponding to lines of constant E_a are shown as circles of radius

$$E_a V_t / X \quad (3.28)$$

centered on the point

$$Q = \frac{V_t^2}{X} \quad (3.29)$$

The armature current limit appears as the circle corresponding to the rated I_a or rated KVA, and the field current limit appears as a circle corresponding to rated E_a .

Point R in Fig.3-3 corresponds to an operation at rated power. This is the intersection of the turbine and armature limits under rated voltage. In the case shown, $E_{a\text{lim}}$ has been chosen so that the field limit also passes through point R . In practice the three different kinds of curves, although very close, may not intersect exactly.

The figure also shows the effect of the terminal voltage. A larger terminal voltage yields a larger armature limit and a slightly larger field current limit as well. Any point that lies within both circles is a safe operating point for the generator.

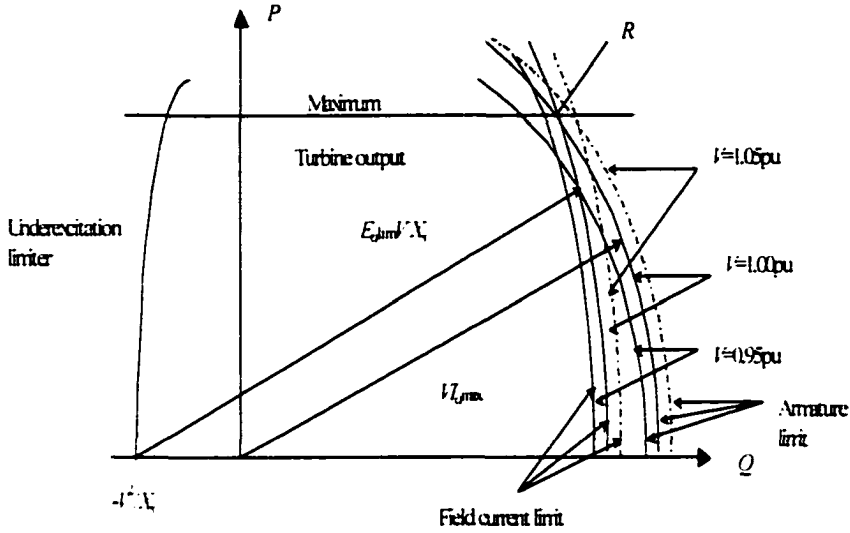


Figure 3-3: Capability curves (saliency and saturation neglected)[6]

3.1.8.3 Generator field and armature current limits

The reactive power output of a generator is dependent on its terminal voltage, which is controlled by the generator AVR. Hence, under normal conditions, the generator reactive power output can be adjusted by regulating AVR reference voltage.

However, once the generator field current limit is reached, the AVR will lose its ability to maintain the generator terminal voltage, and the reactive power output can no longer be regulated. Here we show that the field current limits and the armature current limits both could be accurately represented by implementing the AVR output limits $V_{t,max}$. Note that the field current limit here is referred to as the maximum allowable current for the generator at steady state, with the inverse-time acting characteristic neglected.

The following conditions hold at a steady state with the saturation effects of the exciter ignored.

$$E_{fd} = E_{qt} + (X_{dt} - X_{dt}')I_{dt} \approx E_{qt} = X_{adt} I_{fd} \quad (3.30)$$

$$V_r = (K_{ei} + S_{ei})E_{fd} \quad (3.31)$$

Here E_{fd} is the generator internal induced quadrature axis voltage, which is proportional to the field current I_{fd} . The state variable V_r (AVR output) is also proportional to the generator field current. Thus the field current limit $I_{fd,max}$ can be directly implemented by enforcing the fixed AVR output limit, denoted by

$$V_{r,max} = (K_{ei} + S_{ei})X_{ad}I_{fd,max} \quad (3.32)$$

When V_r is fixed at a certain value, the reactive power will be limited indirectly, or at least not increased exponentially, when approaching voltage collapse[10].

$$Q_{gr,max} = [V_{r,a,max}V_r(X_{qi} \cos(\delta_i - \theta_i) - R_u \sin(\delta_i - \theta_i)) - V_r^2(X_{qi} \cos^2(\delta_i - \theta_i) + X_{di} \sin^2(\delta_i - \theta_i))]/(X_{di}X_{qi} + R_u^2) \quad (3.33)$$

Similarly, for the armature current limit, we can also indirectly implement it by enforcing the AVR output limit.

The maximum limit for the generator reactive output, with respect to the armature current limit, can be determined as

$$Q_{gr,max} = \sqrt{V_r^2 I_{a,max}^2 - P_{gr}^2} \quad (3.34)$$

Hence, when the current reactive power output Q_{gr} is found greater than its allowed limit, it indicates that the armature current limit $I_{a,max}$ has been exceeded. To keep the armature current below its limit, we can impose the AVR output limit to reduce the reactive power output.

Since the system equilibrium solution varies when the AVR output limit is enforced, an iterative scheme is applied to update $V_{r,a,max}$ at each continuation step so that the armature

current can stay within limits. In (3.33), the terminal bus voltage and angle are known from the previous iteration for a particular system loading level.

Similar to the governor hitting its output limits, once the AVR reaches its output limit, either due to the generator field current limitation or due to the armature current limitation, the state variable V_r will immediately become a control input, staying at $V_{r,d,max}$ or $V_{r,fd,max}$. If we still solve the remaining equations that make up the DAE system with the same control inputs, there will be no solution. This is because when the system load further increases, in order to continuously keep V_r at the limiting value, the corresponding excitation reference voltage V_{refi} has to be reduced[10]. The decrease of exciter reference voltage reflects the inability of the generator to keep pace with the load increase. Similar modifications are needed when a governor hits its limit.

3.1.9 Power System DAE Model

The above differential and algebraic equations are commonly known as a DAE representation of a power system. In a compact form, they can be simply denoted as

$$\dot{X} = F^0(X, Y, Z, U) \quad (3.35)$$

$$0 = G^0(X, Y, Z, U) \quad (3.36)$$

The function F^0 describes the dynamics associated with the generators, the excitation systems, the prime movers and the speed governors. The function G^0 represents the network power balance equations. The state vector X , algebraic vector Y , control vector U and parameter vector Z contain the following variables:

$$\begin{aligned} X &= (\delta, \omega, E_q, E_d', P_m, \mu, E_{fd}, V_r, R_f) \\ Y &= (V, \theta), \quad U = (V_{ref}, P_{ex}, \dots), \quad Z = (P_i, Q_i) \end{aligned} \quad (3.37)$$

In short, X contains all the system state variables; Y includes the algebraic variables; U is the control vector, whereas Z characterizes system loading condition.

3.2 Bifurcation Modeling of Power System Dynamics

For a dynamic system, parameterized by a single or a set of static parameters, bifurcations occur when the character of equilibrium changes within an arbitrary small local neighborhood of a critical parameter set. These static parameters are defined as bifurcation parameters. Note that the prerequisite condition of bifurcation parameters is that their derivatives always equal zero. That is, they are out of the dynamic variable set that characterizes the system state.

The bifurcation model has been introduced into voltage stability analysis. Load driven system instability is studied with load condition related parameters, such as constant load or nominal value of voltage dependent load, chosen as bifurcation parameter μ .

In a power system DAE model, a change in equilibrium character with respect to bifurcation parameter is often effectively studied by analyzing changes in the eigenvalues of $A_n(\mu) = F_X^0 - F_Y^0(G_Y^0)^{-1}G_X^0$ in response to parameter variations.

The various types of bifurcation points will generally form surfaces or manifolds in a multidimensional parameter space. These surfaces serve as boundaries in the parameter space separating regions wherein a certain type of system operation (as characterized by equilibria and trajectories) persists. A point on such a surface can be identified by a single bifurcation parameter $\mu = \mu_0$. These bifurcations are classified as codimension one. Only codimension one local bifurcations are discussed here.

There are two major codimension one bifurcations studied in power system dynamics. They are Saddle node bifurcation and Hopf bifurcation.

3.2.1 Saddle Node Bifurcation

When Saddle node bifurcation occurs, the Jacobian matrix of the system $A_{n+1}(\mu_0)$ has a simple eigenvalue and there is no other eigenvalue on the imaginary axis. The equilibrium ceases to exist when μ moves beyond μ_0 . Correspondingly, in the state space x , two equilibriums approach each other as μ approaches μ_0 ; then at μ_0 they merge in a nonhyperbolic equilibrium (with a zero eigenvalue).

Under certain additional transversality (non-degenerate) conditions, the presence of the simple zero eigenvalue of the Jacobian essentially characterizes this bifurcation. In second-order systems, this bifurcation corresponds to the annihilation of a saddle point and a node, hence the name saddle-node bifurcation.

3.2.2 Hopf Bifurcation

When Hopf bifurcation occurs, the Jacobian matrix A_{n+1} of the system has a simple pair of purely imaginary eigenvalues and there are no other eigenvalues on the imaginary axis. As the parameter changes, certain inequality conditions need to hold. These ensure that this pair of critical eigenvalues crosses the imaginary axis. They can be formulated as

$$\frac{\partial}{\partial \mu} \text{Re}[\lambda(\mu)] \neq 0$$

where $\text{Re}(\lambda)$ denotes the real part of the eigenvalue λ , which moves across the imaginary axis, and $\partial/\partial\mu$ denotes the derivative with respect to the bifurcation parameter μ .

Typically, this means that for $\mu \neq \mu_0$ the system has an equilibrium and a closed trajectory; a limit cycle exists near this equilibrium for one side of the parameters. This limit cycle can be unstable (or stable), that is, trajectories diverge (converge) from (to) it, from both the inside and the outside. The inside trajectories converge to (diverge from) a stable internal equilibrium point. As μ approaches the critical value, μ_0 , the limit cycle shrinks into the stable equilibrium within. After passing μ_0 , only the unstable region outside the limit cycle survives, now a regular (hyperbolic) unstable equilibrium point. Hence the local effect is that the stability of the equilibrium at the origin is destroyed at μ_0 . Conversely, there may be an unstable equilibrium surrounded by a stable limit cycle in the right-half plane, and a single real stable node on the left. This, then, is known as a supercritical Hopf bifurcation. Therefore, the supercritical Hopf bifurcation corresponds to a transition in the system operating condition, from a small-signal stable equilibrium point for $\mu < \mu_0$ to a small-signal stable limit cycle for $\mu > \mu_0$. That is, when the system undergoes a supercritical Hopf bifurcation at $\mu = \mu_0$, the system operating condition changes to sustained oscillation for $\mu > \mu_0$. This type of supercritical Hopf bifurcation appears and plays a fundamental role in the oscillating event experienced by Union Electric in 1992[6.33]. Hopf bifurcation is classified as subcritical if the dynamic orbit shrinks into a stable equilibrium that disappears and only an unstable equilibrium survives. For a supercritical Hopf bifurcation, this scenario is reversed. In this case, a stable equilibrium becomes unstable, and a stable periodic orbit is created at the bifurcation.

3.2.3 Comparison with Time Domain Simulation

A bifurcation model based analysis assesses system stability by capturing the character change of equilibrium, thereby avoiding time domain simulation. But it could not present information related to timing issue of how load dynamics affect overall system stability. And if equilibrium character change with respect to the variance of bifurcation parameter is detected, bifurcation based analysis could not determine the critical time to apply corrective control. Time domain simulation is still needed for overall stability assessment and timing of control.

3.3 Manifold Models in Power Systems

Mathematical models of many, practical and important scientific and technical problems involve differentiable manifolds. Differentiable manifolds are implicitly defined as the solution sets of systems of nonlinear equations [36].

3.3.1 Manifold

Assume a dynamic system is presented as

$$\dot{z} = F(z, \lambda), \quad F : R^m \times R^d \mapsto R^m \quad (3.38)$$

Where F is a sufficiently smooth mapping, $z \in R^m$ is a state variable, and $\lambda \in R^d$ is a parameter vector. A computational study of equilibria leads to the nonlinear equations of

$$F(z, \lambda) = 0 \quad (3.39)$$

Interest often centers on determining the behavior of the solution under variation of λ . The zero set $M = \{(z, \lambda) \in R^m \times R^d : F(z, \lambda) = 0\}$ has the structure of a submanifold of dimension d of the product $R^m \times R^d$ of state and parameter space. A computational analysis

could be conducted on the concerned manifold about the singular points on M or other dynamic behavior. In power systems, the dynamical systems are modeled by differential-algebraic equations (DAE). Such DAE is known to be closely related to ordinary differential equations (ODE) on implicitly defined differentiable manifolds [52].

In fact, one of the basic computational problems arising in connection with any implicitly defined manifold is exactly the construction of certain parameterizations and requires the solution of certain systems of nonlinear equations.

3.3.2 Natural Parameterization

In many applications certain quantities are naturally identified as parameter. This means that we have an intrinsic splitting, which includes a d -dimensional parameter space Λ and a state space Y .

$$Y \oplus \Lambda, \dim \Lambda = d$$

This is a natural parameter splitting of original variable space. It is natural to attempt to use the parameter space Λ as the coordinate space of a local coordinate system.

For some cases, the natural parameterization may be not suitable to be a local parameterization. In these cases singularity is always encountered while solving for the solution of nonlinear equation system.

3.3.3 Local Parameterization [36]

The d -dimensional linear subspace $S = \ker DF(x_c, \mu_c)$ of R^{m-d} depends only on M and the particular point on M . This space S is the tangent space of M at x_c and is denoted by $T_{x_c} M$.

The local parameterization could be based on tangent space $T_x M$. This could avoid singularity encountered by natural parameterization. We assume that the vectors $u_1, \dots, u_{d-1} \in R^{m-d+1}$ form an orthonormal basis of the given coordinate subspace T of M at x_c . Then the matrix representation of the mapping U is the $(m+d) \times d$ matrix with the vector u_1, \dots, u_{d-1} as columns. This matrix is denoted by U .

Then, in component form, the nonlinear mapping H assumed the form [36]

$$H : R^{m+d} \mapsto R^{m+d}, H(x) = \begin{pmatrix} F(x) \\ U^T(x-x_c) \end{pmatrix}, \forall x \in E \subset R^{m+d}, \text{ where } F(x) \text{ is the column}$$

vector consisting of the m components of F evaluated at x . By definition of φ we have

$$H(\varphi(y)) = Jy, \quad \forall y \in v^d \quad (3.40)$$

Thus, the evaluation of $x = \varphi(y)$ for given $y \in v^d$ requires the solution of the nonlinear system of equations

$$H(x) \equiv \begin{pmatrix} F(x) \\ U^T(x-x_c) \end{pmatrix} = \begin{pmatrix} 0 \\ y \end{pmatrix} \quad (3.41)$$

For general cases, the Jacobian matrix

$$DH(x) = \begin{pmatrix} DF(x) \\ U^T \end{pmatrix} \quad (3.42)$$

is nonsingular in an open neighborhood of $x = x_c$.

For the solution of the nonlinear system, a chord Newton method works well in practice [36].

3.3.4 Manifold Model in Power Systems

Different manifold modeling is proposed depending on how the set of nonlinear equations is formulated. They thereby have different meanings and serve different objectives in power systems.

Power system equilibrium manifold is defined in Chapter 4 for power system equilibrium tracing.

Bifurcation related stability margin boundary manifold is a submanifold of power system equilibrium manifold and is defined in Chapter 5 for unified margin boundary tracing.

Optimal margin boundary manifold is a submanifold of stability margin boundary manifold and is defined in Chapter 6 for optimal margin control tracing.

Piecewise integration constraint manifold is defined in Chapter 7 for local parameterization based multi-time-scale time domain simulation.

The advantage of the approach presented in this thesis is that the methodology for all these formulations is same. It employs a local parameterization based predictor-corrector approach to trace all these manifolds.

CHAPTER 4 POWER SYSTEM EQUILIBRIUM TRACING WITH DETECTION OF BOTH SADDLE NODE AND HOPF BIFURCATIONS

4.1 Natural Parameterization of Load Parameter Space for Power System Equilibrium Tracing

The equilibrium of power system DAE model (3.35-3.36) is confined by

$$\begin{cases} 0 = F^0(X, Y, Z, U) \\ 0 = G^0(X, Y, Z, U) \end{cases} \quad (4.1)$$

Which defines the equilibrium manifold of the power system. The conventional power flow solution is simply a point on this manifold corresponding to a certain operating condition. It could be regarded as an intersection point of the equilibrium manifold and a hyper-plane defined by a system condition. The power system DAE (4.1) is naturally parameterized by load parameters Z and control variables U .

Power system equilibrium manifold tracing is, in general, under fixed control configuration. Therefore, in this chapter, U is not considered as a parameter set of the power system DAEs. Only load parameters parameterize the power system equilibrium manifold.

Based on the loading scenario, the loading parameter space could be unified by a scalar μ to characterize the system loading pattern.

$$\begin{cases} P_{i0} = (1 + KL_{ip}\mu)P_{i0} \\ Q_{i0} = (1 + KL_{iq}\mu)Q_{i0} \end{cases} \quad (4.2)$$

where P_{i0} and Q_{i0} represent the initial loading conditions at base case where μ is assumed to be zero. KL_{ip} and KL_{iq} indicate the rate of load change at bus i as μ changes.

Correspondingly, a specified generation scenario is given as follows.

$$P_{gi} = (1 + KL_{gi}\mu)P_{gi0} \quad (4.3)$$

where P_{gi0} is the active generation at bus i in the base case and KL_{gi} is the generator load pick-up factor that could be determined by AGC, EDC or other system operation practices.

After this transformation, the equilibrium manifold of power system DAE becomes

$$\begin{cases} 0 = F(X, Y, \mu) \\ 0 = G(X, Y, \mu) \end{cases} \quad (4.4)$$

4.2 Equilibrium Manifold of Power System and Transverse Difficulty

The equilibrium is the solution of a set of nonlinear equations. It could be calculated by the Gauss-Sedel method or the Newton-Raphson method (or their derivatives). The Newton-Raphson type of method is widely used due to its super-linear convergence rate. But when load stress on power system is increased, both methods have difficulty converging, however close the initial guess is. This is due to the folding of the equilibrium manifold over the load parameter. It is difficult to converge to the intersection point of the equilibrium manifold and the original cut hyper-plane defined by the system generation and loading condition. Therefore when the power flow solution diverges, it is not clear whether it is caused by the nonexistence of system equilibrium or numerical problem coming from the conventional power flow algorithm. The voltage collapse point coincident with the fold point cannot be determined by conventional power flow solution. If this bifurcation is also associated with heavy load condition, the equilibrium manifold transverse difficulty also makes the location of oscillatory instability difficult or impossible.

4.3 Initialization of Power System Equilibrium Tracing

To start a power system equilibrium tracing, we need initial conditions that are defined by the following variables at all buses

$$\delta, \omega, E_d, E_q, E_{fd}, V_r, R_f, I_d, I_q, V, \theta$$

The solution from power flow provides

$$V, \theta$$

at all buses. The remaining values are obtained as shown in the following paragraphs.

Assuming i th generator bus, the first step in computing the initial conditions is normally the calculation of the generator currents from stator and network equation as

$$I_{i_s} e^{j\theta} = \frac{P_{i_s} - Q_{i_s}}{V_i e^{-j\theta}} \quad (4.5)$$

Then the relative machine rotor angles can be obtained from (4.6)

$$\delta_i = \text{angle of } (V_i e^{j\theta} + (R_s + jX_q) I_{i_s} e^{j\theta}) \quad (4.6)$$

With these quantities, the remaining dynamic and algebraic states can be found by

$$I_d + jI_q = I_{i_s} e^{j(\theta - \delta - 90^\circ)} \quad (4.7)$$

$$V_d + jV_q = V_i e^{j(\theta - \delta - 90^\circ)} \quad (4.8)$$

followed by E_{fd} from the stator and flux equation:

$$E_{fd} = X_d I_d + V_q + R_s I_q \quad (4.9)$$

With this field voltage, R_f , V_R , and V_{ref} can be found from the exciter equations as

$$R_f = \frac{K_f}{T_f} E_{fd} \quad (4.10)$$

$$V_r = (K_e + S_e(E_{fd}))E_{fd} \quad (4.11)$$

$$V_{ref} = V_t + \frac{V_r}{K_a} \quad (4.12)$$

This initial value of E'_{qi} and E'_{di} are then obtained from the flux equations:

$$E'_{qi} = -(X_{di} - X'_{di})I_{di} + E_{di} \quad (4.13)$$

$$E'_{di} = -(X_{qi} - X'_{qi})I_{qi} \quad (4.14)$$

This completes the computation of all dynamic state initial conditions.

4.4 Continuation Method with Local Parameterization

So far two methods, namely, direct and continuation methods, have been applied to detect voltage collapse [9,9b,15,16,19,22]. This section extends the application of the continuation method to the power system DAE formulation. The system equilibrium manifold defined by (4.4) could be traced, according to a scheduled scenario parameterized by μ from base case up to the point where dynamic voltage collapse associated with the saddle node bifurcation occurs.

The continuation method involves the process of prediction and correction. In the predictor, the tangent vector is solved from

$$\begin{bmatrix} F_X & F_Y & F_\mu \\ G_X & G_Y & G_\mu \\ e_i^T \end{bmatrix} \begin{bmatrix} dX \\ dY \\ d\mu \end{bmatrix} = \begin{bmatrix} 0 \\ 0 \\ \pm 1 \end{bmatrix} \quad (4.15)$$

Once the prediction is made with the tangent vector, the following correction is performed to find the equilibrium point.

$$\begin{bmatrix} F_X & F_Y & F_\mu \\ G_X & G_Y & G_\mu \\ & e_k^T & \end{bmatrix} \begin{bmatrix} \Delta X \\ \Delta Y \\ \Delta \mu \end{bmatrix} = - \begin{bmatrix} F \\ G \\ 0 \end{bmatrix} \quad (4.16)$$

where $[dX^T, dY^T, d\mu]^T$ is the tangent vector. e_k is a column unit vector with all the elements equal to zero except for the k_{th} one, which corresponds to the current continuation parameter. Since F_μ and G_μ cannot be null vectors at the same time even at the base case ($\mu=0$), the singularity of the augmented Jacobian matrix can be easily avoided by the appropriate selection of the continuation parameter. To speed up the computing, the same Jacobian matrix can be used in (4.15) and (4.16). However, if some of the variables hit their limits the Jacobian matrix have to be updated to achieve a better convergence.

From (4.15), we can see that the component of the tangent vector actually indicates some kind of sensitivity of the system variables to the current continuation parameter. Since μ is introduced to parameterize the system generation and load level, it increases monotonically to the maximum value. Hence $d\mu$ is positive before μ reaches its maximum, and negative afterwards. Null $d\mu$ indicates that the system total Jacobian matrix is singular. This is clearly shown in section 4.5.

4.5 Linearization of Power System DAE

When the parameter in (4.1) is varied, the corresponding state vector X and the eigenvalues of the system matrix evaluated on this path change accordingly.

Linearization of (4.1) at the equilibrium point with specified U and Z as natural parameters leads to:

$$\begin{bmatrix} \Delta \dot{X} \\ 0 \end{bmatrix} = \begin{bmatrix} F_X & F_Y \\ G_X & G_Y \end{bmatrix} \begin{bmatrix} \Delta X \\ \Delta Y \end{bmatrix} = J_{total} \begin{bmatrix} \Delta X \\ \Delta Y \end{bmatrix} \quad (4.17)$$

Matrices F_X , F_Y , G_X , and G_Y contain first derivatives of F and G with respect to X and Y , evaluated at the equilibrium point.

Note that matrix G_Y is an algebraic Jacobian matrix that contains the power flow Jacobian matrix.

In the above equation, if $\det(G_Y)$ does not equal zero.

$$\Delta Y = -G_Y^{-1} G_X \Delta X \quad (4.18)$$

Substituting in (4.17) results in

$$\Delta \dot{X} = A_{sys} \Delta X \quad (4.19)$$

$$A_{sys} = F_X - F_Y G_Y^{-1} G_X \quad (4.20)$$

The essential small-disturbance dynamic characteristics of a structure-preserving model are expressed in terms of eigen-properties of the reduced system matrix A_{sys} . This matrix is called dynamic system state matrix.

Eigenvalue analysis of A_{sys} will give dynamic stability information of the current equilibrium point under small disturbances. At voltage collapse, the system loses the ability to supply enough power to a heavily loaded network. At that point, the so called saddle node bifurcation occurs, which is described by the movement of one eigenvalue of A_{sys} on the real axis, crossing the origin from the left half of the complex plane. Eigenvalue computation can detect this movement. Participation factor studies will show how bus voltages participate in

this collapse mode, and sensitivity analysis will show the parameter influence on this critical situation. However, the above procedure is computational intensive since eigenvalue computation is involved. Furthermore, the formulation of A_{sys} also destroys the sparsity of J_{total} .

At saddle node bifurcation that leads to voltage collapse, one of the eigenvalue of A_{sys} becomes zero. Equivalently, the determinant of A_{sys} equals zero. From matrix theory, we know that,

$$\begin{aligned} \det J_{total} &= \det \begin{bmatrix} F_X & F_Y \\ G_X & G_Y \end{bmatrix} = \det(F_X - F_Y G_Y^{-1} G_X) \det(G_Y) \\ &= \det(A_{ns}) \det(G_Y) \\ \det J_{total} &= \det \begin{bmatrix} F_X & F_Y \\ G_X & G_Y \end{bmatrix} = \det(F_X - F_Y G_Y^{-1} G_X) \det(G_Y) \\ &= \det(A_{ns}) \det(G_Y) \end{aligned} \quad (4.21)$$

If G_Y is nonsingular, the determinant of A_{sys} becomes zero if and only if the determinant of J_{total} is zero. This is the Schur formula. J_{total} is very sparse and thus allows efficient handling using sparse techniques. Therefore, detection of the singularity of A_{ns} is equivalent to the detection of the singularity of J_{total} .

4.6 Detection of Saddle Node and Hopf Bifurcation with System Total Jacobian Matrix

Proposition 4.1: *When G_Y^{-1} exists and $u_X \neq 0$, there is the following equivalent condition*

$$A_{ns} u_X = \lambda u_X \quad (4.22)$$

$$\text{if and only if } \begin{bmatrix} F_X - \lambda I & F_Y \\ G_X & G_Y \end{bmatrix} \begin{bmatrix} u_X \\ u_Y \end{bmatrix} = 0, \quad (4.23)$$

$$\text{where } u_Y = -G_Y^{-1}G_X u_X \quad (4.24)$$

We define the extended right eigenvector $u = \begin{bmatrix} u_X^T & u_Y^T \end{bmatrix}^T$.

=

Proof[11]:

$$\text{Assume } A_{ns} u_X = \lambda u_X \text{ ie. } (F_X - F_Y G_Y^{-1} G_X) u_X = \lambda u_X. \quad (4.25)$$

From L.H.S of (4.23)

$$\begin{bmatrix} F_X - \lambda I & F_Y \\ G_X & G_Y \end{bmatrix} \begin{bmatrix} u_X \\ u_Y \end{bmatrix} = \begin{bmatrix} (F_X - \lambda I) u_X + F_Y u_Y \\ G_X u_X + G_Y u_Y \end{bmatrix} = \begin{bmatrix} (F_X - \lambda I) u_X - F_Y G_Y^{-1} G_X u_X \\ G_X u_X - G_Y G_Y^{-1} G_X u_X \end{bmatrix} = \begin{bmatrix} (F_X - F_Y G_Y^{-1} G_X) u_X - \lambda u_X \\ 0 \end{bmatrix} = 0 \quad (4.26)$$

(Substitution of $u_Y = -G_Y^{-1}G_X u_X$ in the above equation verifies (4.23)). Or

$$\text{Assume } \begin{bmatrix} F_X - \lambda I & F_Y \\ G_X & G_Y \end{bmatrix} \begin{bmatrix} u_X \\ u_Y \end{bmatrix} = 0 \quad (4.27)$$

$$\text{That is } \begin{bmatrix} (F_X - \lambda I) u_X + F_Y u_Y \\ G_X u_X + G_Y u_Y \end{bmatrix} = 0 \quad (4.28)$$

substitute $u_Y = -G_Y^{-1}G_X u_X$ into (4.28),

After rearrangement. based on the definition of A_{ns}

$$A_{ns} u_X = \lambda u_X \quad (4.29)$$

is obtained.

=

This concludes the proof for Proposition 4.1.

(4.23) will be utilized to detect either Saddle node or Hopf bifurcation

4.6.1 Detection of Saddle Node Bifurcation

For the detection of Saddle node bifurcations,

$$A_{u,u} u_X = 0 \times u_X = 0 \quad (4.30)$$

From proposition 4.1, the condition

$$\begin{bmatrix} F_X & F_Y \\ G_X & G_Y \end{bmatrix} \begin{bmatrix} u_X \\ u_Y \end{bmatrix} = 0 \quad (4.31)$$

will be utilized to detect Saddle node bifurcation. That is, to detect the singularity of the total Jacobian matrix

$$\text{We define } A_{total} = \begin{bmatrix} F_X & F_Y \\ G_X & G_Y \end{bmatrix}.$$

The singularity of A_{total} can be detected when $d\mu=0$, calculated from the predictor

(4.15). When $d\mu=0$, (4.15) becomes

$$\begin{bmatrix} F_X & F_Y & F_u \\ G_X & G_Y & G_u \\ & e_k^T & 0 \end{bmatrix} \begin{bmatrix} dX \\ dY \\ 0 \end{bmatrix} = \begin{bmatrix} 0 \\ 0 \\ \pm 1 \end{bmatrix} \quad (4.32)$$

$$\text{Which implies } \begin{bmatrix} F_X & F_Y \\ G_X & G_Y \end{bmatrix} \begin{bmatrix} dX \\ dY \end{bmatrix} = 0 \quad (4.33)$$

And

$$\begin{bmatrix} e_k^T \\ & & 0 \end{bmatrix} \begin{bmatrix} dX \\ dY \\ 0 \end{bmatrix} = \begin{bmatrix} 0 \\ 0 \\ \pm 1 \end{bmatrix} \quad (4.34)$$

$\therefore \begin{bmatrix} dX \\ dY \end{bmatrix}$ is not a null vector.

Thus the saddle node bifurcation point can be readily identified by equivalently detecting null $d\mu$ during the direct equilibrium tracing, without formation of A_{sys} and computing its eigenvalues.

4.6.2 Detection of Hopf Bifurcation without Eigenvalue Calculation

After a simple transformation, Hopf bifurcation corresponds to a fold point of the transformed manifold.

Proposition 4.2: *Let the maximum eigenvalue of*

$$(A_{total} + A_{total}^f) = \begin{bmatrix} F_X + F_X^f & F_Y + G_Y^f \\ G_X + F_Y^f & G_Y + G_Y^f \end{bmatrix} \text{ is } \lambda_1, \text{ then case 1: } \lambda_1 \geq 0 \text{ is the necessary condition for}$$

Hopf bifurcation associated with the power system DAE model (A_{sys}). Case 2: When A_{total} is approximate to a normal matrix (this is the most likely case), $\lambda_1 = 0$ becomes the necessary condition.

Proof:

Case 1: Provides the proof for the necessary condition of Hopf bifurcation.

At Hopf bifurcation, there exists an eigenvalue of A_{sys} , $\lambda = j\omega$ such that, from proposition 4.1.

$$(A_{total} - j\omega \begin{bmatrix} I & \\ & 0 \end{bmatrix})u = \begin{bmatrix} F_X - j\omega & F_Y \\ G_X & G_Y \end{bmatrix}u = 0 \quad (4.35)$$

and assume u is an associated eigenvector with 2-norm unity. Then

$$((A_{total} - j\omega \begin{bmatrix} I & \\ & 0 \end{bmatrix})u, u) = u^H (A_{total} - j\omega \begin{bmatrix} I & \\ & 0 \end{bmatrix})u = 0 \quad (4.36)$$

and.

$$u^H (A_{total} - j\omega \begin{bmatrix} I & \\ & 0 \end{bmatrix})^H u = ((A_{total}^T + j\omega \begin{bmatrix} I & \\ & 0 \end{bmatrix})u, u) = 0 \quad (4.37)$$

Therefore $((A_{total} + A_{total}^T)u, u) = 0$. It is obtained from the summation of above two equations.

$$\text{Since } \lambda_i = \max((A_{total} + A_{total}^T)x, x) \text{ for } x \neq 0, x \in C. \quad (4.38)$$

$$\text{Therefore } \lambda_i \geq ((A_{total} + A_{total}^T)u, u) = 0 \quad (4.39)$$

Case 2: Provides the proof for necessary condition for the Hopf bifurcation when A_{total} is a normal matrix.

From Hausdorff's convex hull theorem [48].

$$((A_{total} + A_{total}^T)u, u) = \sum_{i=1}^{M+N} \beta_i \lambda_i = 0 \quad (4.40)$$

with $0 \leq \beta_i \leq 1$ and $\sum_{i=1}^{M+N} \beta_i = 1$. where M is the dimension of dynamic variables and

N is the dimension of the algebraic variables.

For normal operation of the power system. $\lambda_i \leq 0$ where λ_i is the eigenvalue of A_{total} .

Therefore $\lambda_i = 0$ indicates the Hopf bifurcation.

—

Then the identification of Hopf bifurcation for A_{total} is nothing but the identification of the singularity of the matrix $(A_{total} + A_{total}^T)$. A set of cut functions for Hopf related fold bifurcation could be implicitly defined as $\gamma_{H1}(X, Y, \mu, \alpha)$ and $\gamma_{H2}(X, Y, \mu, \alpha)$ in the following equation.

$$\begin{bmatrix} F_X + F_X^T & F_Y + G_Y^T & e_x & e_y \\ G_X + F_Y^T & G_Y + G_Y^T & 0 & 0 \\ e_x^T & 0 & 0 & 0 \\ e_y^T & 0 & 0 & 0 \end{bmatrix} \begin{bmatrix} u_X \\ u_Y \\ \gamma_{H1} \\ \gamma_{H2} \end{bmatrix} + \begin{bmatrix} 0 \\ 0 \\ 1 \\ 0 \end{bmatrix} = 0 \quad (4.41)$$

where $k \neq j$ or equivalently,

$$\begin{bmatrix} F_X + F_X^T & F_Y + G_Y^T & e_x & e_y \\ G_X + F_Y^T & G_Y + G_Y^T & 0 & 0 \\ e_x^T & 0 & 0 & 0 \\ e_y^T & 0 & 0 & 0 \end{bmatrix} \begin{bmatrix} v_X \\ v_Y \\ \gamma_{H1} \\ \gamma_{H2} \end{bmatrix} + \begin{bmatrix} 0 \\ 0 \\ 1 \\ 0 \end{bmatrix} = 0 \quad (4.42)$$

u_X and u_Y (v_X and v_Y) are the vectors associated with the index γ_{H1} and γ_{H2} . They correspond, respectively, to X and Y variables.

The test matrix $(A_{total} + A_{total}^T)$ is 2 dimensional singular if and only if

$$\gamma_{H1}(X, Y, \mu, \alpha) = 0 \text{ and } \gamma_{H2}(X, Y, \mu, \alpha) = 0.$$

Since $\gamma_{H1}(X, Y, \mu, \alpha) = 0$ and $\gamma_{H2}(X, Y, \mu, \alpha) = 0$, therefore

$$(A_{total} + A_{total}^T) \begin{bmatrix} u_X \\ u_Y \end{bmatrix} = 0. \quad (4.43)$$

$$\text{Since } e_x^T \begin{bmatrix} u_X \\ u_Y \end{bmatrix} + 1 = 0, \quad \left\| \begin{bmatrix} u_X \\ u_Y \end{bmatrix} \right\| \neq 0 \quad (4.44)$$

Therefore $(A_{total} + A_{total}^T)$ is singular.

Note that as a special case, Saddle node bifurcation could also cause $(A_{total} + A_{total}^T)$ singular. Therefore this test needs to work with a Saddle node bifurcation test to identify Hopf bifurcation.

At the Hopf bifurcation, the cut set condition is satisfied, that is $\gamma_{H1}(X, Y, \mu, \alpha) = 0$, and $\gamma_{H2}(X, Y, \mu, \alpha) = 0$ but $d\mu \neq 0$.

At each continuation step, γ_{SNB} and γ_{H1}, γ_{H2} are checked.

If γ_{SNB} changes sign, the Saddle node bifurcation point has just been passed.

Otherwise, if γ_{H1}, γ_{H2} changes sign, the Hopf bifurcation has just been passed.

Therefore, without eigenvalue calculation, Hopf bifurcation could be detected along with Saddle node bifurcation using properly defined cut functions. Fig. 4-1 presents the flowchart of the process of the detection of SNB and Hopf bifurcations along the PV curve tracing.

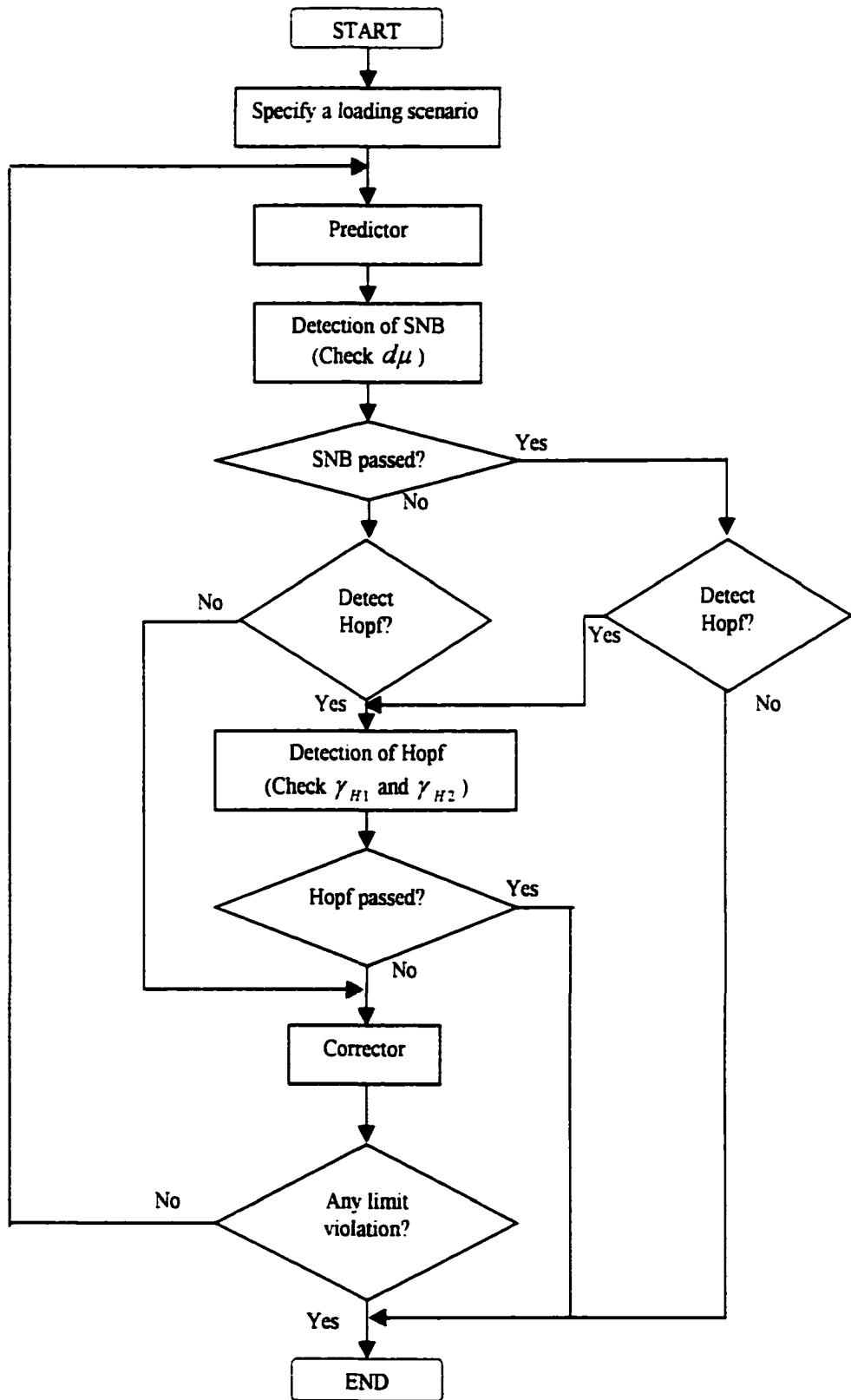


Figure 4-1: Flowchart for detection of Saddle node and Hopf bifurcations

4.7 Numerical Example

Detection of Saddle node and Hopf bifurcations in power system equilibrium tracing is demonstrated through the numerical tests performed on the New-England-39-bus system.

The following conditions are assumed throughout the simulation.

- Constant power load model;
- The maximum real power limit, the field current and the armature current limits are considered for each generator;
- No generator is allowed to have terminal voltage higher than 1.1 p.u. when its secondary voltage control is utilized to increase system stability margin;
- The loading scenario is defined as that all the loads are increased with constant power factor, and all the generators participate in the load pick-up at the same rate.

The starting condition for power system equilibrium tracing is the base case power flow of the New England system. The one line diagram and data files of the New England system are presented in the appendix.

4.7.1 Equilibrium Tracing with Detection of SNB and Hopf

The PV curve is traced under the base control configuration. The Hopf bifurcation index is checked at each continuation step. The eigenvalue calculation is avoided by detecting the simultaneous sign change of γ_{H1} and γ_{H2} . Fig. 4-1 shows the PV curve under base case control condition. The system load margin constrained by Hopf is 809 MW and it is 1370 MW away from voltage collapse.

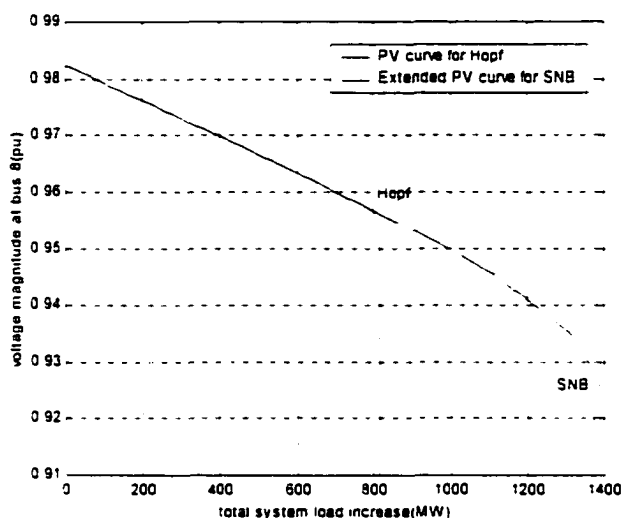


Figure 4-2: Hopf detection in PV curve tracing under base control

4.7.2 Computational Requirements Compared with Eigenvalue Calculation

The detection methods proposed in this chapter are computationally efficient since the eigenvalue calculations are avoided. From the formulation (4.32) for Saddle node bifurcation and formulation (4.41) or (4.42) for Hopf bifurcation, we can see that the augmented linear equations are solved only once at each continuation step. This method saves a large amount of computation compared to eigenvalue calculation since the eigenvalue calculation employs intensive iterative calculation. This is the case even in some simplified algorithm solving for only the largest real part eigenvalue.

4.8 Summary

The load margin of a power system could be determined by equilibrium tracing. Because it is based on a more exact modeling of a power system, the solution is more reliable than solution based on continuation power flow. Meanwhile, the generator related dynamic could be detected, along with Saddle node bifurcation, with a system total Jacobian matrix. A

new method is proposed for the quickest detection of Hopf bifurcation. This formulation is a fundamental step towards unified margin boundary tracing presented in chapter 5. and optimal margin boundary tracing explained in chapter 6.

CHAPTER 5 UNIFIED MARGIN BOUNDARY TRACING

5.1 Introduction

In chapter 4, we identified both Saddle node and Hopf bifurcation for a fixed set of control parameters. When control parameters change, the stability margin related to Saddle node or Hopf bifurcation changes as well. The voltage stability margin boundary is confined by Saddle node bifurcations, whereas oscillatory stability margin boundary is confined by Hopf bifurcations associated with different sets of control parameters. From the perspective of bifurcation, this chapter provides a unified framework to identify and trace voltage as well as oscillatory stability margin boundaries. The system load margin corresponding to any control configuration is determined without retracing the entire PV curve. The eigenvalue calculation associated with the Hopf bifurcation is avoided. The proposed method considers all the system limits.

5.2 Natural Parameterization of Control Parameter Space for Margin Boundary Tracing

In chapter four, the equilibrium manifold of power system (4.1) is actually parameterized by both control parameters and load parameters. But only load parameters are considered for power system equilibrium tracing. However the control parameters should be taken into account for margin boundary tracing. Then there is a natural splitting in parameter space. This parameter space is the combination of control parameters U and the load parameters Z :

Parameter space = control parameter space \oplus load parameter space

Control parameter space can contain any type of control. The following controls are studied in this chapter:

- Load shedding
- Shunt capacitance
- Shunt reactive power compensation
- Generator secondary voltage control

Control parameter space is parameterized by a scalar α to characterize this space.

$$U_i = U_{i0} + \alpha KC_i \quad (5.1)$$

Where U_{i0} indicates the initial configuration of control i .

Different combinations of control action can be achieved by assigning different ratio values to KC_i .

This parameterization leads to two parameter variations: μ characterizing system loading condition with respect to a specified loading scenario and α characterizing control parameter with respect to a specified control scenario. The equations of power system equilibrium manifold are modified to reflect these changes as shown in (5.2).

$$\begin{cases} 0 = F(X, Y, \mu, \alpha) \\ 0 = G(X, Y, \mu, \alpha) \end{cases} \quad (5.2)$$

Note that the loading scenario is kept invariant during the change of control scenario in the margin boundary tracing of chapter 5 and optimization of control scenario in the optimal margin boundary tracing of chapter 6.

5.3 Formulation of Unified Margin Boundary Tracing

5.3.1 Margin Boundary Manifold of Power System

In the case of a multi-dimensional, implicitly defined manifold M , specific local parameterization needs to be constructed to trace a certain submanifold with a special property on M . Saddle node or Hopf bifurcation points form a margin boundary submanifold corresponding to the change of control parameters along a specified control scenario. Therefore bifurcation related stability margin boundary manifold could be traced by augmenting the power system equilibrium with a characterization equation. This characterization equation defines the margin boundary.

5.3.2 Bifurcation Characterization

5.3.2.1 Characterization of Saddle node bifurcation

The Saddle node bifurcation of a dynamic system corresponds to codimension 1 fold bifurcation. A cut function for Saddle node related fold bifurcation is implicitly defined as $\gamma_{SNB}(x)$ in the following equation.

$$\begin{bmatrix} F_V & F_Y & e_k \\ G_V & G_Y & 0 \\ e_l^T & 0 & \gamma_{SNB} \end{bmatrix} \begin{bmatrix} u_X^0 \\ u_Y^0 \\ \gamma_{SNB} \end{bmatrix} + \begin{bmatrix} 0 \\ 0 \\ 1 \end{bmatrix} = 0 \quad (5.3)$$

where we denote $u^0 = \begin{bmatrix} u_X^0 \\ u_Y^0 \end{bmatrix}$

$$\text{or equivalently, } \begin{bmatrix} F_V & F_Y & e_k \\ G_V & G_Y & 0 \\ e_l^T & 0 & \gamma_{SNB} \end{bmatrix}^T \begin{bmatrix} v_X^0 \\ v_Y^0 \\ \gamma_{SNB} \end{bmatrix} + \begin{bmatrix} 0 \\ 0 \\ 1 \end{bmatrix} = 0 \quad (5.4)$$

where we denote $v^0 = \begin{bmatrix} v_X^0 \\ v_Y^0 \end{bmatrix}$.

With the formulation of (5.3), the cut set condition $\gamma_{SNB}(X, Y, \mu, \alpha) = 0$ implies it is at the fold point.

If $\gamma_{SNB}(X, Y, \mu, \alpha) = 0$, then

$$\begin{bmatrix} F_X & F_Y \\ G_X & G_Y \end{bmatrix} \begin{bmatrix} u_X^0 \\ u_Y^0 \end{bmatrix} = 0 \text{ and } e_i^T \begin{bmatrix} u_X^0 \\ u_Y^0 \end{bmatrix} = 1 \text{ which implies } \begin{bmatrix} u_X^0 \\ u_Y^0 \end{bmatrix} \neq 0$$

Hence, proving that it is at the fold point.

$\begin{bmatrix} u_X^0 \\ u_Y^0 \end{bmatrix}$ is the right eigenvector associated with zero eigenvalue. Similarly $\begin{bmatrix} v_X^0 \\ v_Y^0 \end{bmatrix}$ is the

left eigenvector associated with zero eigenvalue.

In principle, the indices k and j in (5.3-5.4) may be kept fixed throughout the computation, but it is usually advantageous to update them occasionally by selecting new indices for the next step according to

$$|(e^k)^T v^0| = \max\{|(e^i)^T v^0|, i = 1, \dots, m\} \quad (5.5)$$

$$|(e^j)^T u^0| = \max\{|(e^i)^T u^0|, i = 1, \dots, m\} \quad (5.6)$$

5.3.2.2 Characterization of Hopf bifurcation

At the Hopf bifurcation, the cut set condition is satisfied, that is $\gamma_{H_1}(X, Y, \mu, \alpha) = 0$, and $\gamma_{H_2}(X, Y, \mu, \alpha) = 0$. Any of them alone could be used to identify Hopf bifurcation in Hopf bifurcation related margin boundary tracing.

For a Hopf bifurcation, any of $\gamma_{H_1}(X, Y, \mu, \alpha) = 0$ and $\gamma_{H_2}(X, Y, \mu, \alpha) = 0$ could be differentiated to trace Hopf bifurcation related margin boundary (Excluding the possibility of Saddle node bifurcation).

5.3.2.3 Augmentation for bifurcation characterization

A characterization of bifurcation can be formulated in the cut set form as follows on the solution manifold [17].

$$B(X, Y, \mu, \alpha) = \begin{bmatrix} F(X, Y, \mu, \alpha) \\ G(X, Y, \mu, \alpha) \\ c(X, Y, \mu, \alpha) \end{bmatrix} = 0 \quad (5.7)$$

These bifurcation based margin boundary tracing can be obtained by the solution manifold as defined in (5.7)[40].

A cut function for Saddle node bifurcation could be substituted to trace voltage stability margin boundary.

$$c(X, Y, \mu, \alpha) = \gamma_{SNB}(X, Y, \mu, \alpha) \quad (5.8)$$

$$Dc(X, Y, \mu, \alpha) = D\gamma_{SNB} \quad (5.9)$$

(Here D stands for differentiation)

A cut function for Hopf bifurcation is substituted to trace oscillatory stability margin boundary.

$$c(X, Y, \mu, \alpha) = \gamma_{H1}(X, Y, \mu, \alpha) \quad (5.10)$$

$$Dc(X, Y, \mu, \alpha) = D\gamma_{H1} \quad (5.11)$$

5.3.3 Augmentation for Local Parameterization

The total augmented equations for margin boundary tracing are

$$H(X, Y, \mu, \alpha) = \begin{bmatrix} B(X, Y, \mu, \alpha) \\ [X^T \ Y^T \ \mu \ \alpha] p_k - \eta \end{bmatrix} = \begin{bmatrix} F(X, Y, \mu, \alpha) \\ G(X, Y, \mu, \alpha) \\ c(X, Y, \mu, \alpha) \\ [X^T \ Y^T \ \mu \ \alpha] p_k - \eta \end{bmatrix} = 0 \quad (5.12)$$

$$DH(X, Y, \mu, \alpha) = \begin{bmatrix} DF \\ DG \\ Dc \\ e_k^T \end{bmatrix} = \begin{bmatrix} F_x & F_y & F_\mu & F_\alpha \\ G_x & G_y & G_\mu & G_\alpha \\ c_x & c_y & c_\mu & c_\alpha \\ e_k \end{bmatrix} \quad (5.13)$$

where $\eta = [X_{pre}^T \ Y_{pre}^T \ \mu_{pre} \ \alpha_{pre}] p_k$ and it is obtained from the tangent vector

calculated in boundary predictor.

5.3.3.1 Boundary predictor

With σ as step size.

$$DH(X, Y, \mu, \alpha) \begin{bmatrix} dX \\ dY \\ d\mu \\ d\alpha \end{bmatrix} = \begin{bmatrix} 0 \\ 0 \\ 0 \\ \pm 1 \end{bmatrix} \quad \text{and} \quad \begin{bmatrix} X_{pre} \\ Y_{pre} \\ \mu_{pre} \\ \alpha_{pre} \end{bmatrix} = \begin{bmatrix} X \\ Y \\ \mu \\ \alpha \end{bmatrix} + \sigma \begin{bmatrix} dX \\ dY \\ d\mu \\ d\alpha \end{bmatrix} \quad (5.14)$$

The Jacobian matrix of the augmented equation system is nonsingular under the appropriate choice of a continuation parameter. Similar criteria can be applied as is presented in [4].

5.3.3.2 Boundary corrector

The Newton method is employed to do the boundary correction as

$$\begin{bmatrix} X \\ Y \\ \mu \\ \alpha \end{bmatrix}^{\text{new}} = \begin{bmatrix} X \\ Y \\ \mu \\ \alpha \end{bmatrix} - DH^{-1}(X, Y, \mu, \alpha)H(X, Y, \mu, \alpha) \quad (5.15)$$

5.3.4 Differentiation of Cut Functions

Through the differentiation of the above augmented equations, the derivative of the augmenting function γ_{SNB} could be obtained from

$$D\gamma_{SNB} w = v^{0T} D \begin{bmatrix} F_X & F_Y \\ G_X & G_Y \end{bmatrix} (u^0, w) \quad (5.16)$$

$$\text{where } w = \begin{bmatrix} dX \\ dY \\ d\mu \\ d\alpha \end{bmatrix}$$

Proof:

To obtain the derivative of γ_{SNB} ,

$$\begin{bmatrix} v_X^{0T} & v_Y^{0T} & \gamma_{SNB} \end{bmatrix} \begin{bmatrix} F_X & F_Y & e_t \\ G_X & G_Y & 0 \\ e_f & 0 & \gamma_{SNB} \end{bmatrix} \begin{bmatrix} u_X^0 \\ u_Y^0 \\ \gamma_{SNB} \end{bmatrix} = \begin{bmatrix} v_X^{0T} & v_Y^{0T} & \gamma_{SNB} \end{bmatrix} \begin{bmatrix} 0 \\ 0 \\ -1 \end{bmatrix} = -\gamma_{SNB} \quad (5.17)$$

$$\begin{bmatrix} v_X^{0T} & v_Y^{0T} \end{bmatrix} \begin{bmatrix} F_X & F_Y \\ G_X & G_Y \end{bmatrix} \begin{bmatrix} u_X^0 \\ u_Y^0 \end{bmatrix} + \begin{bmatrix} v_X^{0T} & v_Y^{0T} \end{bmatrix}^T e_k \gamma_{SNB} + e_l^T \begin{bmatrix} u_X^0 \\ u_Y^0 \end{bmatrix} \gamma_{SNB} = -\gamma_{SNB} \quad (5.18)$$

Since $\begin{bmatrix} v_X^{0T} & v_Y^{0T} \end{bmatrix}^T e_k = -1$ is derived from (5.4) and $e_l^T \begin{bmatrix} u_X^0 \\ u_Y^0 \end{bmatrix} = -1$ is derived from

(5.3),

$$\gamma_{SNB} = \begin{bmatrix} v_X^{0T} & v_Y^{0T} \end{bmatrix} \begin{bmatrix} F_X & F_Y \\ G_X & G_Y \end{bmatrix} \begin{bmatrix} u_X^0 \\ u_Y^0 \end{bmatrix} \quad (5.19)$$

$$D\gamma_{SNB} = \begin{bmatrix} u_X^{0T} & u_Y^{0T} \end{bmatrix}^T \begin{bmatrix} F_X & F_Y \\ G_X & G_Y \end{bmatrix}^T D \begin{bmatrix} v_X^0 \\ v_Y^0 \end{bmatrix} + \begin{bmatrix} v_X^{0T} & v_Y^{0T} \end{bmatrix} \begin{bmatrix} F_X & F_Y \\ G_X & G_Y \end{bmatrix} D \begin{bmatrix} u_X^0 \\ u_Y^0 \end{bmatrix} + \begin{bmatrix} v_X^{0T} & v_Y^{0T} \end{bmatrix} D \begin{bmatrix} F_X & F_Y \\ G_X & G_Y \end{bmatrix} \begin{bmatrix} u_X^0 \\ u_Y^0 \end{bmatrix} \quad (5.20)$$

$$D\gamma_{SNB} = \begin{bmatrix} v_X^{0T} & v_Y^{0T} \end{bmatrix} D \begin{bmatrix} F_X & F_Y \\ G_X & G_Y \end{bmatrix} \begin{bmatrix} u_X^0 \\ u_Y^0 \end{bmatrix} \quad (5.21)$$

To avoid the calculation of the Hessian matrix, in implementation, finite differentiation could be applied instead, as follows.

$$D\gamma_{SNB} \approx \frac{1}{\delta} v_{(X,Y,\mu,\alpha)}^{0T} \left[T_{(X-\delta u_X^0, Y+\delta u_Y^0, \mu, \alpha)} - T_{(X,Y,\mu,\alpha)} \right] \quad (5.22)$$

Where $\delta \neq 0$ is a sufficiently small scalar. The test matrix for SNB is defined as

$$T = \begin{bmatrix} DF \\ DG \end{bmatrix}$$

Actually, Jacobian matrices are evaluated twice, at points $(Y + \delta u_Y^0, Y + \delta u_Y^0, \mu, \alpha)$ and (Y, Y, μ, α) to approximate $D\gamma_{SNB}$.

Through the differentiation of the above augmented equations, the derivative of the augmenting function γ could be obtained from

$$D\gamma_{HI}w = v^{0T} D \begin{bmatrix} F_X + F_X^T & F_Y + G_X^T \\ G_X + F_Y^T & G_Y + G_Y^T \end{bmatrix} (u^0, w) \quad (5.23)$$

The proof is similar to the proof of proposition 5.1 and thus is omitted here.

Therefore, without eigenvalue calculation, Hopf bifurcation could be detected and directed, just as when we trace for Saddle node bifurcation by bifurcation unfolding with cut function. The volume of calculation is decreased dramatically.

In implementation, finite differentiation is also applied as follows.

$$D\gamma_{HI} \approx \frac{1}{\delta} v_{(X,Y,\mu,\alpha)}^{0T} \left[T_{(X-\delta u_Y^0, Y-\delta u_Y^0, \mu, \alpha)} - T_{(X,Y,\mu,\alpha)} \right] \quad (5.24)$$

Where the test matrix for Hopf bifurcation is defined as

$$T = \begin{bmatrix} DF \\ DG \end{bmatrix} + \begin{bmatrix} DF \\ DG \end{bmatrix}^T$$

5.3.5 Unified Margin Boundary Tracing

The unified margin boundary tracing program is designed to have several options as follows.

- 1) Saddle node bifurcation related voltage stability margin boundary tracing.
- 2) Hopf bifurcation related oscillatory stability margin boundary tracing.

3) The most conservative margin boundary tracing.

The first two options check either SNB or Hopf bifurcation condition correspondingly along the equilibrium tracing and further trace the related margin boundary. The most conservative margin boundary tracing checks both bifurcation conditions and always switches to and continues the tracing on the most conservative margin boundary.

The following steps are necessary in unified margin boundary tracing.

- 1) Specify a loading scenario.
- 2) Direct Equilibrium Tracing starts at the current operating point for the first boundary point under the current fixed control configuration and specified loading scenario.
- 3) Specify the control scenario that describes the change of control configuration or contingencies.
- 4) Boundary prediction with (5.14)
- 5) Boundary correction with (5.15)
- 6) Go to 4) unless some control variables hit limits. otherwise stop.

The procedure is also shown in flowchart Fig.5-1.

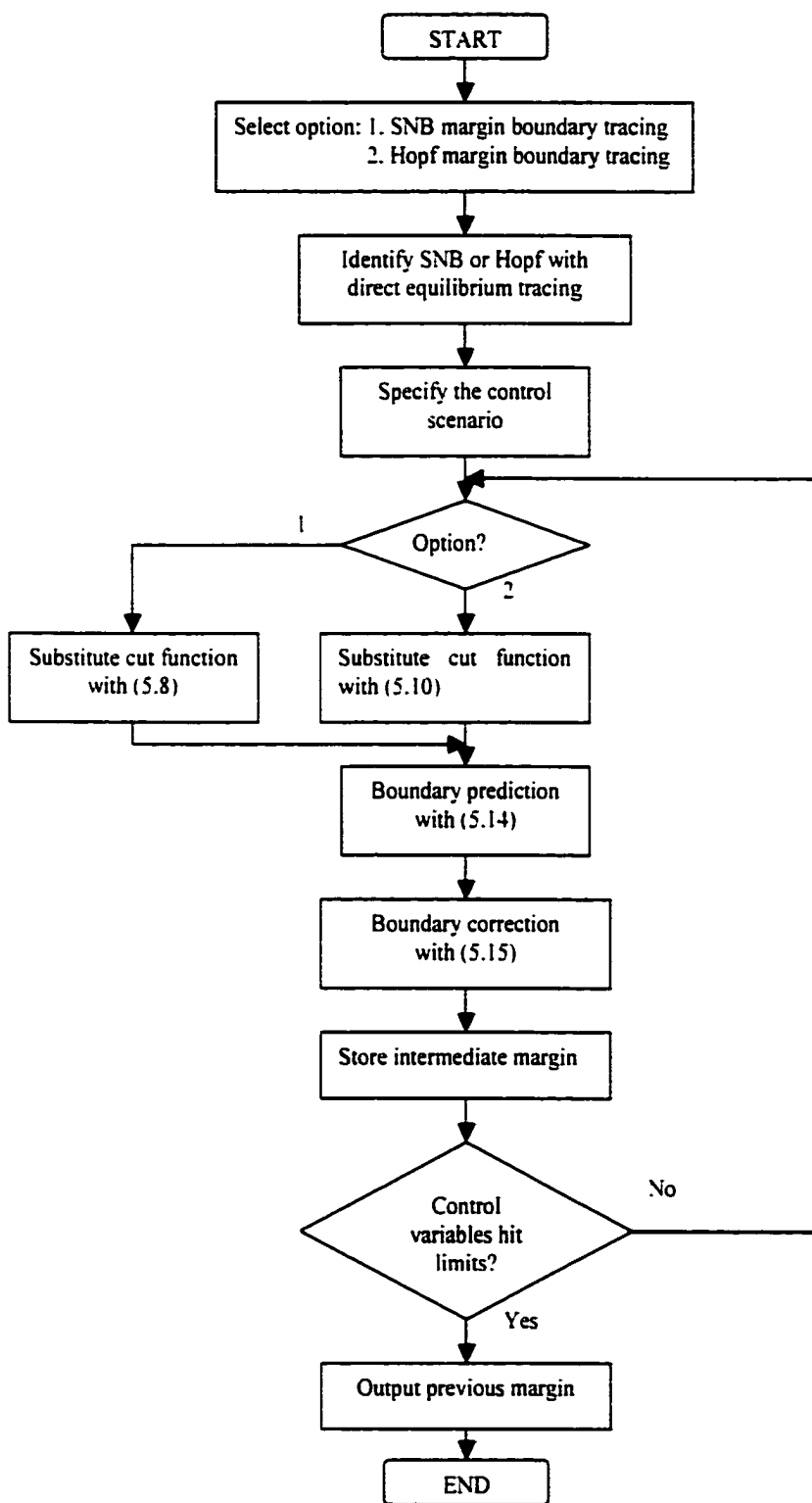


Figure 5-1: Flowchart of margin boundary tracing

5.4 Saddle Node Bifurcation Related Margin Boundary Tracing

Saddle node bifurcation related unified margin boundary tracing is demonstrated through the numerical tests performed on the New-England-39-bus system.

The same conditions are assumed as the numerical example of Chapter 4 except that the limit of V , of each generator is lower.

Before margin boundary is traced with respect to any control, direct equilibrium tracing is conducted under a specified load scenario from the base case operating point until Saddle node or Hopf bifurcation is located. The identification of Saddle node bifurcation and Hopf bifurcations along direct equilibrium tracing is presented in Chapter 4. In the numerical examples presented in this chapter, the loading scenario is defined as that all the loads are increased with constant power factor, and all the generators participate in the load pick-up at the same rate.

The starting condition for unified margin boundary tracing is first encountered Saddle node bifurcation point in power system equilibrium tracing, starting from the base case. Then the margin boundaries can be traced with respect to any specified control scenario.

5.4.1 Emergency Load Shedding

Fig.5-2 demonstrates the system total loading margin change with load shedding at bus 39. It is highly nonlinear and the system load margin reaches its maximum 1752.84 MW when 1056 MW load is shed. Further load shedding after that amount would decrease the loading margin.

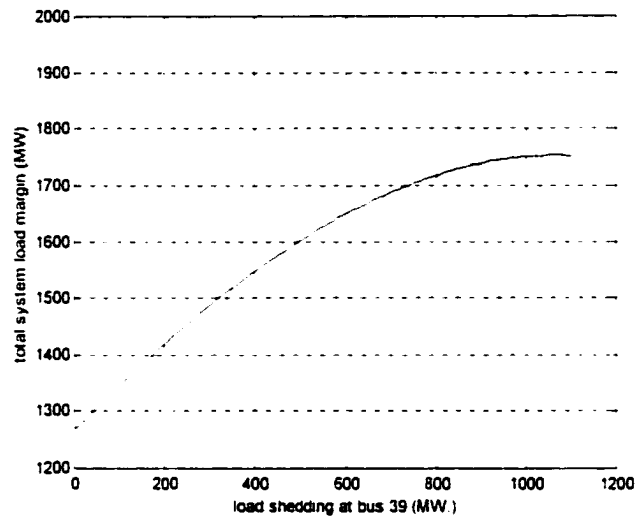


Figure 5-2: System load margin vs load shedding at bus 39

5.4.2 Reactive Power Support

Fig.5-3 shows the system loading margin change as shunt capacitance increases at bus 8. The sudden drop in margin at 3.0 p.u. shunt capacitance is caused when generator 30 hits its I_c and V_c limits.

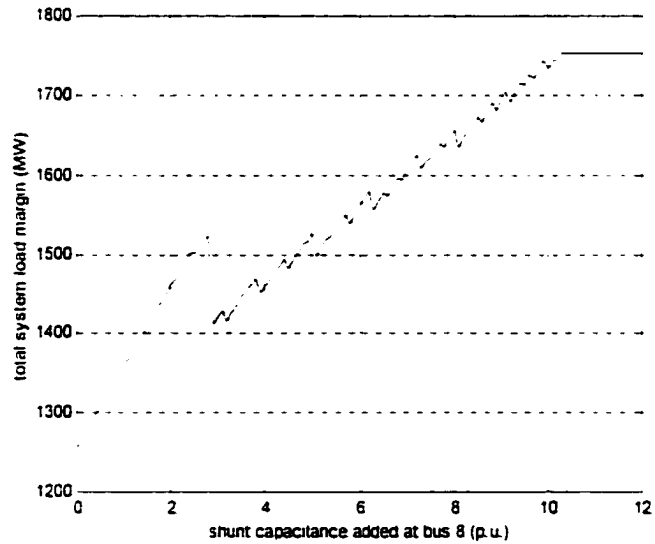


Figure5-3: System load margin vs shunt capacitance at bus 8

5.4.3 Secondary Voltage Control

Fig.5-4 shows the system margin change with respect to the increased reference voltage of the AVR of each generator. The sequential sharp “jumps” are due to some of the components hitting their limits.

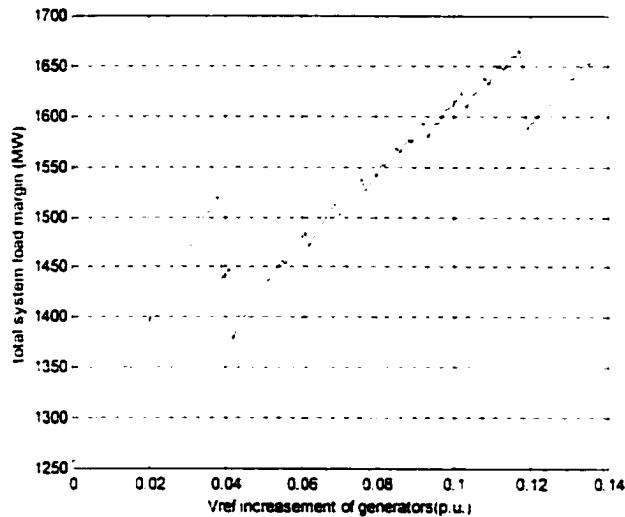


Figure 5-4: System load margin vs Vref adjustment at all generators

5.4.4 Control Combination

The control scenario could be any combination of control parameters. So a unified margin boundary tracing method can trace an actual margin boundary with respect to control parameter changes in any direction in the multi-control parameter space.

Fig. 5-5 shows how the load margin changes with respect to a control scenario: V_{ref} of generator 39 increases by 0.001 p.u in proportion to shunt capacitance at bus 8 increased by 0.1 p.u. and reactive power injection at bus 6 increased by 0.1 pu. The control scenario simulates the total effect of secondary voltage regulation, as well as linear and nonlinear reactive power compensations.

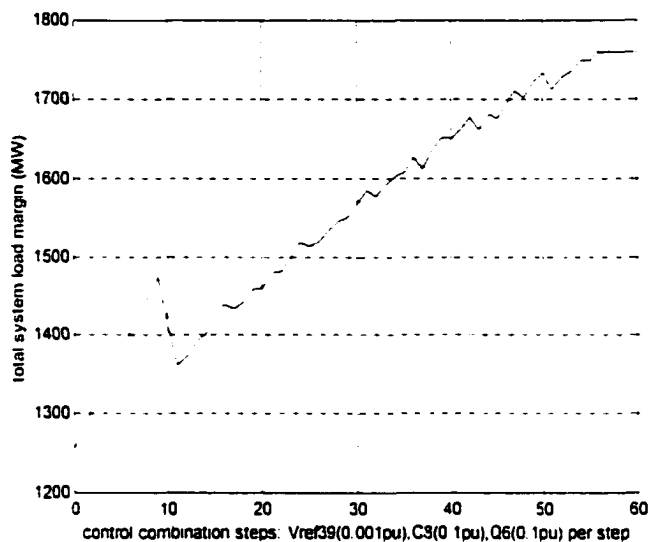


Figure 5-5: System load margin vs control combination steps:
Vref39(0.001pu),C3(0.1pu),Q6(0.1pu)

5.4.5 Multiple Contingencies

Voltage stability margin change due to single or multiple contingencies could also be traced by parameterizing the control parameter change involved in the contingency. The margin change caused by the double line outages of 8-9 and 7-8 is calculated by parameterization of branch outage. A multiplier of branch resistance and reactance is defined. If it is zero, the line is totally in. If it is 1, the line is totally out. A value between 0 and 1 indicates an intermediate status in the continuation process [Fig.5-6].

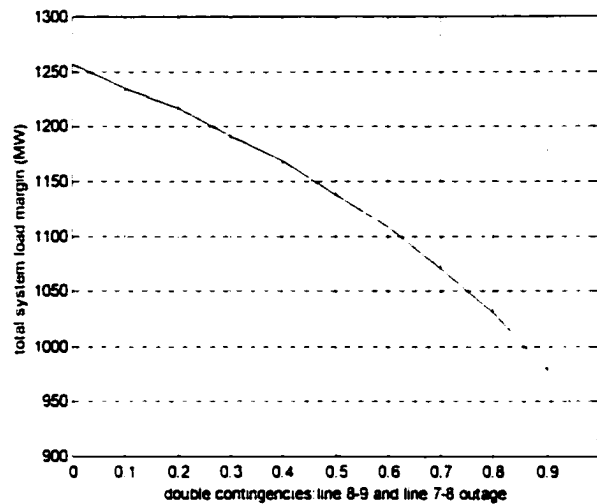


Figure 5-6: System load margin vs multiple contingencies: line 8-9 and line 7-8 outage

5.5 Saddle Node and Hopf Bifurcation Related Stability Boundary Tracing

In this section both Saddle Node and Hopf bifurcation margin boundaries are calculated for the New-England-39-bus system.

The same conditions are assumed as the numerical example of identification of both Saddle node and Hopf bifurcations in Chapter 4. The starting condition for the unified margin boundary tracing is Saddle node or Hopf bifurcation point in power system equilibrium tracing, starting from the base case.

5.5.1 Boundary Tracing with Respect to Generation Control Parameters

The Hopf bifurcation related margin boundaries could be traced with respect to any specified control scenario.

5.5.1.1 Load margin versus adjustment of K_a of AVR system

In Fig.5-7, voltage stability (SNB related) margin boundary versus adjustment of " K_a " gain of the AVR of each generator around its base case operating value is depicted as the solid curve. Oscillatory stability (Hopf bifurcation related) margin boundary versus adjustment of " K_a " around its base case operating value is depicted as the dashed curve. A positive value of K_a enhancement denotes an increase of K_a and a negative value denotes a decrease in K_a . Increase of K_a may lead to system oscillatory instability, even though the proximity to potential voltage collapse is enlarged. When K_a is decreased by more than 11, the system no longer loses stability via Hopf. Only Saddle node bifurcation related voltage collapse limits the system load margin. This confirms the theoretical condition for the AVR parameter effect on the evolution of Hopf bifurcation [32].

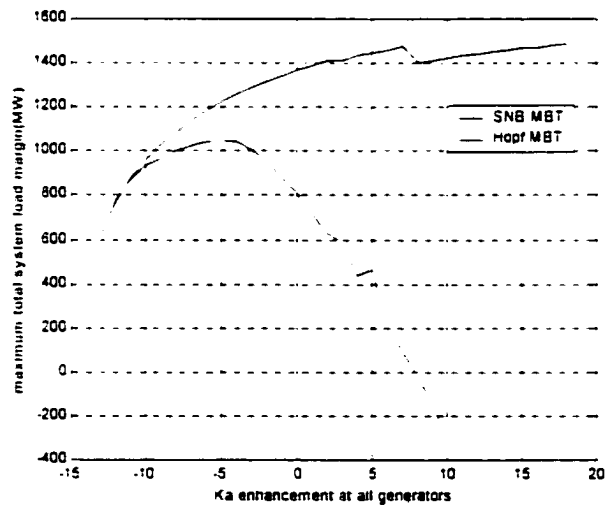


Figure 5-7: Unified margin boundary tracing versus K_a adjustment

5.5.1.2 Load margin versus adjustment of Vref of the AVR system

In Fig. 5-8, voltage stability (SNB related) margin boundary versus unified adjustment of Vrefs of all the generators around their base case operating value is depicted as the solid curve. Oscillatory stability (Hopf bifurcation related) margin boundary versus adjustment of Vref around its base case operating value is depicted as the dashed curve. An increase of Vref of AVR may lead to oscillatory instability even though the proximity to potential voltage collapse is enlarged. The non-smooth profile of margin boundary is due to various components hitting their limits.

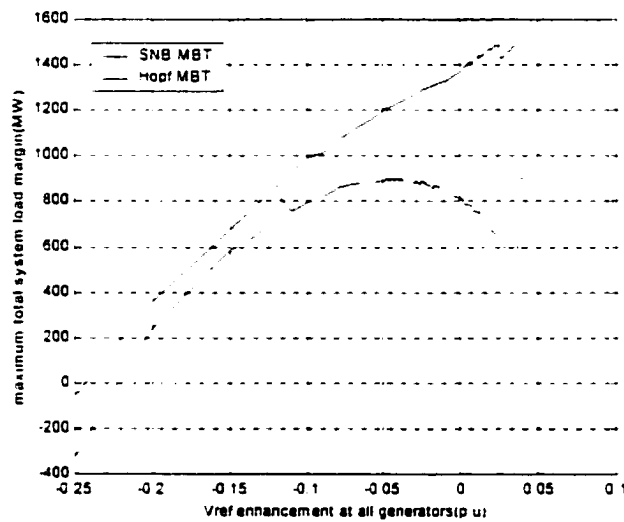


Figure 5-8: Unified margin boundary tracing versus Vref adjustment

5.5.2 Boundary Tracing with Respect to Network Parameter Change

5.5.2.1 Load shedding

Fig.5-9 shows that load shedding at bus 39 increases the load margin of both the Saddle node bifurcation related voltage collapse and Hopf bifurcation related oscillations.

Note that other control parameters such as K_a and V_{ref} are kept constant at their initial operating value. This demonstrates that load variation could also affect system oscillatory margin.

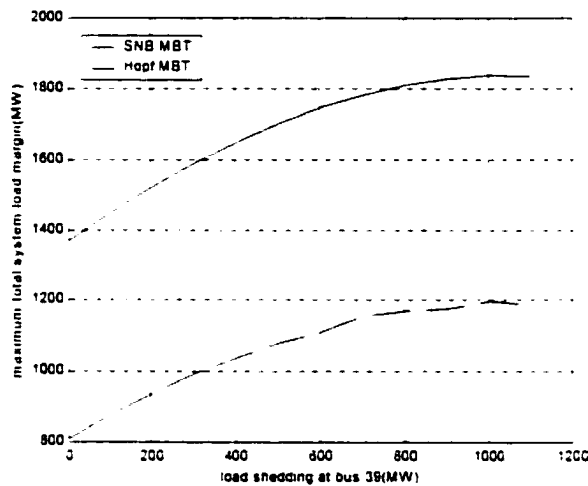


Figure 5-9: Unified margin boundary tracing versus load shedding

5.5.2.2 Contingency: single line outage

Fig.5-10 shows the margins that are constrained by the Saddle node and Hopf bifurcations. The margins declined due to the single line 6-31 outage. This line connects the load 6 to the generator at bus 31. This contingency represents a similar event described in [33].

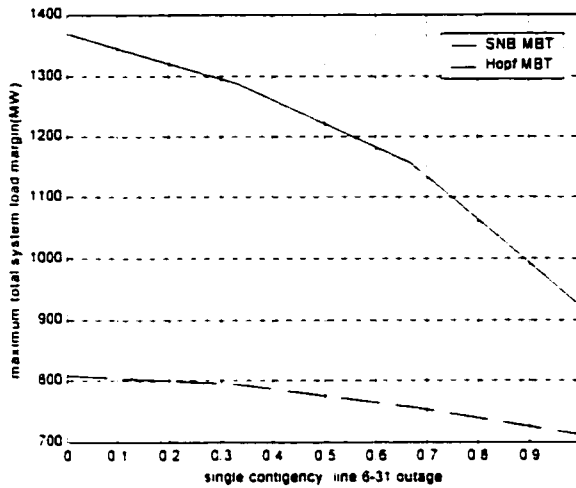


Figure 5-10: Unified margin boundary tracing versus line outage

5.6 Advantages of Unified Margin Boundary Tracing

- Unified Margin Boundary Tracing is accurate and reliable.
- It is easy to take account of limit effects and other nonlinearities.
- Margin boundary tracing dramatically saves CPU time compare to obtaining each new boundary point by exhaustively recomputing the whole PV curve.

5.7 Summary

In this chapter, we presented a unified framework to trace the SNB and Hopf bifurcation related margin boundary in multi-control parameter space under specified loading and control scenarios. It could be applied to monitor the load margin variation constrained by both voltage collapse and system oscillations under a control change or a contingency. It could also be used for an offline planning study.

CHAPTER 6 OPTIMAL MARGIN BOUNDARY TRACING WITH CONTINUATION

OPTIMAL POWER FLOW

6.1 Introduction

This chapter presents a general methodology to solve for the cost sense optimal control configurations corresponding to specified voltage stability margin levels. Based on the formulation of continuation optimal power flow, the optimal margin boundary is traced on the implicitly defined margin boundary surface in a multi-control parameter space. The proposed method considers all the system limits.

Load margin is often taken as a reasonable measure of proximity to bifurcation related instability. Independent System Operator (ISO) needs to monitor the system load margin in real time and close the power transaction deals based on the available system stability margin in order to meet the quickly varying energy demand. How to efficiently extend the system margin by the readjustment of the system control configuration becomes an important part of the power system operation.

In this chapter, optimal margin control is achieved with optimal margin boundary tracing (OMBT) based on continuation optimal power flow (COPF). It could automatically generate a whole set of cost based optimal control configurations with each optimal control configuration corresponding to a specific margin level that can be realized. Fig.2-2 is a conceptual diagram of the optimal margin boundary tracing re-demonstrated here. u_1 and u_2 are control parameters. m_0, \dots, m_3 indicate the voltage stability margins.

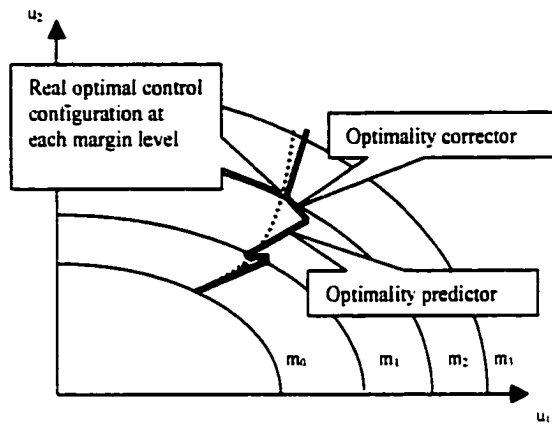


Figure 2-2: Optimal margin boundary tracing

6.2 Problem Formulation

The cost sense optimal control of specified load levels can be formulated as the solution of the following optimization problem, naturally parameterized by the load level parameter μ .

For a sequence of specified load levels μ ,

$$\min f(U) \quad (6.1)$$

Subject to

$$\begin{cases} F(X, Y, \mu, U) = 0 \\ G(X, Y, \mu, U) = 0 \end{cases} \quad (6.2)$$

$$h(X, Y, \mu, U) \leq 0 \quad (6.3)$$

Here (6.2) comes from an equilibrium formulation of the power system DAE model. $f(U)$ is the cost function representing the total control cost to be minimized. U represents the selected control variables from the most effective controls for real power generation rescheduling, shunt capacitance, reactive power compensation and load shedding. The

control range for other variables is simply determined by their available control capacity.

$h(X, Y, \mu, U)$ represents all the constraints that affect the system stability margin.

The above formulation is well established in the literature as an optimal power flow [28-31]. The Galiana group published a series of papers [27-31] on the optimal power flow based on the homotopy type continuation method. It could trace its optimal solution along a certain load scenario with optimization formulated with power flow equations. Load level is parameterized to achieve the optimal solutions in succession. However, the algorithm may diverge when the sequential specified load level is close to the largest feasible load margin.

Our aim is to specifically find an optimal control for specified load margin, that is, to seek the control configuration with the minimal control cost for given margin requirements.

To achieve this objective, the following assumptions are made:

$$1) \frac{\partial \mu_{mrs}}{\partial U_i} / \frac{\partial f}{\partial U_i} \geq 0, \text{ which indicates an increase in stability margin always results in}$$

corresponding increase in cost. (This is most likely case in practice.)

$$2) \text{ (i) } f(U) \geq 0$$

(ii) $f(U) = 0$ if and only if $U = U_0$, where U_0 is defined as the base case control configuration.

Proposition 6.1: *With the above assumptions, the optimal solution of the above formulation (6.1-6.3) is always on the Saddle node bifurcation related margin boundary manifold.*

Proof:

Assume there is an optimal solution $[X_1^T \ Y_1^T \ \mu_1 \ U_1^T]^T$ that is not on the margin boundary manifold. It has to be within the solvable region. Hence when U_1 is kept invariant, another feasible solution $[X_{mr\kappa 1}^T \ Y_{mr\kappa 1}^T \ \mu_{mr\kappa 1} \ U_1^T]^T$ could be achieved with $\mu_{mr\kappa 1} > \mu_1$. Obviously, control cost is kept constant that is, $f_{mr\kappa 1} = f_1$.

A change of ΔU_1 , could be made such that

$$\frac{\partial \mu_{mr\kappa}}{\partial U_1} \Delta U_1 = \mu_{mr\kappa 2} - \mu_{mr\kappa 1} = \mu_1 - \mu_{mr\kappa 1} < 0. \text{ that is, } \mu_{mr\kappa 2} = \mu_1. \quad (6.4)$$

From assumption 1), that is,

$$\frac{\partial \mu_{mr\kappa}}{\partial U_1} \Big/ \frac{\partial f}{\partial U_1} \geq 0. \quad (6.5)$$

$$\text{Therefore } f_{mr\kappa 2} - f_{mr\kappa 1} = f_{mr\kappa 2} - f_1 = \frac{\partial f}{\partial U_1} \Delta U_1 < 0. \quad (6.6)$$

Then there is a feasible solution $[X_{mr\kappa 2}^T \ Y_{mr\kappa 2}^T \ \mu_1 \ U_{mr\kappa 2}^T]^T$ such that control cost $f_{mr\kappa 2} < f_1$. This contradicts the fact that $[X_1^T \ Y_1^T \ \mu_1 \ U_1^T]^T$ is the optimal solution of formulation (6.1-6.3). This proves Proposition 6.1.

Therefore the above optimal margin control formulation could be applied to obtain optimal margin boundary tracing, which is a specific submanifold on margin boundary with minimum control cost corresponding to a given load margin.

6.3 Formulation of Optimal Margin Boundary Tracing

6.3.1 Optimal Margin Boundary Manifold of Power System

Margin boundary forms a multi-dimensional, implicitly defined manifold in multi-control parameter space. Specific local parameterization needs to be constructed to trace a certain sub-manifold with special property. The optimal control configuration for a given load margin is of special interest on the margin boundary manifold. That sub-manifold is called optimal margin boundary manifold. An optimal margin boundary manifold could be traced by augmenting the power system equilibrium equations introduced in chapter 5 with the optimality characterization equation.

6.3.2 Characterization of Optimal Margin Boundary

The Lagrangian of the optimal parameterized margin boundary problem is

$$L(X, Y, \mu, U) = f(U) + \lambda_F^T F(X, Y, \mu, U) + \lambda_G^T G(X, Y, \mu, U) + s^T h(X, Y, \mu, U) \quad (6.7)$$

Where $[\lambda_F^T \quad \lambda_G^T]^T$ is the multiplier vector for the equality constraints. s is the multiplier vector for the operation limit constraints of $[X, Y, \mu, U]^T$.

The first order K-T optimality conditions are.

$$\begin{bmatrix} L_X \\ L_Y \\ L_U \end{bmatrix} = \begin{bmatrix} 0 \\ 0 \\ f_U \end{bmatrix} + \begin{bmatrix} F_X^T & G_X^T & h_{AX}^T \\ F_Y^T & G_Y^T & h_{AY}^T \\ F_U^T & G_U^T & h_{AU}^T \end{bmatrix} \begin{bmatrix} \lambda_F \\ \lambda_G \\ s \end{bmatrix} = 0 \quad (6.8)$$

$$h_A(X, Y, \mu, U) = 0 \quad (h_A \text{ corresponds to active constraint set}) \quad (6.9)$$

$$\begin{bmatrix} F(X, Y, \mu, U) \\ G(X, Y, \mu, U) \end{bmatrix} = 0 \quad (6.10)$$

(6.8-6.10) characterize the optimal control configuration on the margin boundary manifold.

6.3.3 Optimal Margin Boundary Tracing with Continuation Optimal Power Flow

6.3.3.1 Initialization of the optimal margin boundary tracing

Before tracing for the optimal margin control submanifold on the power system equilibrium manifold, the initial margin is achieved by direct equilibrium tracing under U_0 . U_0 is optimal for this margin and could be used as the initial point of optimal margin control submanifold. The following methodology of continuation optimal power flow is proposed to further trace for the optimal control to extend the margin.

6.3.3.2 Optimality predictor

At the boundary predictor stage, the optimal tangent vector is sought with the optimization problem formulated in the tangent space which locally approximates the margin boundary manifold.

With the augmented Jacobian matrix of the first order optimality conditions (6.8-6.10), the optimality predictor is

$$\begin{bmatrix} F_X & F_Y & F_u & F_r & 0 & 0 & 0 \\ G_X & G_Y & G_u & G_r & 0 & 0 & 0 \\ h_{AX} & h_{AY} & h_{Au} & h_{Ar} & 0 & 0 & 0 \\ L_{XV} & L_{XY} & L_{Xu} & L_{Xr} & F_X^T & G_X^T & h_{AX}^T \\ L_{YX} & L_{YY} & L_{Yu} & L_{Yr} & F_Y^T & G_Y^T & h_{AY}^T \\ L_{uX} & L_{uY} & L_{uu} & L_{ur} & F_u^T & G_u^T & h_{Au}^T \\ e_k \end{bmatrix} \begin{bmatrix} dX \\ dY \\ d\mu \\ dU \\ d\lambda_F \\ d\lambda_G \\ ds \end{bmatrix}^{opt} = \begin{bmatrix} 0 \\ 0 \\ 0 \\ 0 \\ 0 \\ 0 \\ \pm 1 \end{bmatrix} \quad (6.11)$$

The optimality tangent vector is defined as

$$t^{opt} = [dX^T \quad dY^T \quad d\mu \quad dU^T \quad d\lambda_F^T \quad d\lambda_G^T \quad ds^T]^{opt} \quad (6.12)$$

Then the predicted optimal margin control solution is obtained by

$$\begin{bmatrix} X \\ Y \\ \mu \\ U \\ \lambda_F \\ \lambda_G \\ s \end{bmatrix}^{t+1} = \begin{bmatrix} X \\ Y \\ \mu \\ U \\ \lambda_F \\ \lambda_G \\ s \end{bmatrix}^t + \delta \begin{bmatrix} dX \\ dY \\ d\mu \\ dU \\ d\lambda_F \\ d\lambda_G \\ ds \end{bmatrix}^{opt} \quad (6.13)$$

6.3.3.3 Optimality corrector

The optimality corrector brings the optimal margin control solution back to the optimal margin boundary manifold.

$$\begin{bmatrix} F_X & F_Y & F_u & F_t & 0 & 0 & 0 \\ G_X & G_Y & G_u & G_t & 0 & 0 & 0 \\ h_{AX} & h_{AY} & h_{Au} & h_{At} & 0 & 0 & 0 \\ L_{XV} & L_{YV} & L_{Xu} & L_{Xt} & F_Y^T & G_X^T & h_{AX}^T \\ L_{YX} & L_{YV} & L_{Yu} & L_{Yt} & F_Y^T & G_Y^T & h_{AY}^T \\ L_{tX} & L_{tY} & L_{tu} & L_{tt} & F_t^T & G_t^T & h_{At}^T \\ e_i \end{bmatrix} \begin{bmatrix} \Delta X \\ \Delta Y \\ \Delta \mu \\ \Delta U \\ \Delta \lambda_F \\ \Delta \lambda_G \\ \Delta s \end{bmatrix} = - \begin{bmatrix} F \\ G \\ h_A \\ L_X \\ L_Y \\ L_t \\ 0 \end{bmatrix} \quad (6.14)$$

6.3.3.4 Selection of continuation parameter

By selecting the variable with the largest differential change among state variables X , voltage, angle variables Y , control variable U , and load parameter μ , the difficulty of transverse on the power system optimal margin boundary manifold at the largest feasible load margin condition could be avoided.

6.3.3.5 Determination of the largest feasible load margin

The largest feasible load margin is determined by the sign change of $d\mu$. In the event that all the controls hit the limits, the COPF formulation will degenerate into CPF with all the control parameters fixed at the limits. Thereby the sign change of $d\mu$ still indicates the largest feasible load margin. COPF based optimal margin boundary tracing could avoid the divergence nearby the largest feasible load margin.

6.4 Optimal Margin Boundary Tracing Procedure

Optimal margin boundary tracing includes the following steps.

- 1) Specify a concerned loading scenario to measure load margin.
- 2) Direct equilibrium tracing [10] to the Saddle node bifurcation at the base operating control configuration, which is taken as the initial point of optimal margin boundary tracing.
- 3) Do optimal margin boundary prediction for an increased load level with the optimality predictor (6.11).
- 4) Do optimal margin boundary correction with the optimality corrector (6.14).
- 5) If a control variable exceeds the limit, add it into the active constraint set.
- 6) Go to 3) until $d\mu$ changes sign, which indicates that the system has reached the largest feasible load margin.

The flowchart is shown in Fig.6-1.

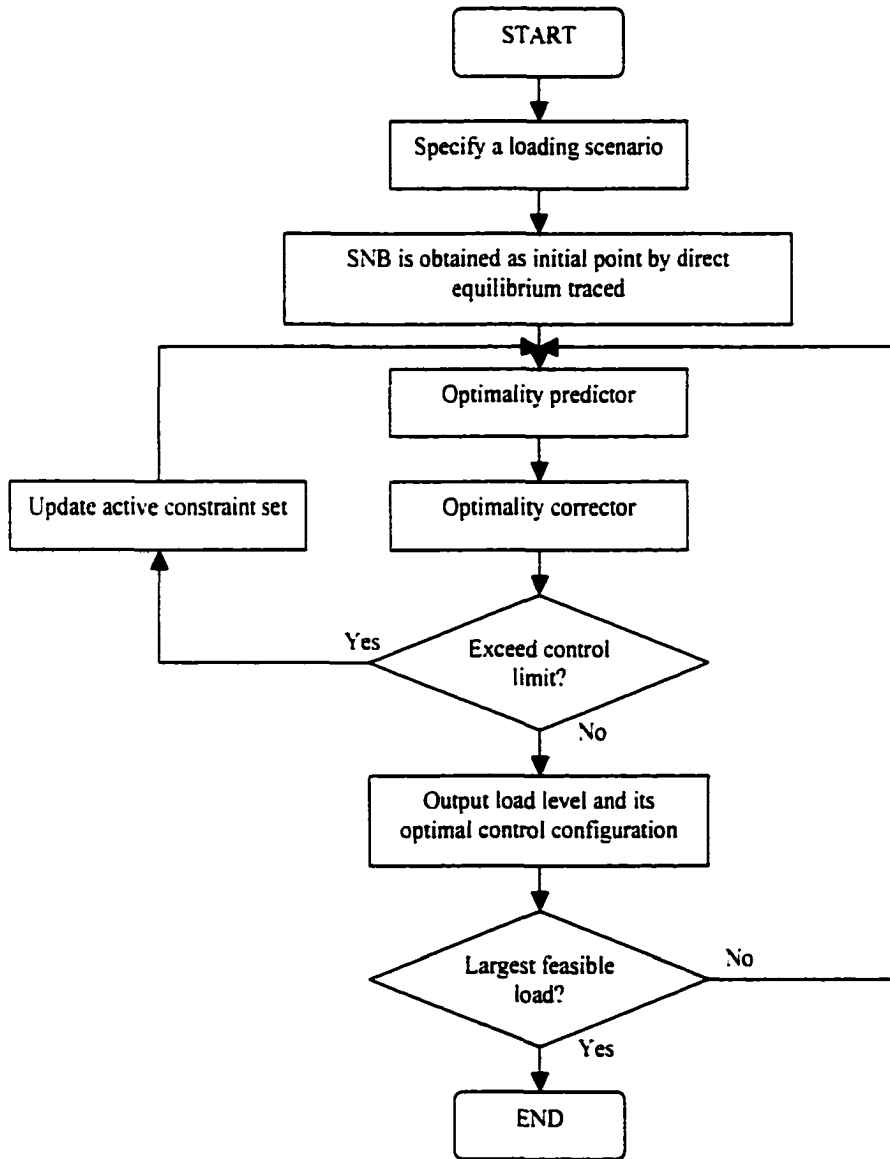


Figure 6-1: Flowchart of optimal margin boundary tracing

6.5 Numerical Results

Optimal margin control tracing for voltage stability margin control optimization is also demonstrated through the numerical tests performed on the New-England-39-bus system under the same assumptions as in chapter 5.

In addition, linear cost function $f(U) = W^T U$ is assumed. All controls are equally weighted as unity. Detail system data and control constraints are presented in the appendix.

Two control cases are studied using the optimal margin boundary tracing method. These control strategies are compared with linear programming (LP). The starting condition for optimal margin boundary tracing is the Saddle node bifurcation point obtained in power system equilibrium tracing, starting from the base case.

6.5.1 Case 1: Load Shedding

The loads at buses 4, 7, 8 are chosen for load shedding in order to maintain a certain margin. Fig.6-2 provides information related to an optimal load shedding for a given voltage stability margin. In that figure, the solid curve corresponds to a nonlinear optimal margin boundary tracing. The long dashed (___) curve corresponds to a margin sensitivity based linear programming (LP). An LP based approach is valid only up to a margin level of 28%. Even then, the accuracy of the LP based approach decreased with an increase in margin requirement. With OMBT a margin level of 38% is achieved. The margin stops at 38% when all the control variables hit the specified limits.

Individual load shedding curves for buses 4, 7, 8 are the components of the nonlinear optimal margin boundary of the total load shedding.

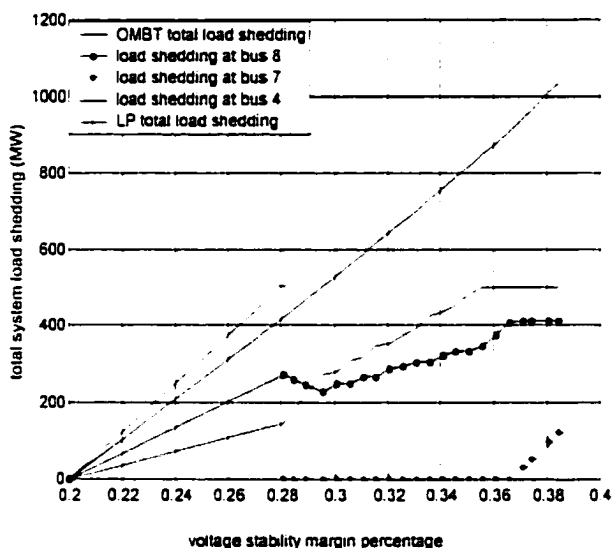


Figure 6-2: Margin boundary optimization comparison between OMBT and Linear Programming

6.5.2 Case 2: Control of Shunt Capacitance

For a given set of capacitors placed at buses 6, 7, 8, and 20 to maintain a given margin, three cases are considered.

- Optimal capacitor var requirements using the nonlinear optimal margin boundary tracing (OMBT) approach (solid curve in Fig.6-3).
- Optimal capacitor var requirements using the linear programming approach (long and short dashed curve in Fig.6-3).
- Capacitive var requirements when only the capacitor var at bus 20 is increased (Δ curve in Fig.6-3).

We can easily see that there is a large error when a linear programming based approach is used to estimate the var requirements to maintain a given margin. Notice that only the optimal margin boundary tracing method could get the control configuration at which the system margin level reaches the maximum feasible amount. By adding capacitor

only at bus 20, a system margin of no more than 22.5% will result. However, at this value the voltage at that bus might have exceeded its rated value.

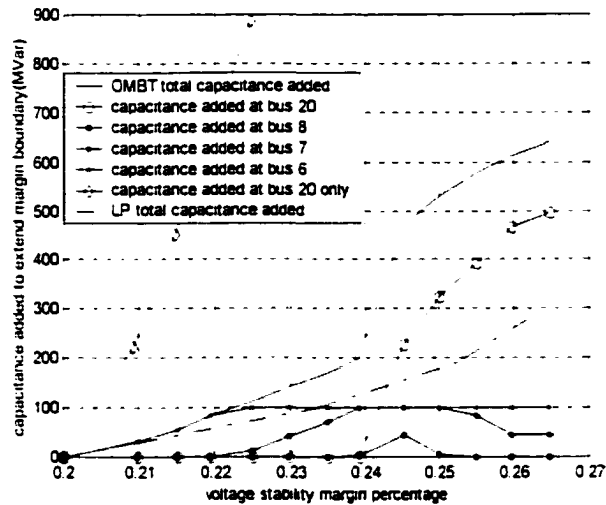


Figure 6-3: Margin boundary optimization comparison among OMBT, Linear Programming and, randomly chosen strategy (adding capacitance only at bus 20)

6.6 Summary

In this chapter, we present an approach based on the optimal margin boundary tracing to optimize the margin control for a given specified voltage stability margin. The system limit constraints are taken into account. Compared with the margin sensitivity based linear programming method, it takes account of limit effect and nonlinearity and hence is capable of solving for an optimal solution within a wide range of margin control. COPF based optimal margin boundary tracing could also avoid the divergence nearby the largest feasible load margin.

CHAPTER 7 LOCAL PARAMETERIZATION BASED UNIFIED TIME DOMAIN SIMULATION

7.1 Introduction

Time domain simulation of a large set of coupled algebraic and ordinary differential equations is an important part of power system analysis. Time domain simulation techniques are widely used for power system analysis because of their versatility and accuracy. The set of equations is usually formulated as a set of differential algebraic equations (DAE) [1].

The dynamic behavior associated with voltage instability involves a time horizon stretching from seconds to minutes. In [3], Taylor classifies voltage instability into transient and long term, according to the time it takes to collapse after a triggering event. For example, the 1987 collapse of the Tokyo Electric Company system [53] evolved over a period of about 30 minutes. However the 1985 Florida power failure due to voltage collapse evolved over a short period of 4 seconds [1]. Thus, the transient stability analysis and the long-term analysis have to be combined into a single computer program, which is quite different from the usual formulations that tend to decompose the dynamic behavior of power systems into different time horizons.

In recent years, a large effort has been spent in this area [41–45,54,55]. In all cases, this formidable stiff problem can be solved by the use of variable step size and variable order integration algorithms. Even though the multiple time scale simulation is solved by variable step size, the numerical problems associated with singularities near the collapse point is still a problem.

Due to the heavy non-linear behavior shown by the stressed power system, nonlinear analysis and nonlinear global (practically within a certain physical range) control are in

essence required by the nature of non-linearity around the voltage stability boundary. The timing of corrective control is vital for whether the system stability can be restored. The conventional time domain simulation algorithms encounter numerical difficulty near the voltage collapse point. So a more robust and reliable algorithm is needed for an accurate simulation of the dynamics associated with voltage collapse. This is also an indispensable tool for determining the timing of the corrective control actions needed to restore voltage stability.

With the proposed manifold based method, the singularity problem associated with power system differential algebraic equations under heavy load condition could be avoided. This chapter presents a novel local parameterization based time domain simulation that not only solves multi-time-scale problem but also robust near the collapse point.

7.2 DAE Modeling for Time Domain Simulations

7.2.1 Multi-Time-Scale DAE Modeling

The power system multi-time scale DAE modeling for time domain simulation is given by (7.1-7.3).

$$\dot{X} = F^0(X, Y, Z, U) \quad (7.1)$$

$$0 = G^0(X, Y, Z, U) \quad (7.2)$$

$$\dot{Z} = H^0(X, Y, Z, U) \text{ with initial conditions } X(t_0) = X_0 \text{ and } Z(t_0) = Z_0 \quad (7.3)$$

In general, continuous long term dynamic represented by Z is separated from the short-term dynamics X . Here Z is a dynamic variable rather than an algebraic variable. Note that the models valid for different time scales are presented collectively under this full time scale power system DAE presentation.

Short-term time scale dynamic variables may represent the following components:

- Synchronous generators and their regulators, such as AVRs and governors.
- HVDC systems
- SVCs
- Induction motors

Long-term time scale dynamic variables include:

- Thermostatic and aggregate load recovery
- LTC dynamics
- Secondary voltage control
- Shunt capacitor/reactor switching
- Over excitation limits
- Armature current limiters

7.2.2 Quasi-Steady State DAE Modeling

In Quasi Steady State (QSS) analysis short-term dynamics are neglected by replacing the short-term differential equations with their equilibrium equations. This simplification results in the observation of only long term phenomena.

The power system QSS DAE modeling is given [5.18] by (7.4-7.6).

$$0 = F^0(X, Y, Z, U) \quad (7.4)$$

$$0 = G^0(X, Y, Z, U) \quad (7.5)$$

$$\dot{Z} = H^0(X, Y, Z, U) \text{ with initial conditions } Z(t_0) = Z_0 \quad (7.6)$$

Time domain integration is only applied on Z with X and Y updated as algebraic variables.

7.2.3 Unified DAE Modeling of Power System Dynamics

To demonstrate the methodology developed in this chapter, the multi-time-scale DAE model described by 7.1 to 7.3 is represented in a compact form as is shown below. This compact notation is called unified DAE.

$$\dot{S} = D(S, R, U) \quad (7.7)$$

$$0 = A(S, R, U) \quad (7.8)$$

$S(t_0) = S_0$, where S is the state variable that represents $[X^T \ Z^T]^T$ in multi-time scale modeling and Z in QSS DAE modeling; R is the instant responsive variable Y in multi-time scale modeling and $[X^T \ Y^T]^T$ in QSS DAE modeling. Corresponding relations hold for D and A . U always stands for a set of parameters characterizing system control configuration.

7.3 Formulation of Conventional Time Domain Simulation of Unified DAE

7.3.1 Conventional Time Domain Simulation of Unified DAE

Denote t_Δ as the integration time step size. At i_{th} step, given $[S^{i'} \ \dot{S}^{i'} \ R^{i'} \ t^{i'}]^T$ and t_Δ^{i-1} , conventionally the following set of equations are solved for $[S^{(i+1)'} \ \dot{S}^{(i+1)'} \ R^{(i+1)'}]^T$ at $t^{i+1} = t^{i'} + t_\Delta^{i-1}$ (Note that t_Δ^{i-1} acts as a natural parameter. In conventional time domain simulation, it is pre-specified rather than calculated.)

$$\tilde{D}(S^{i+1}, \dot{S}^{i+1}, R^{i+1}, t_\Delta^{i-1}) = D(S^{i+1}, R^{i+1}, U) - \dot{S}^{i+1} = 0 \quad (7.9)$$

$$\tilde{A}(S^{i+1}, \dot{S}^{i+1}, R^{i+1}, t_\Delta^{i-1}) = A(S^{i+1}, R^{i+1}, U) = 0 \quad (7.10)$$

$$f(S^{i+1}, \dot{S}^{i+1}, t_\Delta^{i-1}) = 0 \quad (7.11)$$

where f presents the integration methods that may be applied in time domain simulation. They could be explicit methods such as the Euler method or implicit methods

such as the Backward Euler or the Trapezoidal Rule methods. For simplicity, the Euler method is employed in this chapter to demonstrate the difference between conventional and local parameterization based time domain simulation algorithms. For the Euler method equation, (7.11) will be replaced by (7.12).

$$f(S^{i+1}, \dot{S}^{i+1}, t_{\Delta}^{i+1}) = S^{i+1} - S^i - t_{\Delta}^{i+1} \dot{S}^i = 0 \quad (7.12)$$

7.3.2 Conventional Time Domain Simulation of Multi-Time-Scale DAE

Specifically for a conventional time domain simulation of multi-time-scale DAE, a set of nonlinear equations are solved for $[X^{(i+1)T} \quad \dot{X}^{(i+1)T} \quad Y^{(i+1)T} \quad Z^{(i+1)T} \quad \dot{Z}^{(i+1)T}]^T$ with specified t_{Δ}^{i+1} , given $[X^{iT} \quad \dot{X}^{iT} \quad Y^{iT} \quad Z^{iT} \quad \dot{Z}^{iT}]^T$.

For a Euler method integration, first X^{i+1} and Z^{i+1} can be expressed in term of X^i , \dot{X}^i , Z^i and \dot{Z}^i .

$$X^{i+1} = X^i + t_{\Delta}^{i+1} \dot{X}^i \quad (7.13)$$

$$Z^{i+1} = Z^i + t_{\Delta}^{i+1} \dot{Z}^i \quad (7.14)$$

And then $[Y^{(i+1)T} \quad \dot{Y}^{(i+1)T} \quad \dot{Z}^{(i+1)T}]^T$ is solved with specified t_{Δ}^{i+1} , as shown below

$$\tilde{F}(Y^{i+1}, \dot{X}^{i+1}, \dot{Z}^{i+1}, t_{\Delta}^{i+1}) = F^0(X^i + \dot{X}^i t_{\Delta}^{i+1}, Y^{i+1}, Z^i + \dot{Z}^i t_{\Delta}^{i+1}, U) - \dot{X}^{i+1} = 0 \quad (7.15)$$

$$\tilde{H}(Y^{i+1}, \dot{X}^{i+1}, \dot{Z}^{i+1}, t_{\Delta}^{i+1}) = H^0(X^i + \dot{X}^i t_{\Delta}^{i+1}, Y^{i+1}, Z^i + \dot{Z}^i t_{\Delta}^{i+1}, U) - \dot{Z}^{i+1} = 0 \quad (7.16)$$

$$\tilde{G}(Y^{i+1}, \dot{X}^{i+1}, \dot{Z}^{i+1}, t_{\Delta}^{i+1}) = G^0(X^i + \dot{X}^i t_{\Delta}^{i+1}, Y^{i+1}, Z^i + \dot{Z}^i t_{\Delta}^{i+1}, U) = 0 \quad (7.17)$$

Limitations of a conventional algorithm in the solving of multi-time scale DAE:

- Stiff problems associated with a conventional multi-time-scale time domain simulation causes the ill condition of the Jacobian matrix. For multi-time scale, the ratio of the eigenvalue associated with a fast-time scale and that associated

with short-time scale is usually quite large. This leads to the stiff problem that brings numerical difficulty in solving for both time scales.

- A divergence of solution could be encountered during a time domain simulation due to the singularity of G_Y . This corresponds to the exact voltage collapse point in the time domain.

7.3.3 Conventional Time Domain Simulation of QSS DAE

In QSS time domain simulation we solve only for

$$\begin{bmatrix} X^{(n+1)\tau} & Y^{(n+1)\tau} & Z^{(n+1)\tau} & \dot{Z}^{(n+1)\tau} \end{bmatrix}^T \text{ with specified } t_{\Delta}^{(n+1)}, \text{ given } \begin{bmatrix} X^{(n)\tau} & Y^{(n)\tau} & Z^{(n)\tau} & \dot{Z}^{(n)\tau} \end{bmatrix}^T.$$

$X^{(n+1)}$ and $Z^{(n+1)}$ could be expressed similarly to (7.13) and (7.14). Then

$$\begin{bmatrix} Y^{(n+1)\tau} & \dot{Z}^{(n+1)\tau} \end{bmatrix}^T \text{ is solved with specified } t_{\Delta}^{(n+1)} \text{ (a natural parameter).}$$

$$\tilde{F}(Y^{(n+1)}, \dot{Z}^{(n+1)}, t_{\Delta}^{(n+1)}) = F^0(X^{(n+1)}, Y^{(n+1)}, Z^{(n+1)} + \dot{Z}^{(n+1)} t_{\Delta}^{(n+1)}, U) = 0 \quad (7.18)$$

$$\tilde{G}(Y^{(n+1)}, \dot{Z}^{(n+1)}, t_{\Delta}^{(n+1)}) = G^0(X^{(n+1)}, Y^{(n+1)}, Z^{(n+1)} + \dot{Z}^{(n+1)} t_{\Delta}^{(n+1)}, U) = 0 \quad (7.19)$$

$$\tilde{H}(Y^{(n+1)}, \dot{Z}^{(n+1)}, t_{\Delta}^{(n+1)}) = H^0(X^{(n+1)}, Y^{(n+1)}, Z^{(n+1)} + \dot{Z}^{(n+1)} t_{\Delta}^{(n+1)}, U) - \dot{Z}^{(n+1)} = 0 \quad (7.20)$$

Limitations of conventional algorithm in the solving of a quasi-steady state DAE:

- Divergence of solution could be encountered during a time domain simulation due

to the singularity of $\begin{bmatrix} F_X & F_Y \\ G_X & G_Y \end{bmatrix}$.

- Even though stiff problems are avoided by time scale decomposition, the assumption of the existence of stable equilibrium of fast dynamics could be violated and could lead to over-optimistic results.

7.4 Local Parameterization Based Time Domain Simulation of Unified DAE

The solution manifold of (7.9-7.11) can be naturally parameterized by t_{Δ}^{i-1} . It forms a one dimensional manifold. Similar to equilibrium tracing [10], the whole time trajectory is traced by a single step predictor-corrector approach on each piece of solution manifold defined by (7.9-7.11). Fig.7-1 shows the conceptual diagram.

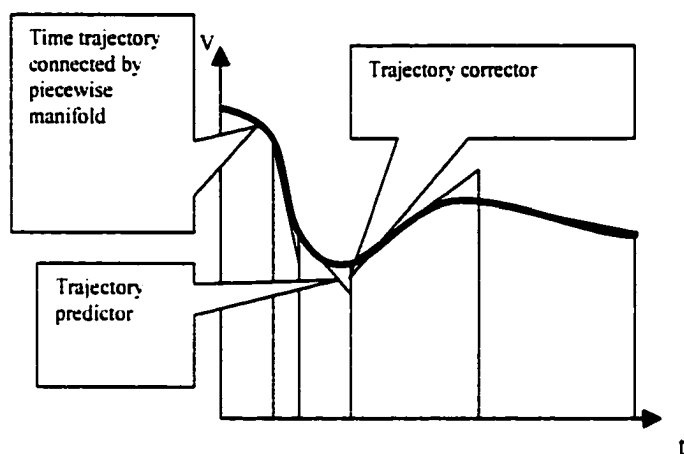


Figure 7-1: locally parameterized time trajectory tracing

7.4.1 Initial Point of Piecewise Manifold

At i th step, the trajectory point $[S^{iT} \quad \dot{S}^{iT} \quad R^{iT} \quad t^i]^T$ and $t_{\Delta}^{i-1} = 0$ satisfies the equations (7.9-7.11). It works as an initial point of the piecewise manifold defined by (7.9-7.11) at $(i+1)$ th step. Then, the next trajectory point $[S^{(i+1)T} \quad \dot{S}^{(i+1)T} \quad R^{(i+1)T} \quad t^{i+1}]^T$ could be achieved by a single iteration of the trajectory predictor and corrector along this piecewise manifold.

7.4.2 Trajectory Predictor

From the initial point $[S^{iT} \quad \dot{S}^{iT} \quad R^{iT} \quad t^i]^T$ and $t_{\Delta}^{i-1} = 0$, the next point can be predicted from the following equation.

$$\begin{bmatrix} D'_S & -I & D'_R & 0 \\ A'_S & 0 & A'_R & 0 \\ f'_S & f'_S & 0 & f'_{t_s} \\ e_k & & & \end{bmatrix} \begin{bmatrix} dS^{i-1} \\ d\dot{S}^{i-1} \\ dR^{i-1} \\ dt_s^{i-1} \end{bmatrix} = \begin{bmatrix} 0 \\ 0 \\ 0 \\ \pm 1 \end{bmatrix} \quad (7.21)$$

Then the predicted solution is

$$\begin{bmatrix} S^{i-1} \\ \dot{S}^{i-1} \\ R^{i-1} \\ t_s^{i-1} \end{bmatrix} = \begin{bmatrix} S^i \\ \dot{S}^i \\ R^i \\ 0 \end{bmatrix} + \delta \begin{bmatrix} dS^{i-1} \\ d\dot{S}^{i-1} \\ dR^{i-1} \\ dt_s^{i-1} \end{bmatrix} \quad (7.22)$$

δ is the step size that controls precision and progress of the local parameterization based time domain simulation.

When the Euler integration method is applied, that is

$$f'_S = I, \quad f'_S = 0, \quad f'_{t_s} = -\dot{S}^{i-1}$$

The following predictor with a reduced dimension could be achieved (after reduction is applied with (7.21))

$$\begin{bmatrix} -I & D'_R & D'_S \dot{S}^{i-1} \\ 0 & A'_R & A'_S \dot{S}^{i-1} \\ e_k & & \end{bmatrix} \begin{bmatrix} d\dot{S}^{i-1} \\ dR^{i-1} \\ dt_s^{i-1} \end{bmatrix} = \begin{bmatrix} 0 \\ 0 \\ \pm 1 \end{bmatrix} \quad (7.23)$$

7.4.3 Trajectory Corrector

The Newton method serves as the trajectory corrector.

$$\begin{bmatrix} D'_S & -I & D'_R & 0 \\ A'_S & 0 & A'_R & 0 \\ f'_S & f'_S & 0 & f'_{t_s} \\ e_k & & & \end{bmatrix} \begin{bmatrix} \Delta S^{i-1} \\ \Delta \dot{S}^{i-1} \\ \Delta R^{i-1} \\ \Delta t_s^{i-1} \end{bmatrix} = \begin{bmatrix} \tilde{D}^i \\ \tilde{A}^i \\ f^i \\ 0 \end{bmatrix} \quad (7.24)$$

$$\text{The time is updated by } t^{i-1} = t^i + t_s^{i-1} \quad (7.25)$$

Now a new time trajectory point $[S^{(i+1)T} \quad \dot{S}^{(i+1)T} \quad R^{(i+1)T} \quad t^{i+1}]^T$ has been achieved.

Error tolerance is set to control the accuracy of the solution. Here subscripts stand for the derivative of the respective functions

When the Euler integration method is applied, the following corrector with reduced dimension could be achieved.

$$\begin{bmatrix} -I & D_R^i & D_S^i \dot{S}^{i+1} \\ 0 & A_R^i & A_S^i \dot{S}^{i+1} \\ e_t & & \end{bmatrix} \begin{bmatrix} \Delta \dot{S}^{i+1} \\ \Delta R^{i+1} \\ \Delta t^{i+1} \end{bmatrix} = - \begin{bmatrix} \tilde{D}^i \\ \tilde{A}^i \\ 0 \end{bmatrix} \quad (7.26)$$

7.4.4 Continuation Parameter Selection

The variable with the largest variation among $[S^T \quad \dot{S}^T \quad R^T \quad t_s]^T$ is selected as the continuation parameter.

7.5 Local Parameterization Based Time Domain Simulation for Special Cases

7.5.1 Multi-Time-Scale DAE

In this section we specifically address the multi-time scale modeling as described by equations (7.1-7.3). The solution manifold of (7.15-7.17) can be parameterized by t_s^{i+1} . It forms a one dimensional manifold. Similar to equilibrium tracing, the whole time trajectory is traced by a single step predictor-corrector approach on each piece of solution manifold as defined by (7.15-7.17).

7.5.1.1 Trajectory predictor

Through the differentiation of (7.15-7.17), the Jacobian matrix could be achieved. From the initial point $[X^{iT} \quad Y^{iT} \quad Z^{iT} \quad \dot{X}^{iT} \quad \dot{Z}^{iT} \quad t^i]^T$, the next point can be predicted from the following equation utilizing an augmented Jacobian matrix.

$$\begin{bmatrix} -I_{n \times n} & F_Y^{0i} & 0 & F_X^{0i} \dot{X}^i + F_Z^{0i} \dot{Z}^i \\ 0 & H_Y^{0i} & -I_{d \times d} & H_X^{0i} \dot{X}^i + H_Z^{0i} \dot{Z}^i \\ 0 & G_Y^{0i} & 0 & G_X^{0i} \dot{X}^i + G_Z^{0i} \dot{Z}^i \\ & e_t & & \end{bmatrix} \begin{bmatrix} d\dot{X}^{i+1} \\ d\dot{Z}^{i+1} \\ dY^{i+1} \\ dt_{\Delta}^{i+1} \end{bmatrix} = \begin{bmatrix} 0 \\ 0 \\ 0 \\ \pm 1 \end{bmatrix} \quad (7.27)$$

Then the predicted solution is

$$\begin{bmatrix} \dot{X}^{i+1} \\ \dot{Z}^{i+1} \\ Y^{i+1} \\ t_{\Delta}^{i+1} \end{bmatrix} = \begin{bmatrix} \dot{X}^i \\ \dot{Z}^i \\ Y^i \\ 0 \end{bmatrix} + \delta \begin{bmatrix} d\dot{X}^{i+1} \\ d\dot{Z}^{i+1} \\ dY^{i+1} \\ dt_{\Delta}^{i+1} \end{bmatrix} \quad (7.28)$$

7.5.1.2 Trajectory corrector

Newton method serves as the trajectory corrector.

$$\begin{bmatrix} -I_{n \times n} & F_Y^{0i} & 0 & F_X^{0i} \dot{X}^i + F_Z^{0i} \dot{Z}^i \\ 0 & H_Y^{0i} & -I_{d \times d} & H_X^{0i} \dot{X}^i + H_Z^{0i} \dot{Z}^i \\ 0 & G_Y^{0i} & 0 & G_X^{0i} \dot{X}^i + G_Z^{0i} \dot{Z}^i \\ & e_t & & \end{bmatrix} \begin{bmatrix} \Delta \dot{X}^{i+1} \\ \Delta \dot{Z}^{i+1} \\ \Delta Y^{i+1} \\ \Delta t_{\Delta}^{i+1} \end{bmatrix} = - \begin{bmatrix} \bar{F} \\ \bar{H} \\ \bar{G} \\ 0 \end{bmatrix} \quad (7.29)$$

The time is updated by (7.25).

Now a new time trajectory point $[X^{(i+1)\tau} \ Y^{(i+1)\tau} \ Z^{(i+1)\tau} \ \dot{X}^{(i+1)\tau} \ \dot{Z}^{(i+1)\tau} \ t_{\Delta}^{i+1}]$ has been achieved.

7.5.1.3 Continuation parameter selection

The variable with the largest variation among $[Y^i \ \dot{X}^i \ \dot{Z}^i \ t_{\Delta}^i]$ is selected as the continuation parameter.

The advantages of local parameterization are as follow.

- When a system undergoes fast dynamics, time step size is adjusted according to the variation of \dot{s} . For example, if the ratio of $d\dot{X}_i$ to t_{Δ} is the largest, then

\dot{x}_i will be chosen as the continuation parameter. t_{Δ} is calculated so that each step change of \dot{x}_i will not be missed. If $\Delta\dot{x}_i$ is quite large, which indicates fast dynamics, smaller t_{Δ} is obtained.

- When a system undergoes slow dynamics, $\Delta\dot{x}_i$ is small, which indicates slow dynamics, then a larger t_{Δ} is obtained comparable to step size of continuation power flow. Therefore the number of integration steps is dramatically reduced for slow dynamics.
- The adaptable time step size is achieved based on continuation parameter selection. The proposed approach does not need second order or higher order information to obtain the time step. Conventional methods need this high order information.
- The singularity of network Jacobian matrix could be avoided.

7.5.2 QSS DAE

In this section we specifically address QSS modeling as described by equations (7.4 to 7.6). The solution manifold of (7.18-7.20) can be parameterized by t_{Δ}^{i-1} . Again it forms a one dimensional manifold. Similar to equilibrium tracing, the whole time trajectory is traced by a single step predictor-corrector approach on each piece of solution manifold as defined by (7.18-7.20).

7.5.2.1 Trajectory predictor

From the initial point $[X^{i'} \ Y^{i'} \ Z^{i'} \ \dot{Z}^{i'} \ t^i]^T$, the next point can be predicted from the following equation.

$$\begin{bmatrix} H_X^{0i} & H_Y^{0i} & -I_{J \times d} & H_X^{0i} \dot{X}' + H_Z^{0i} \dot{Z}' \\ F_X^{0i} & F_Y^{0i} & 0 & F_X^{0i} \dot{X}' + F_Z^{0i} \dot{Z}' \\ G_X^{0i} & G_Y^{0i} & 0 & G_X^{0i} \dot{X}' + G_Z^{0i} \dot{Z}' \\ e_k \end{bmatrix} \begin{bmatrix} d\dot{Z}'^{i+1} \\ dX'^{i+1} \\ dY'^{i+1} \\ dt_\Delta'^{i+1} \end{bmatrix} = \begin{bmatrix} 0 \\ 0 \\ 0 \\ \pm 1 \end{bmatrix} \quad (7.30)$$

Then the predicted solution is

$$\begin{bmatrix} \dot{Z}'^{i+1} \\ X'^{i+1} \\ Y'^{i+1} \\ t_\Delta'^{i+1} \end{bmatrix} = \begin{bmatrix} \dot{Z}'^i \\ X'^i \\ Y'^i \\ 0 \end{bmatrix} + \delta \begin{bmatrix} d\dot{Z}'^{i+1} \\ dX'^{i+1} \\ dY'^{i+1} \\ dt_\Delta'^{i+1} \end{bmatrix} \quad (7.31)$$

7.5.2.2 Trajectory corrector

Newton method serves as the trajectory corrector.

$$\begin{bmatrix} H_X^{0i} & H_Y^{0i} & -I_{J \times d} & H_X^{0i} \dot{X}' + H_Z^{0i} \dot{Z}' \\ F_X^{0i} & F_Y^{0i} & 0 & F_X^{0i} \dot{X}' + F_Z^{0i} \dot{Z}' \\ G_X^{0i} & G_Y^{0i} & 0 & G_X^{0i} \dot{X}' + G_Z^{0i} \dot{Z}' \\ e_k \end{bmatrix} \begin{bmatrix} \Delta \dot{Z}'^{i+1} \\ \Delta X'^{i+1} \\ \Delta Y'^{i+1} \\ \Delta t_\Delta'^{i+1} \end{bmatrix} = - \begin{bmatrix} \tilde{H} \\ \tilde{F} \\ \tilde{G} \\ 0 \end{bmatrix} \quad (7.32)$$

The time is updated by (7.25).

Now a new time trajectory point $[X^{(i+1)T} \ Y^{(i+1)T} \ Z^{(i+1)T} \ \dot{Z}^{(i+1)T} \ t_\Delta^{i+1}]$ has been achieved.

7.5.2.3 Continuation parameter selection

The variable with the largest variation among $[X^T \ Y^T \ \dot{Z}^T \ t_\Delta^T]$ is selected as the continuation parameter.

The advantage of local parameterization is that

- We can avoid the singularity of $\begin{bmatrix} F_x^0 & F_y^0 \\ G_x^0 & G_y^0 \end{bmatrix}$. Solution no longer diverges during the DAE time domain simulation when QSS is approaching the voltage collapse point.

7.6 Manifold Based Time Domain Simulation Procedure

- 1) Set up an initial operating point by evaluating the state variable based on network variables.
- 2) If a contingency or control event occurs, determine the post-event condition $[x^{nr} \ z^{nr} \ t_0]$ of the power system and calculate $[y^{nr} \ x^{nr} \ z^{nr}]$ under the post-event network configuration with (7.24)
- 3) Predict trajectory with (7.21-7.22)
- 4) Correct trajectory with (7.24-7.25).
- 5) Go to 2) until it reaches the specified end time for the simulation

The flowchart of the procedure is shown in Fig.7-2.

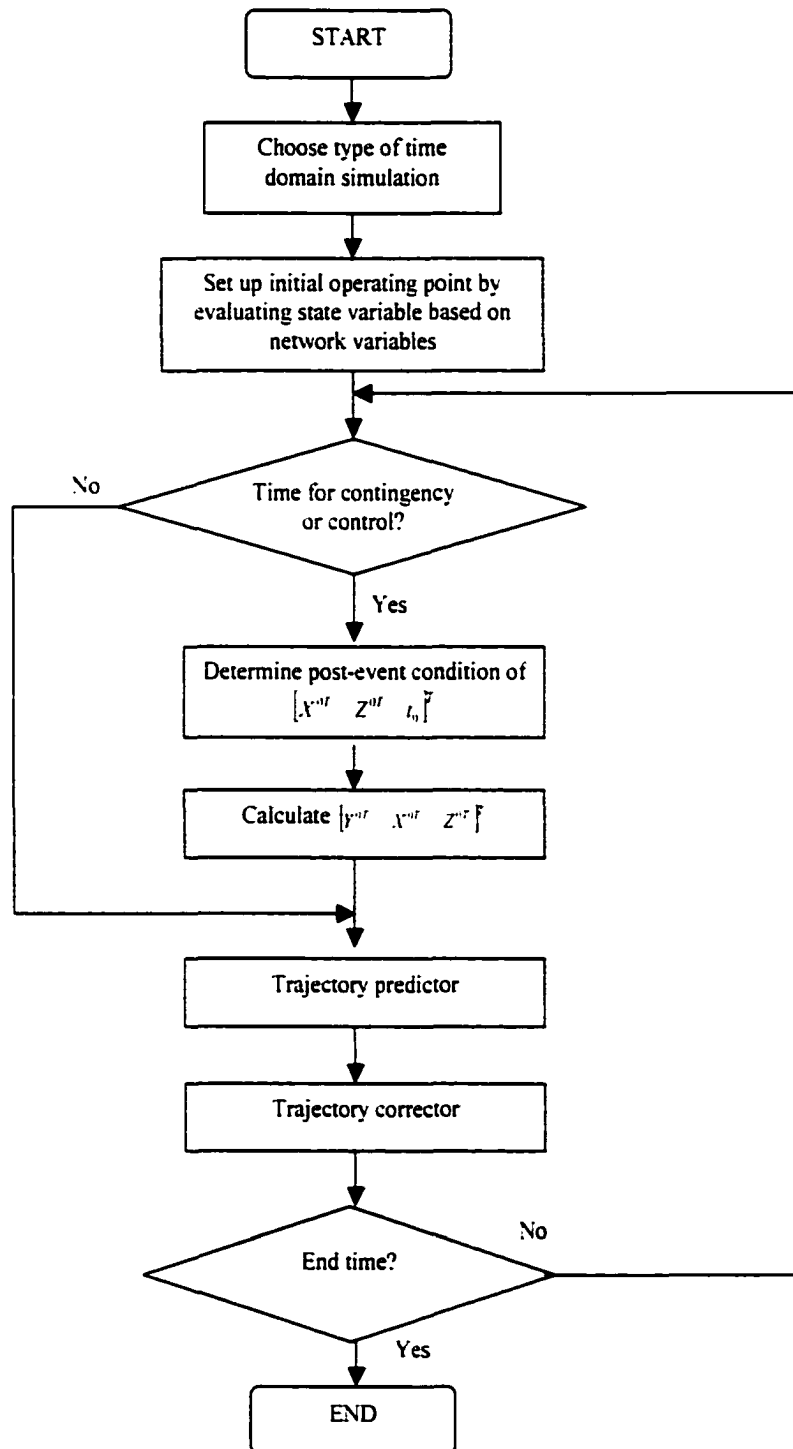


Figure 7-2: Flowchart of manifold based time domain simulation

7.7 Numerical Simulation Results

Manifold based unified time domain simulation is demonstrated by utilizing the same New-England-39-bus system that was used before. The same base operating point as previous chapters works as the initial point. Here a constant load variation rate is assumed, so that $\dot{Z} = \dot{Z}_0 = 6.0$ MW/sec at all the load buses. The detailed system data is presented in the appendix.

Various cases are considered to demonstrate the flexibility of this methodology for time domain simulation with multiple time scales. The starting condition for local parameterization based time domain simulation is the base case power flow as is presented in Appendix.

7.7.1 Results for Multi-Time Scale Time Domain Simulation

The following time domain simulation cases are considered:

Case 1: Load variation with time without contingency

Case 2: Load variation with time before and after a line outage

Case 3: Load variation with time before and after load shedding

Case 4: Load variation with time before and after a capacitor switching

Case 5: Fixed load before and after a line outage

In case 1, here the load is varied at a constant rate at all the buses. In this case Hopf bifurcation occurs at around 30 sec. as shown in Fig.7-3. The period of this oscillation is close to 1 sec. as we can see from Fig.7-4, which is an enlarged section of Fig.7-3 between 134 sec. and 150 sec.

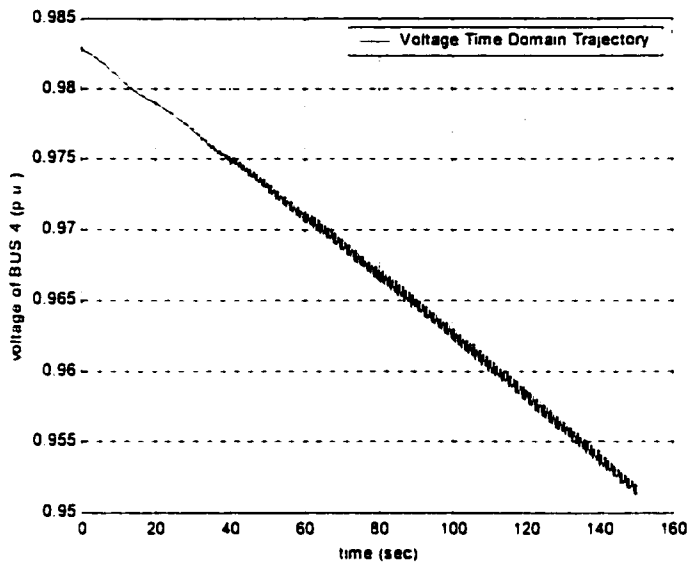


Figure 7-3: Small disturbance time domain simulation

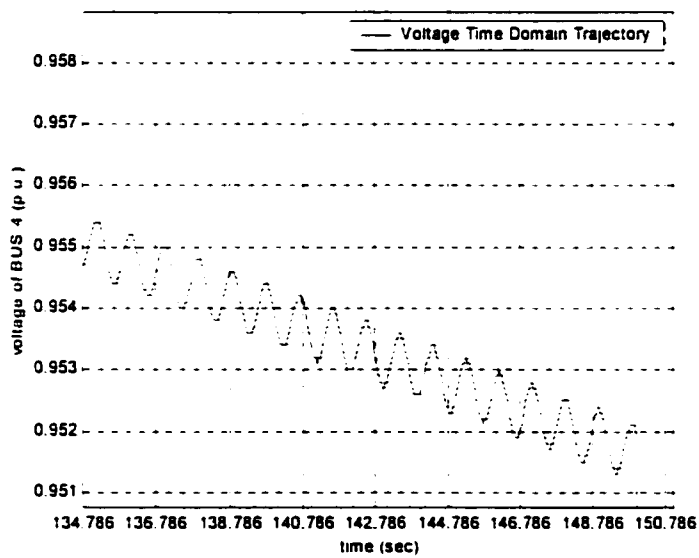


Figure 7-4: Enlarged oscillatory behavior

Case 2: In this example the branch from bus 7 to bus 8 is tripped at 80 sec. At the same time, the load is also changing at a constant rate. Fig.7-5 shows the time domain

simulation result. The time distance to collapse is shortened. This program could also easily handle the hybrid time scale problem due to the optimal selection of the continuation parameter. The selection of the continuation parameter is among voltage variables. The time step length is determined by constant step change of voltage, ensuring the larger time step size before outage disturbance and small enough time step size to characterize the system dynamics after the outage.

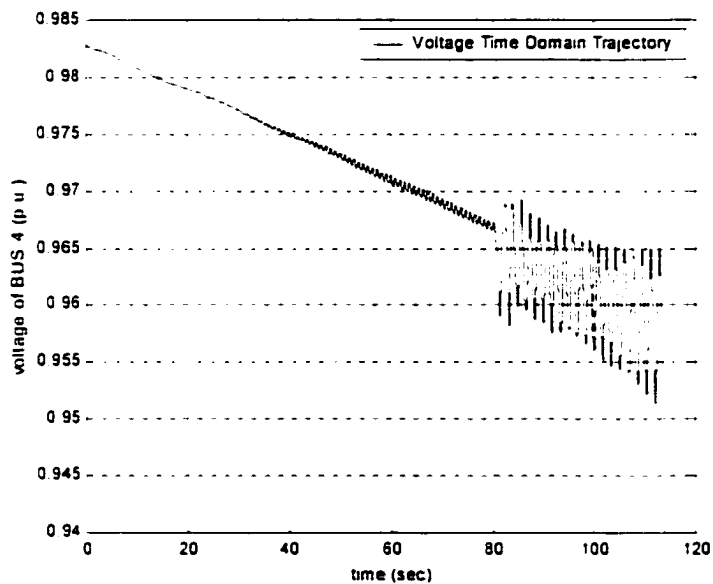


Figure 7-5: Line 8-9 is out at 80 sec

Case 3: In this example, a 100MW load is shed at bus 8. It is done at 80 sec., i.e. 20 seconds after L7-8 is out. Fig.7-6 shows the time distance to collapse is enlarged compared with the contingency case in Fig. 7-5. There is no numerical problem in time domain simulation with this heavily stressed system.

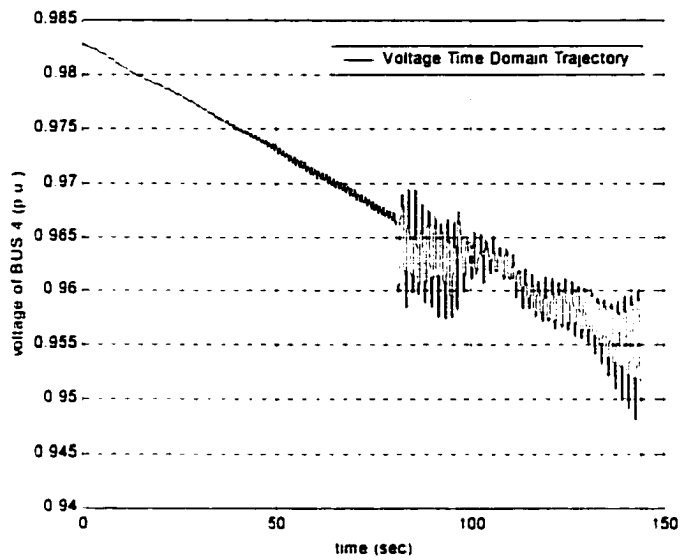


Figure 7-6: Load shedding at 20 seconds after contingency

Case 4: In this example a capacitance of 500 Kvar is added at bus 8. It is also added at 20 seconds after L7-8 is out. Fig.7-7 shows no evidence of enhancement of time disturbance to voltage collapse even though bifurcation theory based margin sensitivity indicates adding capacitance could increase the voltage stability margin. It seems that load dynamics make an impact on how capacitance affects system stability.

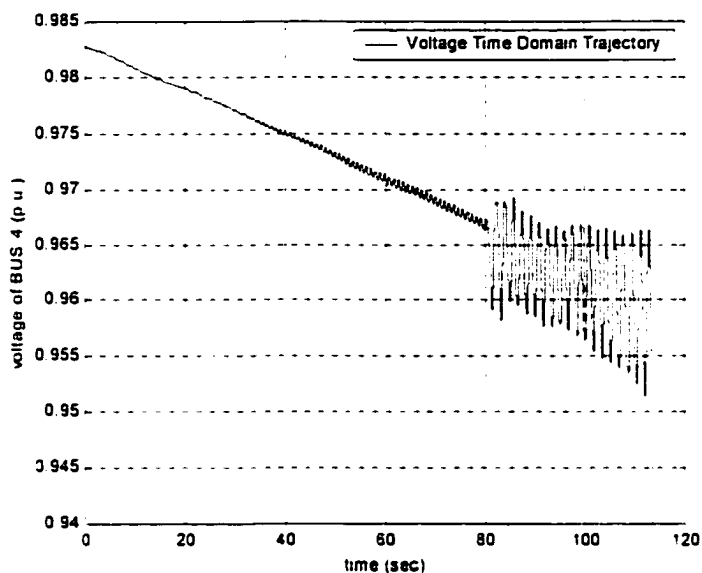


Figure 7-7: Capacitance is on at 20 seconds after the contingency

Case 5: In a conventional time domain simulation, in general, there is no load variation during simulation. The local parameterization based time domain simulation could also easily handle this type of time domain trajectory. Fig.7-8 shows the time domain simulation when the branch from bus 7 to bus 8 is out at base case with the load kept constant during the simulation period.

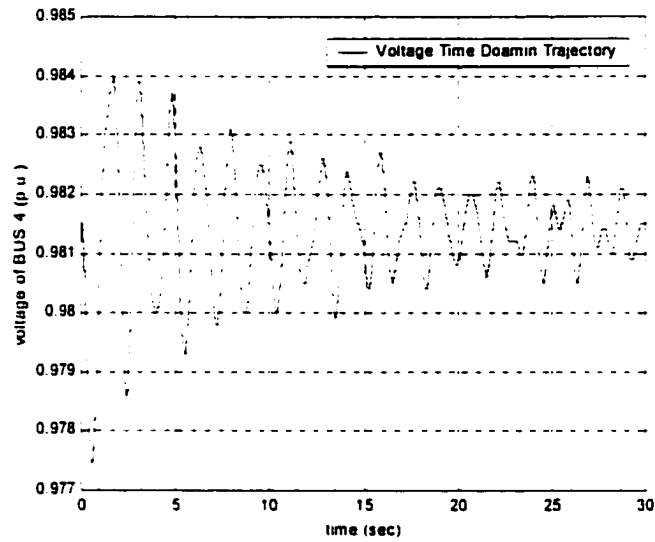


Figure 7-8: Line 8-9 is out at base condition with no load variation

7.7.2 Results for QSS Simulation

A QSS time domain simulation under only load variation is demonstrated in Fig.7-9. Note that the QSS method has its limitations in detecting the oscillatory instability due to fast dynamics. This is caused by the simplification of the DAE model based on the assumption that the equilibrium of undergoing fast dynamics could be achieved and stable.

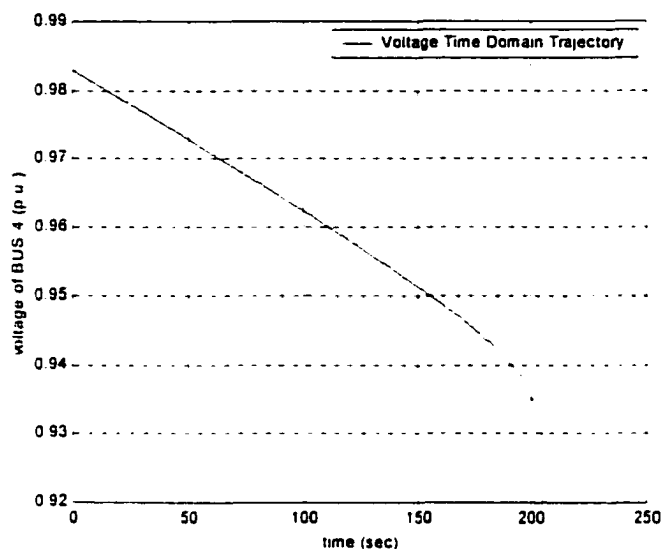


Figure 7-9: Quasi-Steady State simulation

7.7.3 Comparison with Margin Boundary Tracing

The margin achieved from margin boundary tracing is based on the identification of Saddle node or Hopf bifurcation. The assumption for bifurcation based analysis is that the bifurcation parameter is always time invariant. However, load is time variant in the time domain simulations of this chapter. Load dynamic effect on system stability is determined. As the results show, when affected by load dynamics, the system stability margin is always less than the margin calculated from margin boundary tracing, which is based on bifurcation theory.

7.8 Summary

In this chapter, a local parameterization based unified time domain simulation is presented. This methodology can be applied in both multi-time-scale and quasi-steady state DAE modeling of power system dynamics.

Local parameterization based time domain simulation could easily handle multi-time-scale dynamics so that fast dynamics could be captured along with slow dynamics. It is computationally efficient due to local parameterization. Moreover, numerical difficulty associated with conventional DAE time domain simulation algorithms could be avoided for a stressed system.

Local parameterization based QSS time domain simulation also could avoid the divergence of Newton iteration and deterioration of accuracy when it encounters Saddle node bifurcation of short-term dynamics.

CHAPTER 8. CONCLUSIONS AND SUGGESTIONS FOR FUTURE WORK

8.1 Conclusions

In stressed power system networks non-linearity becomes the dominant factor in studying the system's behavior. New nonlinear analysis tools are needed, both for small-disturbance as well as large disturbance stability studies. In this thesis, based on manifold theory, a set of new and novel algorithms for the nonlinear analysis of power system stability are developed. The proposed algorithms cover bifurcation, optimization and multi-time scale time domain simulation modifications, to study both the power system small-disturbance and large-disturbance voltage stability.

Power system small-disturbance stability computation involves:

- Power system equilibrium tracing with the detection of Saddle node and Hopf bifurcations:
- Unified stability margin boundary tracing in multi control parameter space for Saddle node and Hopf bifurcations:
- Continuation optimal power flow for achieving optimal margin control:

Power system large-disturbance stability computation involves:

- Time domain trajectory tracing for power system dynamics.

The proposed manifold based computational algorithms are large-scale system oriented. The algorithms are designed to avoid numerical ill conditioning when the system approaches a critical point both for steady state as well as time domain simulations. Numerical examples based on the New England 39 bus system are presented to demonstrate the versatility and usefulness of these algorithms. The new techniques are very useful for power system planning as well as real time margin monitoring

In summary, this thesis proposed a general methodology that can be used:

- To trace nonlinear voltage as well as oscillatory stability boundaries
- To find the minimum cost to obtain a specified margin
- To do numerically well conditioned time domain simulations

The major contributions of this approach are:

- A unified framework to trace the margin boundary in multi-parameter space under a specified loading and control scenario. The framework could be applied to monitor the load margin variation constrained both by voltage collapse and system oscillations. The framework doesn't require eigenvalue calculation.
- A nonlinear optimization method that calculates the minimum cost control solution for a given margin. Existing methods use linear margin sensitivities to include the margin constraint.
- A local parameterization based time domain simulation for large disturbance dynamic voltage stability analysis and corrective control. The approach is capable of capturing multi-time scale dynamics. For a stressed system, numerical difficulty associated with traditional algorithms could be avoided.

8.2 Suggestions for Future Work

- The Hopf detection algorithm can be further improved for any matrix other than the normal matrix.
- An efficient and optimal integration of steady state and time domain analysis that easily allows for one to get the answers to questions of timing and the amount of control needed to avoid voltage collapse.

REFERENCES

- [1] IEEE System Dynamic Performance Subcommittee. *Voltage stability of power systems: concepts, analytical tools and industry experience*. IEEE/PES Publication 90TH0358-2-PWR. 1990.
- [2] Y. Mansour. ed., *Suggested techniques for voltage stability analysis*. IEEE Working Group on Voltage Stability. Publication 93TH0620-5-PWR. 1993.
- [3] C.W. Taylor. *Power system voltage stability*. McGraw-Hill, New York. 1994.
- [4] P. Kundur. *Power system stability and control*. McGraw-Hill, New York. 1994.
- [5] T. Van Cutsem and Costa Vournas. *Voltage stability of electric power systems*. Kluwer Academic Publishers, Norwell, MA. 1998.
- [6] M. Ilic, J. Zaborszky. *Dynamics and control of large electric power systems*. John Wiley & Sons. New York. 2000.
- [7] L. H. Fink. ed. *Proceeding: Bulk power system voltage phenomena –III, voltage stability, security and control*. Davol, Switzerland. August. 1994.
- [8] L. H. Fink. ed. *Proceeding: Bulk power system dynamics and control IV restructuring*. Santonini. Greece. August 24-28. 1998.
- [9] V. Ajjarapu and C. Christy. "The Continuation power flow: a tool for steady state voltage stability analysis." *IEEE Transactions on Power Systems*. PWRS-7. Feb. 1992. pp.416-423.
- [9b] V. Ajjarapu. "Identification of steady state voltage stability in power systems." *International Journal of Energy System*. Vol.11. 1991, pp.43-46.

- [10] Z. Feng, V. Ajjarapu, and B. Long, "Identification of voltage collapse through direct equilibrium tracing," *IEEE Transactions on Power Systems*, Vol.15, Feb. 2000, pp. 342 – 349.
- [11] B. Long, V. Ajjarapu, "The sparse formulation of ISPS and its application to voltage stability margin sensitivity and estimation," *IEEE Transactions on Power Systems*, PWRS-14, August 1999, pp.944-957.
- [12] V. Ajjarapu, B. Lee. " Bifurcation theory and its application to nonlinear dynamical phenomena in an electrical power system," *IEEE Transactions on Power Systems*, Vol. 7, pp. 424-431 Feb. 1992.
- [13] V. Ajjarapu and B. Lee. "Bibliography on voltage stability," *IEEE Transactions on Power Systems*, PWRS-13, Feb. 1998, pp.115-125.
- [14] C. A. Canizares, A. C. Z. de Souza and V. H. Quintana. "Comparison of performance indices for detection of proximity to voltage collapse," *IEEE Transactions on Power Systems*, PWRS-11, August 1996, pp.1441-1450.
- [15] C. A. Canizares, F. L. Alvarado, "Point of collapse and continuation methods for large AC/DC systems," *IEEE Transactions on Power Systems*, PWRS-8, Feb. 1993, pp.1-8.
- [16] A.C.Z. de Souza, C.A. Canizares, V.H. Quintana. "New techniques to speed up voltage collapse computations using tangent vectors", *IEEE Transactions on Power Systems*, Vol. 12, Aug. 1997 pp. 1380 –1387.
- [17] T. Van. Cutsem. " An approach to corrective control of voltage instability using simulation and sensitivity," *IEEE Transactions on Power Systems*, PWRS-10, May 1995, pp.616-622.

- [18] T. Van Cutsem and C.D. Vournas, "Voltage stability analysis in transient and mid-term time scales," *IEEE Transactions on Power Systems*, Vol.11 Feb. 1996, pp. 146 –154.
- [19] T. Van Cutsem, "Voltage instability: phenomena, countermeasures, and analysis methods," *Proceedings of the IEEE*, Vol. 88, Feb. 2000, pp. 208 –227.
- [20] T. Van Cutsem Y. Jacquemart J.-N Marquet P. Pruvot, "A comprehensive analysis of mid-term voltage stability," *IEEE Transactions on Power Systems*, Vol. 10, Aug. 1995, pp. 1173 –1182.
- [21] A. J. Flueck and J. R. Dondeti, " A new continuation power flow tool for investigating the nonlinear effects of transmission branch parameter variations," *IEEE Transactions on Power Systems*, vol. 15 no. 1, February 2000, pp.223-227.
- [22] H. D. Chiang, A. J. Flueck, K. S. Shah and N. Balu, "CPFLOW: A practical tool for tracing power system steady-state stationary behavior due to load and generation variations," *IEEE Transactions on Power Systems*, PWR5-10, May 1995, pp.623-634.
- [23] I. Dobson and L. Lu, "Computing an optimal direction in control space to avoid saddle bifurcation and voltage collapse in electrical power systems," *IEEE Transactions on Automatic Control*, Vol.37, Oct. 1992, pp.1616-1620.
- [24] I. Dobson, F. Alvarado and C.L DeMarco, " Sensitivity of Hopf bifurcations to power system parameters," *Proceedings of the 31st IEEE Conference on Decision and Control*, 1992 vol.3, pp. 2928 –2933.
- [25] S. Greene, I. Dobson, F. L. Alvarado, " Contingency ranking for voltage collapse via sensitivities from a single nose curve," *IEEE Transactions on Power Systems*, PWR5-14, pp.232-240, Feb. 1999.

- [26] S. Greene, I. Dobson and F. L. Alvarado, "Sensitivity of the loading margin to voltage collapse with respect to arbitrary parameters." *IEEE Transactions on Power Systems*. PWRS-12. Feb. 1997. pp.262-272.
- [27] K.C. Almeida F.D. Galiana S. Soares. " A general parametric optimal power flow." *IEEE Transactions on Power Systems*. Vol. 9, Feb. 1994 pp. 540 –547.
- [28] Z. -C. Zeng, F.D. Galiana B.T. Ooi N. Yorino, "A simplified approach to estimate maximum loading conditions in the load flow problem." *IEEE Transactions on Power Systems*. Vol. 8. May 1993 pp. 646 –654.
- [29] M. Huneault and F.D. Galiana. "A survey of the optimal power flow literature." *IEEE Transactions on Power Systems*. Vol. 6. May 1991. pp. 762 –770.
- [30] M. Huneault and F.D. Galiana. "An investigation of the solution to the optimal power flow problem incorporating continuation methods." *IEEE Transactions on Power Systems*. Vol. 5. Feb. 1990. pp. 103 –110.
- [31] R.A. Ponrajah and F.D. Galiana. " The minimum cost optimal power flow problem solved via the restart homotopy continuation method." *IEEE Transactions on Power Systems*. Vol. 4. Feb. 1989. pp. 139 –148.
- [32] C.D. Vournas, M.A. Pai, P.W. Sauer. "The effect of automatic voltage regulation on the bifurcation evolution in power systems." *IEEE Transactions on Power Systems*. Vol. 11. Nov. 1996. pp.1683-1688.

- [33] K. Kim, H. Schattler, V. Venkatasubramanian, J. Zaborszky, P. Hirsch. "Methods for calculating oscillations in large power systems." *IEEE Transactions on Power Systems*. Vol. 12. Nov. 1997, pp.1639-1648.
- [34] F. Howell, V. Venkatasubramanian. "Transient stability assessment with unstable limit cycle approximation." *IEEE Transactions on Power Systems*. Vol. 14. May 1999, pp. 667-677.
- [35] W. Zhu, R.R. Mohler, R. Spee, W.A. Mittelstadt, D. Maratukulam. "Hopf bifurcations in a SMIB power system with SSR." *IEEE Transactions on Power Systems*. Vol. 11. Aug. 1996, pp.1579-1584.
- [36] W. C. Rheinboldt. *Numerical analysis of parameterized nonlinear equations*. John Wiley & Sons, New York, 1986.
- [37] Y. Saad. *Numerical methods for large eigenvalue problems*. Manchester University Press, New York, 1992.
- [38] B. D. Hassard, N. D. Kazarinoff and Y. -H. Wan. *Theory and applications of Hopf bifurcation*. Cambridge University Press, Cambridge, 1981.
- [39] J. Nocedal and S.J. Wright. *Numerical optimization*. Springer, New York, 1999.
- [40] R. Dai, and W. C. Rheinboldt, "On the computation of manifolds of foldpoints for parameter-dependent problems." *SIAM J. Numer. Anal.* Vol. 27, No. 2, April 1990, pp. 437-446.

- [41] F. Iavernaro, M. La Scala, F. Mazzia. "Boundary values methods for time-domain simulation of power system dynamic behavior." *IEEE Transactions on Circuits and Systems I: Fundamental Theory and Applications*, Vol. 45, Jan. 1998, pp. 50–63.
- [42] Chih-Wen Liu, J.S Thorp "New methods for computing power system dynamic response for real-time transient stability prediction." *IEEE Transactions on Circuits and Systems I: Fundamental Theory and Applications*, Vol. 47, March 2000, pp. 324–337.
- [43] B. Stott. "Power system dynamic response calculations." *Proc. IEEE*, Vol. 67, Feb. 1979, pp. 219–240.
- [44] H. Fankhauser, K. Aneros, A. Edris, and S. Torseng. "Advanced simulation techniques for the analysis of power system dynamics." *IEEE Comput. Applicat. Power*, Vol. 3, Oct. 1990, pp. 31–36.
- [45] J. Y. Astic, A. Bihain, and M. Jerosolimski. "The mixed Adams-BDF variable step size algorithm to simulate transient and long-term phenomena in power systems." *IEEE Transaction on Power Systems*, Vol. 9, May 1994, pp.929–935.
- [46] A. Berizzi, P. Finazzi, D. Dosi, P. Marannino, and s. corsi. " First and second order methods for volateg collapse assessment and security enhancement." IEEE/PES, PE-422-PWRS-0-01-1997, Winter Meeting, NY, Feb. 1997.
- [47] J. Barauin, T. Gomez, and F. L. pagola, " Estimating the loading limit margin taking into account voltage collapse areas." *IEEE Transaction on power systems*, Vol.10, no. 4, Nov. 1995, pp. 1952-1962.
- [48] P.W. Sauer and M.A. Pai. "Power system steady-state sability and the load flow Jacobian." *IEEE Transaction on power systems*, PWRS-5, Nov. 1990, pp. 1374-1383.

- [49] J. Deuse and M. Stubbe, "Dynamic simulation of voltage collapses." *IEEE transactions on Power Systems*. Vol. 8. 1993, pp. 894-904.
- [50] H. Fudeh, C. M. Ong, "A simple and efficient AC-DC load flow method for multiterminal DC systems." *IEEE Transactions on Power Apparatus and Systems*, Vol. PAS-100, No. 11 Nov. 1981, pp. 4389-4396.
- [51] Z. Feng, V. Ajjarapu and D. J. Maratukulam, "A practical minimum load shedding strategy to mitigate voltage collapse." *IEEE Trans. on Power Systems*. PWRS-13, Nov. 1998, pp.1285-1291.
- [52] W. C. Rheinboldt, "Solving algebraically explicit DAEs with the MANPAK-Manifold-Algorithms." *Computers Math. Applic.* Vol. 33, No. 3. 1997, pp.31-43.
- [53] A.kurita.T.Sakurai. "The Power System Failure on July 23, 1987 in Tokyo." *Proceedings of 27th Conference on Decision and Control*. Dec. 1998. pp.2093.
- [54] A.Kurita, H.Okubu, K. Oki, S. Agematsu, D.B. Klapper, N.W. Miller, W.W.Price, J.J. Sanchez-Gasca, K.A. Wirgau,T.D. Younkins, " Multiple Time Scale Power System Dynamic Simulation." *IEEE Trans. on Power Systems*. Vol.8, Feb.1993. pp.216-223.
- [55] J.F. Vernotte , P. Panciatici, B. Myers,J.P. Antoine, J. Deuse, and M. Stubbe." High Fidelity Simulation Power System Dynamics." *IEEE Computer Applications in Power*. Vol. 8, Jan. 1995, pp.37 -41.
- [56] George Angelidis, and Adam Semlyen. "Improved methodologies for the calculation of critical eigenvalues in small signal stability analysis". *IEEE Trans on Power Systems*. Vol. 11, No. 3, Aug. 1996, pp.1209-1217.


```

36 BUS36 1 1 2 1 0435 2.01 0.00 0.00 540.00 170.64 0.00 1.0635 500.00 -220.00 0.0000 0.0000 0 36
37 BUS37 1 1 2 1 0478 -3.43 0.00 0.00 520.00 69.56 0.00 1.0278 500.00 -220.00 0.0000 0.0000 0 37
38 BUS38 1 1 2 1 0265 1.73 0.00 0.00 810.00 159.60 0.00 1.0265 500.00 -300.00 0.0000 0.0000 0 38
39 BUS39 1 1 2 1 0300 -14.69 1104.00 250.00 1000.00 124.37 0.00 1.0300 900.00 -800.00 0.0000 0.0000 0 39

```

-.999

BRANCH DATA FOLLOWS

48 ITEMS

```

1 2 1 1 1 0 003500 0 041100 0.69870 0 0 0 0 0 0.0000 0.00 0.0000 0.0000 0.0000 0.0000 0.0000 1
1 39 1 1 1 0 002000 0 050000 0.37500 0 0 0 0 0 0.0000 0.00 0.0000 0.0000 0.0000 0.0000 0.0000 2
1 39 1 1 2 0 002000 0 050000 0.37500 0 0 0 0 0 0.0000 0.00 0.0000 0.0000 0.0000 0.0000 0.0000 3
2 3 1 1 1 0 001300 0 015100 0.25720 0 0 0 0 0 0.0000 0.00 0.0000 0.0000 0.0000 0.0000 0.0000 4
2 25 1 1 1 0 000700 0 008600 0.14600 0 0 0 0 0 0.0000 0.00 0.0000 0.0000 0.0000 0.0000 0.0000 5
3 4 1 1 1 0 001300 0 021300 0.22140 0 0 0 0 0 0.0000 0.00 0.0000 0.0000 0.0000 0.0000 0.0000 6
3 18 1 1 1 0 0001100 0 013300 0.21380 0 0 0 0 0 0.0000 0.00 0.0000 0.0000 0.0000 0.0000 0.0000 7
4 5 1 1 1 0 000800 0 012800 0.13420 0 0 0 0 0 0.0000 0.00 0.0000 0.0000 0.0000 0.0000 0.0000 8
4 14 1 1 1 0 000800 0 012900 0.13820 0 0 0 0 0 0.0000 0.00 0.0000 0.0000 0.0000 0.0000 0.0000 9
5 6 1 1 1 0 000200 0 002600 0.04340 0 0 0 0 0 0.0000 0.00 0.0000 0.0000 0.0000 0.0000 0.0000 10
5 8 1 1 1 0 000800 0 011200 0.14760 0 0 0 0 0 0.0000 0.00 0.0000 0.0000 0.0000 0.0000 0.0000 11
6 7 1 1 1 0 000600 0 009200 0.11300 0 0 0 0 0 0.0000 0.00 0.0000 0.0000 0.0000 0.0000 0.0000 12
6 11 1 1 1 0 000700 0 008200 0.13890 0 0 0 0 0 0.0000 0.00 0.0000 0.0000 0.0000 0.0000 0.0000 13
7 8 1 1 1 0 000400 0 004600 0.07800 0 0 0 0 0 0.0000 0.00 0.0000 0.0000 0.0000 0.0000 0.0000 14
8 9 1 1 1 0 002300 0 036300 0.38040 0 0 0 0 0 0.0000 0.00 0.0000 0.0000 0.0000 0.0000 0.0000 15
9 39 1 1 1 0 001000 0 025000 1.20000 0 0 0 0 0 0.0000 0.00 0.0000 0.0000 0.0000 0.0000 0.0000 16
10 11 1 1 1 0 000400 0 004300 0.07290 0 0 0 0 0 0.0000 0.00 0.0000 0.0000 0.0000 0.0000 0.0000 17
10 13 1 1 1 0 000400 0 004300 0.07290 0 0 0 0 0 0.0000 0.00 0.0000 0.0000 0.0000 0.0000 0.0000 18
13 14 1 1 1 0 000900 0 010100 0.17230 0 0 0 0 0 0.0000 0.00 0.0000 0.0000 0.0000 0.0000 0.0000 19
14 15 1 1 1 0 001800 0 021700 0.36600 0 0 0 0 0 0.0000 0.00 0.0000 0.0000 0.0000 0.0000 0.0000 20
15 16 1 1 1 0 000900 0 009400 0.17100 0 0 0 0 0 0.0000 0.00 0.0000 0.0000 0.0000 0.0000 0.0000 21
16 17 1 1 1 0 000700 0 008900 0.13420 0 0 0 0 0 0.0000 0.00 0.0000 0.0000 0.0000 0.0000 0.0000 22
16 19 1 1 1 0 001600 0 019500 0.30400 0 0 0 0 0 0.0000 0.00 0.0000 0.0000 0.0000 0.0000 0.0000 23
16 21 1 1 1 0 000800 0 013500 0.25480 0 0 0 0 0 0.0000 0.00 0.0000 0.0000 0.0000 0.0000 0.0000 24
16 24 1 1 1 0 000300 0 003900 0.06800 0 0 0 0 0 0.0000 0.00 0.0000 0.0000 0.0000 0.0000 0.0000 25
17 18 1 1 1 0 000700 0 008200 0.13190 0 0 0 0 0 0.0000 0.00 0.0000 0.0000 0.0000 0.0000 0.0000 26
17 27 1 1 1 0 001300 0 017300 0.32160 0 0 0 0 0 0.0000 0.00 0.0000 0.0000 0.0000 0.0000 0.0000 27
21 22 1 1 1 0 000800 0 014000 0.25650 0 0 0 0 0 0.0000 0.00 0.0000 0.0000 0.0000 0.0000 0.0000 28
22 23 1 1 1 0 000600 0 009600 0.18460 0 0 0 0 0 0.0000 0.00 0.0000 0.0000 0.0000 0.0000 0.0000 29
23 24 1 1 1 0 002200 0 035000 0.36100 0 0 0 0 0 0.0000 0.00 0.0000 0.0000 0.0000 0.0000 0.0000 30
25 26 1 1 1 0 003200 0 032300 0.51300 0 0 0 0 0 0.0000 0.00 0.0000 0.0000 0.0000 0.0000 0.0000 31
26 27 1 1 1 0 001400 0 014700 0.23960 0 0 0 0 0 0.0000 0.00 0.0000 0.0000 0.0000 0.0000 0.0000 32
26 28 1 1 1 0 004300 0 047400 0.78020 0 0 0 0 0 0.0000 0.00 0.0000 0.0000 0.0000 0.0000 0.0000 33
26 29 1 1 1 0 005700 0 062500 1.02900 0 0 0 0 0 0.0000 0.00 0.0000 0.0000 0.0000 0.0000 0.0000 34
28 29 1 1 1 0 001400 0 015100 0.24900 0 0 0 0 0 0.0000 0.00 0.0000 0.0000 0.0000 0.0000 0.0000 35
2 30 1 1 1 1 000000 0 018100 0.00000 0 0 0 0 0 1.0250 0.00 0.0000 0.0000 0.0000 0.0000 0.0000 36
6 31 1 1 1 1 000000 0 050000 0.00000 0 0 0 0 0 1.0700 0.00 0.0000 0.0000 0.0000 0.0000 0.0000 37
6 31 1 1 2 1 000000 0 050000 0.00000 0 0 0 0 0 1.0700 0.00 0.0000 0.0000 0.0000 0.0000 0.0000 38
10 32 1 1 1 1 000000 0 020000 0.00000 0 0 0 0 0 1.0700 0.00 0.0000 0.0000 0.0000 0.0000 0.0000 39
12 11 1 1 1 1 001600 0 043500 0.00000 0 0 0 0 0 1.0060 0.00 0.9200 1.0800 0.0000 0.9500 1.0500 40
12 13 1 1 1 1 001600 0 043500 0.00000 0 0 0 0 0 1.0060 0.00 0.9200 1.0800 0.0000 0.9500 1.0500 41
19 20 1 1 1 1 000700 0 013800 0.00000 0 0 0 0 0 1.0600 0.00 0.9200 1.0800 0.0000 0.9500 1.0500 42
19 33 1 1 1 1 000700 0 014200 0.00000 0 0 0 0 0 1.0700 0.00 0.0000 0.0000 0.0000 0.0000 0.0000 43
20 34 1 1 1 1 000900 0 018000 0.00000 0 0 0 0 0 1.0250 0.00 0.8750 1.1250 0.0000 0.9500 1.0500 44
22 35 1 1 1 1 000000 0 014300 0.00000 0 0 0 0 0 1.0250 0.00 0.0000 0.0000 0.0000 0.0000 0.0000 45
23 36 1 1 1 1 000500 0 027200 0.00000 0 0 0 0 0 1.0000 0.00 0.0000 0.0000 0.0000 0.0000 0.0000 46
25 37 1 1 1 1 000600 0 023200 0.00000 0 0 0 0 0 1.0250 0.00 0.0000 0.0000 0.0000 0.0000 0.0000 47
29 38 1 1 1 1 000800 0 015600 0.00000 0 0 0 0 0 1.0250 0.00 0.0000 0.0000 0.0000 0.0000 0.0000 48

```

-.999

LOSS ZONES FOLLOWS

2 ITEMS

-.99

INTERCHANGE DATA FOLLOWS

1 ITEMS

-.9

TIE LINES FOLLOW

0 ITEMS

-.999

3. The ISU Format of Dynamic Data of the New England System

NEW_ENGLAND SYSTEM STABILITY RELATED PARAMETERS OF GENERATOR & EXCITATION & GOVERNOR & SVC & OLTC & DYNAMIC LOADS

Generator transient parameter follows

Num	Gen_name	Xd	Xq	X'd	X'q	Rs	Tdo	T'qo	Mg	Dg
30	BUS30	0.1000	0.0690	0.0310	0.0690	0.0002	10.2000	0.010	84.000	5.000
31	BUS31	0.2590	0.2820	0.0700	0.1700	0.0002	6.5600	1.5000	60.600	5.000
32	BUS32	0.2500	0.2370	0.0530	0.0880	0.0002	5.7000	1.5000	71.600	5.000
33	BUS33	0.2620	0.2580	0.0440	0.1660	0.0002	5.6900	1.5000	57.200	5.000
34	BUS34	0.6700	0.6200	0.1320	0.1660	0.0002	5.4000	0.4400	52.000	5.000
35	BUS35	0.2540	0.2410	0.0300	0.0810	0.0002	7.3000	0.4000	69.600	5.000

36 BUS36	0.2950	0.2920	0.0490	0.1860	0.0002	5.6600	1.5000	52.800	5.000
37 BUS37	0.2900	0.2800	0.0570	0.0910	0.0010	6.7000	0.4100	48.600	5.000
38 BUS38	0.2110	0.2050	0.0570	0.0590	0.0002	4.7900	1.9600	69.000	5.000
39 BUS39	0.0200	0.0190	0.0060	0.0080	0.0002	7.0000	0.7000	1000.000	10.000

-999

Generator control system (excitor - AVR - governor) parameter follows

Num	Gen_name	Ke	Te	Se	Ka	Ta	Kf	Tf	Tch	Tg	Rg
30	BUS30	1.0000	0.2500	0.0000	20.0000	0.0600	0.0400	1.0000	1.6000	0.2000	0.0500
31	BUS31	1.0000	0.4100	0.0000	40.0000	0.0500	0.0600	0.5000	54.1000	0.4500	0.0500
32	BUS32	1.0000	0.5000	0.0000	40.0000	0.0600	0.0800	1.0000	10.0000	3.0000	0.0500
33	BUS33	1.0000	0.5000	0.0000	40.0000	0.0600	0.0800	1.0000	10.1800	0.2400	0.0500
34	BUS34	1.0000	0.7900	0.0000	30.0000	0.0200	0.0300	1.0000	9.7900	0.1200	0.0500
35	BUS35	1.0000	0.4700	0.0000	40.0000	0.0200	0.0800	1.2500	10.0000	3.0000	0.0500
36	BUS36	1.0000	0.7300	0.0000	30.0000	0.0200	0.0300	1.0000	7.6800	0.2000	0.0500
37	BUS37	1.0000	0.5300	0.0000	40.0000	0.0200	0.0900	1.2600	7.0000	3.0000	0.0500
38	BUS38	1.0000	1.4000	0.0000	20.0000	0.0200	0.0300	1.0000	6.1000	0.3800	0.0500
39	BUS39	1.0000	1.0000	0.0000	20.0000	0.0200	0.0300	1.0000	10.0000	2.0000	0.0500

-999

Dynamic loads data follows

Num	Bus_name	TapL	TqL	ALd	BLd	ALph	Beta
-----	----------	------	-----	-----	-----	------	------

-999

Static var compensator data follows

Num	Bus_name	Ksvs	Tsvs	Vsvsr
-----	----------	------	------	-------

-999

On load tap-changer data follows

S_N	Secondary_Bus	P_N	Prime_Bus	Tr	Vrr
-----	---------------	-----	-----------	----	-----

-999

4. The ISU Format of the Scenario Control File for the New England System

EXTENDED CONTINUATION POWER FLOW - VOLTAGE STABILITY ANALYSIS

DEPARTMENT OF ELECTRICAL AND COMPUTER ENGINEERING
IOWA STATE UNIVERSITY

BASE CASE: NEW ENGLAND 39 BUS 10 MACHINE TEST SYSTEM

OUTAGES: none

-999

LINE RATING TO USE IN ANALYSIS (1,2, OR 3)

2

.....
 LOCATION OF LOAD INCREASE FOR LOAD/GENERATION INCREASING SCENERIO (SCENARIO-1)
 =====

INITIAL _____ LOAD _____ VALUE

BUS	NAME	P(MW)	Q(MVAR)
-----	------	-------	---------

BUS NUMBERS WHERE LOAD IS TO BE INCREASED

3
 4
 7
 8
 12
 15
 16
 18
 20
 21
 23
 24
 25
 26
 27

28
29
39
-999

.....
LOCATION OF GENERATION INCREASE FOR LOAD/GENERATION INCREASING (SCENARIO-1)
=====

BUS NAME AREA OUTPUT(MW) INCREASING RATE %

BUS NUMBER WHERE GENERATOR WILL SUPPLY MORE POWER

30
31
32
33
34
35
36
37
38
39
-999

.....
LOCATION OF REACTIVE LOAD FOR REACTIVE LOAD INCREASING SCENERIO (SCENARIO-2)
=====

INITIAL LOAD VALUE

BUS NAME P(MW) Q(MVAR)

BUS NUMBERS WHERE REACTIVE LOAD IS TO BE ADDED

-999

.....
LOCATION OF EXPORTING UNITS FOR IMPORT/EXPORT SCENERIO (SCENARIO-3)
=====

BUS NAME AREA OUTPUT(MW) % EXPORT RATE (INCREASING)

BUS NUMBER, SCALING FACTOR

-999

.....
LOCATION OF IMPORTING UNITS FOR IMPORT/EXPORT SCENERIO (SCENARIO-3)
=====

BUS NAME AREA OUTPUT(MW) % IMPORT RATE (DECREASING)

BUS NUMBER, SCALING FACTOR

-999

.....
LOCATION OF LOAD INCREASE FOR LOAD/IMPORT SCENERIO (SCENARIO-4)
=====

INITIAL LOAD VALUE

BUS NAME P(MW) Q(MVAR)

BUS NUMBERS WHERE LOAD IS TO BE INCREASED AND SERVED FROM OUTSIDE

-999

.....
LOCATION OF GENERATION INCREASE FOR LOAD/IMPORT SCENERIO
=====

BUS NAME AREA OUTPUT(MW) % IMPORTED RATE

BUS NUMBER, SCALING FACTOR

-999 0

.....

LOCATION OF BUSES FOR REAL & REACTIVE LOAD SHEDDING

BUS	PL%	QL%
3	0	0
4	0	0
7	0	0
8	0	0
12	0	0
15	0	0
16	0	0
18	0	0
20	0	0
21	0	0
23	0	0
24	0	0
25	0	0
26	0	0
27	0	0
28	0	0
29	0	0
39	100	100
-999	0	0

DEFINITION OF SYSTEM ADJUSTMENTS FOR PREVENTIVE CONTROL

G#	VREF	PGS	VR_MAX	MU_MAX
30	0.00	0.00	0.00	0.00
31	0.00	0.00	0.00	0.00
32	0.00	0.00	0.00	0.00
33	0.00	0.00	0.00	0.00
34	0.00	0.00	0.00	0.00
35	0.00	0.00	0.00	0.00
36	0.00	0.00	0.00	0.00
37	0.00	0.00	0.00	0.00
38	0.00	0.00	0.00	0.00
39	0.00	0.00	0.00	0.00
-999	0	0	0	0

BUSES TO MONITER

BUS	NAME	AREA
30		
32		
33		
34		
35		
36		
37		
38		
39		
-999		

- 1) ESTIMATE OF MULTIPLE OF ORIGINAL LOAD FOR COLLAPSE..OR..
- 2) ESTIMATE OF (MVAR) OF REACTIVE LOADING BEFORE COLLAPSE..OR..
- 3) ESTIMATE OF (MW) OF INCREASED INTERCHANGE BEFORE COLLAPSE..OR..
- 4) ESTIMATE OF MULTIPLE OF ORIGINAL LOAD FOR COLLAPSE FOR LOAD/IMPORT

2.0
DESIRED VALUE OF LAMBDA AT CRITICAL POINT

0.30

CONVERGENCE TOLERANCE FOR POWER FLOW

0.001

MAXIMUM NUMBER OF ITERATIONS ALLOWED

80

NUMBER OF WEAK BUSES TO MONITER

10

ACKNOWLEDGEMENTS

I would like to acknowledge the effort of my major professor, Dr. Venkataramana Ajjarapu, who has given me a large amount of suggestions and instructions during my Ph. D research work. It is under his insightful vision and guidance that I could conduct my research smoothly and fruitfully. My great appreciation first goes to you, my advisor, Dr. Ajjarapu.

I also sincerely appreciate the assistance of Dr. Vijay Vittal, Dr. James D. McCalley, Dr. Degang J. Chen, Dr. Scott Hansen and Dr. Wolfgang Kliemann as being my committee members and so much advice from you enlightens my way to research accomplishment.

I would thank all the students and researchers in power group for their support and unforgettable friendliness during my three years in Iowa State University.

I always need to express my gratitude to my parents for their endless love and encouragement to me.

Sincere thanks go to my wife, Qianning Ma, who has been an indispensable part of my life and has given me her innermost support.